

# DOCTORAL THESIS

# Laser induced proton – boron fusion using TW-class laser system – study of novel approach employing protons produced during thermonuclear D(d,p)T reaction

## Author:

mgr inż. Przemysław TCHÓRZ Supervisor:

Dr hab. Sławomir JABŁOŃSKI, Dr inż. Marcin ROSIŃSKI

A thesis submitted in fulfillment of the requirements for the degree of Doctor of Philosophy

February 25, 2025

# **Declaration of Authorship**

I, mgr inż. Przemysław TCHÓRZ, declare that this thesis titled, "Laser induced proton – boron fusion using TW-class laser system – study of novel approach employing protons produced during thermonuclear D(d,p)T reaction" and the work presented in it are my own. I confirm that:

- This work was done wholly or mainly while in candidature for a research degree at this University.
- Where any part of this thesis has previously been submitted for a degree or any other qualification at this University or any other institution, this has been clearly stated.
- Where I have consulted the published work of others, this is always clearly attributed.
- Where I have quoted from the work of others, the source is always given. With the exception of such quotations, this thesis is entirely my own work.
- I have acknowledged all main sources of help.
- Where the thesis is based on work done by myself jointly with others,
   I have made clear exactly what was done by others and what I have
   contributed myself.

Signed:		
Date:		

# **Abstract**

## mgr inż. Przemysław TCHÓRZ

Laser induced proton – boron fusion using TW-class laser system – study of novel approach employing protons produced during thermonuclear D(d,p)T reaction

Majority of current research related to proton-boron approach of laser fusion employ hundreds of TW and PW-class laser systems to increase yield of alpha particles produced during  $p + {}^{11}B$  reaction. Recently, such laser systems became much more accessible, however the importance of enabling as many research groups as possible to contribute in the laser-fusion field requires seeking alternative approaches that could be implemented using moderate laser intensities. This dissertation is written in regard of generation of energetic ( $E_{max} > 4 \, MeV$ ), intense and directed proton beam during Cavity Pressure Acceleration (CPA) scenario of laser-matter interaction, where  $CD_2$ powder was used inside the target cavity. The origin of these protons is one of deuterium-deuterium fusion reaction channels, in which  ${}_{1}^{3}H$  and  $p^{+}$  are produced. The applicability of this approach is discussed based on magnetohydrodynamic simulations by evaluation of thermodynamical parameters, such as density, electron temperature and pressure arising during lasermatter interaction, which are crucial for driving the themronuclear reactions. The measurements of proton energy spectra carried out during experimental session served as an input for Monte Carlo simulations (FLUKA) of proton beam colliding with boron targets of different thickness, which suggest potential for few-TW laser systems to generate alpha particle flux comparable to these achieved using the most powerful laser beamlines.

# **Abstrakt**

## mgr inż. Przemysław TCHÓRZ

Laserowo indukowana fuzja proton-bor z wykorzystaniem układów laserowych klasy TW - badanie alternatywnego podejścia wykorzystującego wiązki protonowe wyprodukowane podczas reakcji D(d,p)T

Większość obecnie prowadzonych badań nad laserowo indukowaną reakcją fuzji typu proton-bor wykorzystuje do tego celu układy laserowe o mocach siggających od setek terawatów do petawata w celu zwiększenia ilości cząstek alfa produkowanych podczas reakcji  $p + {}^{11}B$ . Od niedawna układy laserowe tej klasy stały się szerzej dostępne, jednakże umożliwienie jak największej ilości grup badawczych rozpoczęcia bądź kontynuowania badań dotyczących fuzji z wykorzystaniem laserów wymaga znalezienia alternatywnych rozwiązań które umożliwiłyby stosowanie do tego celu układów laserowych o umiarkowanych intensywnościach impulsu, w klasycznym podejściu uważanych za niezdolne do produkcji wysokoenergetycznych protonów. Istotą poniższej rozprawy jest zbadanie możliwości produkcji intensywnych, wysokoenergetycznych ( $E_{max} > 4 MeV$ ) oraz ukierunkowanych wiązek protonowych poprzez wykorzystanie metody Cavity Pressure Acceleration (CPA), w której jako element paliwowy we wnęce użyty jest sproszkowany, deuterowany polietylen. Źródłem wysokoenergetycznych protonów w tym scenariuszu jest jeden z kanałów reakcji fuzji typu deuter-deuter, w którym produkowane są tryt  ${}_{1}^{3}H$  oraz proton  $p^{+}$ . Skuteczność zaproponowanej metody została oceniona na podstawie symulacji magnetohydrodynamicznych poprzez ewaluację parametrów plazmy takich jak gęstość, temperatura elektronowa oraz ciśnienie plazmy powstałej w ramach interakcji impulsu laserowego z tarczą typu cavity. Widma energetyczne wiązek protonowych, zarejestrowane podczas sesji eksperymentalnej w której wykorzystano mechanizm Cavity Pressure Acceleration, posłużyły jako dane wejściowe do symulacji Monte Carlo wykonanych przy pomocy kodu FLUKA, w których zadana wiązka protonowa oddziaływała z tarczami borowymi o różnej grubości oraz składzie chemicznym. Otrzymane rezultaty wskazują na możliwość użycia układów laserowych o mocach nieprzekraczających kilku terawatów do produkcji strumieni cząstek alfa, których intensywność jest bliska wartościom uzyskiwanych przy użyciu najintensywniejszych układów laserowych na świecie.

# Acknowledgements

First and foremost, my dear supervisors - this could not be written without your support and I am really grateful that both of you were guiding me not only during preparation of this manuscript, but since my early days in the Institute of Plasma Physics and Laser Microfusion.

It is necessarry to thank all of the PALS and IPPLM researchers who participated in experimental and theoretical activities over last several years that allowed to make this work feel complete. On top of that, I would like to acknowledge Mattia Cipriani (ENEA, Frascati, Italy) for his invaluable help with preparation, execution and discussion on results of FLASH simulations presented in this work.

Last but not least, I am really thankful to my entire family for encouraging me to pursue the scientific career path for the last 14 years and supported me during difficult times. I know all of you were waiting a little too long for this moment.

This work has been carried out within the framework of the EUROfusion Consortium, funded by the European Union via the Euratom Research and Training Program (Grant Agreement No. 101052200—EUROfusion). Views and opinions expressed are, however, those of the author(s) only and do not necessarily reflect those of the European Union or the European Commission. Neither the European Union nor the European Commission can be held responsible for them.

This scientific paper has been published as part of the international project called "PMW," co-financed by the Polish Ministry of Science and Higher Education within the framework of the scientific financial resources for 2020 – 2022 under the Contract No. 5199/PALS/2021/0 and was partially funded by LASERLAB-EUROPE (Grant No. PALS002750).

This research work was supported by the Ministry of Science and Higher Education as part of the IPPLM statutory subsidy. This research work was supported by the Ministry of Youth and Sports of the Czech Republic (Project Nos. LM2023068 and LM2018114 (PALS RI). This work was supported as well from the Czech Academy of Science's project "Strategy AV21 — Light at the service of society."

The dissertation is based upon work from COST Action CA21128 "PROton BOron Nuclear fusion: from energy production to medical applications," supported by COST (European Cooperation in Science and Technology — www.cost.eu).

The computing resources and the related technical support used for this work have been provided by CRESCO/ENEAGRID High Performance Computing infrastructure and its staff. CRESCO/ENEAGRID High Performance Computing infrastructure is funded by ENEA, the Italian National Agency for New Technologies, Energy and Sustainable Economic Development and by Italian and European research programmes.

# **Contents**

D	eclara	ation of	f Authorship	iii
<b>A</b> l	bstra	ct		v
A	cknov	wledge	ments	ix
Li	st of	Figures	5	xiii
Li	st of	Tables		xix
1	Intr	oductio	on	1
	1.1	Laser-	-based approach to fusion - a brief overview	1
		1.1.1	Laser ion acceleration - Target Normal Sheath Acceler-	
			ation	2
		1.1.2	Cavity Pressure Acceleration	4
		1.1.3	Proton - boron fusion scenario - laser-based approach .	10
		1.1.4	Thesis statement	13
2	Cha	racteri	zation of CPA-accelerated ion beams and their interaction	n
	witl	h boror	n target	15
	2.1	Radia	tive-hydrodynamic simulations of laser-matter interac-	
		tion e	mploying cavity geometry	15
	2.2	Thom	son Parabola Spectrometer (TPS)	24
		2.2.1	Principal of TPS operation	25
		2.2.2	Data analysis software	28
	2.3	Monte	e Carlo FLUKA simulations	33
		2.3.1	Interaction of proton beam with boron catcher:	
			geometry design and scoring estimators in FLAIR	34
3	Res	ults an	d discussion	39
	3.1	Exper	rimental and MC simulations results: High Power Laser	
		Labor	ratory (HPLL) (Warsaw, Poland)	40
		3.1.1	Experimental results	40

		Repub	olic)	48
		3.2.1	Experimental results	49
		3.2.2	Post-experimental FLASH simulations: PALS laser pulse	
			interaction with cavity target	58
		3.2.3	FLUKA simulations for CPA-induced proton beam	
			energy spectrum	62
4	Con	clusior	ıs	79
Bi	Bibliography 81			

# **List of Figures**

1.1	Basic approaches to inertial confinement fusion - direct-drive	
	(a), fast ignition (b) and in-direct drive (c) schemes. Taken	
	from [2]	1
1.2	Schematic of Target Normal Sheath Acceleration mechanism.	
	Taken from [16]	3
1.3	Schematic of Impact Fast Ignition method. Taken from [24]	5
1.4	Initial experimental design of target for Reverse Acceleration	
	Scheme. Taken from [25]	5
1.5	Reverse Acceleration Scheme target with cavity - the first Cav-	
	ity Pressure Acceleration experimental design. Taken from [27]	6
1.6	Target design for Forward Acceleration Scheme experiment.	
	Taken from [28]	6
1.7	Interferometric frames of macroparticle propagation using open	
	channel (a) and closed channel (b) of FAS type targets. Taken	
	from [28]	7
1.8	New Cavity Pressure Acceleration target design with low den-	
	sity ablator. Taken from [28]	7
1.9	Measurement of macroparticle velocity using interferometric	
	system for ablator-equipped cavity type targets. Taken from [28]	8
1.10	Dimensions of craters created during impact of LICPA-accelerated	
	flyer (a) in comparison to ablative acceleration (b) and direct	
	laser irradiation (c). Taken from [32]	9
1.11	Latest iteration of Cavity Pressure Acceleration targets suit-	
	able for neutron production. Taken from [33]	9
1.12	DT, DD, and P-B11 cross-sections. Taken from [35]	11
1.13	Progress of alpha particle production in laser-based experi-	
	ments in past years. Taken from [35]	12
2.1	Temporal profile of laser pulse used for simulations of laser-	
	matter interaction with cavity targets using nanosecond, kJ-	
	class laser system	16

2.2	Initial 2D density distribution of cavity "A" (left) and cavity "B"	
	(right)	17
2.3	2D distributions of density (upper left), electron temperature	
	(upper right), pressure (bottom left) and deposited laser en-	
	ergy (bottom right) for cavity "A" at 100 ps of simulation time	18
2.4	2D distributions of density (upper left), electron temperature	
	(upper right), pressure (bottom left) and deposited laser en-	
	ergy (bottom right) for cavity "A" at 1 ns of simulation time	19
2.5	2D distributions of density (upper left), electron temperature	
	(upper right), pressure (bottom left) and deposited laser en-	
	ergy (bottom right) for cavity "A" at 2 ns of simulation time	19
2.6	2D distributions of density (upper left), electron temperature	
	(upper right), pressure (bottom left) and deposited laser en-	
	ergy (bottom right) for cavity "A" at 3 ns of simulation time	20
2.7	2D distributions of density (upper left), electron temperature	
	(upper right), pressure (bottom left) and deposited laser en-	
	ergy (bottom right) for cavity "B" at $100 \ ps$ of simulation time .	21
2.8	2D distributions of $\rho$ (upper left), $T_e$ (upper right), $P$ (bottom	
	left) and deposited laser energy (bottom right) for cavity "B"	
	at: (a) $300 ps$ , (b) $1 ns$ , (c) $2 ns$ and (d) $3 ns$ of simulation time .	22
2.9	Time evolution of maximum values of thermodynamic param-	
	eters during simulation time for cavity geometries A and B	23
2.10	Raw image of deflected parabolas registered with multi-channel	
	plate and a camera at High Power Laser Laboratory (IPPLM,	
	Warsaw)	25
2.11	Schematic of Thomson Parabola Spectrometer designed at IP-	
	PLM (up) together with magnetic field profile measured along	
	magnetic poles (down)	26
2.12	Left: Fit of theoretical parabolas to high-energy part of parabo-	
	las of different ions registered using Image Plate during one of	
	experiments performed at Prague Asterix Laser System (CZ).	
	Right: Corresponding area of original image	27
2.13	Energy spectrum of parabolas from Fig. 2.12 (left) in units of	
	quantum-level	27
2.14	Snapshot of TPS results analysis process using TPSeer software.	28
2.15	Snapshot of "TPSeer" geometry definition of spectrometer	29
2.16	Positioning of origin of calculated fitting parabolas	29

2.17	Snapshot of "TPSeer" module responsible for defining the the-	20
2 10	oretical parabola.	30
	Result of fitting theoretical ion lines to experimental results	31
	Snapshot of "TPSeer" graphic edition module window	32
	Snapshot of FLAIR software main window	34
2.21	Snapshot of geometry designer module - proton beam (pur-	
	ple cone) irradiating boron disk target (top) and overlayed US-	25
2.22	RBIN scoring over one of the geometry ports (bottom)	35
2.22	Enlarged simulation geometry design with overlayed alpha	25
2.22	particle fluence on the targets front surface	35
	Experimental energy spectra of proton beams sampled by FLUKA	. 36
2.24	2D distribution of alpha particles fluence in FLUKA simula-	<b>~=</b>
	tion box	37
3.1	Schematic drawing of HPLL experimental chamber with stan-	
	dard positions of diagnostic devices	40
3.2	Parabola of protons captured by Multi-Channel Plate coupled	
	with Thomson Parabola Spectrometer. The image is processed	
	by "TPSeer" software and theoretical proton parabola is fitted	
	(black line)	41
3.3	Energy spectrum of protons captured on Fig. 3.2	42
3.4	Alpha particle energy spectrum for different thickness of pure	
	boron-11 catcher - calculated in FLUKA using energy spec-	
	trum obtained in HPLL	43
3.5	Alpha particle energy spectrum for different thickness of nat-	
	ural boron catcher - calculated in FLUKA using energy spec-	
	trum obtained in HPLL	44
3.6	Total alpha particle yield as a function of catcher thickness	45
3.7	2D alpha particle distribution for 80 $\mu m$ boron-11 catcher. Al-	
	pha particles are mainly emitted in backward direction	46
3.8	Neutron energy spectrum for different thickness of pure boron-	
	11 catcher - calculated in FLUKA using energy spectrum ob-	
	tained in HPLL	46
3.9	Neutron energy spectrum for different thickness of natural boron	
	catcher - calculated in FLUKA using energy spectrum obtained	
	in HPLL.	47
3.10	Three variants of cavity targets - cavity target with the channel	
	(a), cavity target without the channel (b) and cavity filled with	
	$CD_2$ powder (c)	49

3.11	Schematic of experimental chamber and positions of impor-	
	tant plasma diagnostics during described experimental cam-	
	paign	50
3.12	Ion traces captured by Thomson Parabola Spectrometer together	
	with fitted theoretical curves (left), zoomed in region repre-	
	senting two displaced proton traces (right)	51
3.13	Identified ion traces captured using Image Plate. Visible drop	
	in intensity of trace is an evidence of overlapping two parabo-	
	las of different origin (proton traces on left) or different ions of	
	same $\frac{q}{m}$ (carbon/deuterium ion trace on right)	51
3.14	Zoomed in region corresponding to high energy ions with clear	
	evidence of double-parabola formations	52
3.15	Energy spectra of protons extracted from concurrent proton	
	parabolas obtained in shot no. 59104 (Fig. 3.14)	53
3.16	Examples of DD-induced proton energy spectra from different	
	shots performed in described PALS experiment	53
3.17	Schematic picture of track detector holder equipped with Al	
	foils of different thickness used in described experiment	54
3.18	Microscopic image of track detector after irradiation through	
	20 μm Al filter	56
3.19	Microscopic image of track detector after irradiation through	
	50 μm Al filter	56
3.20	Microscopic image of track detector after irradiation through	
	65 μm Al filter	57
3.21	Microscopic image of track detector after irradiation through	
	83 <i>µm</i> Al filter	57
3.22	Temporal profile of PALS laser pulse intensity used for post-	
	experiment simulations of laser-matter interaction with cavity	
	target. The temporal profile is based on experimental data	58
3.23	2D distributions of density (upper left), electron temperature	
	(upper right), pressure (bottom left) and deposited laser en-	
	ergy (bottom right) for cavity used during PALS experiment	
	at 2.2 ns of simulation time	60
3.24	2D distributions of density (upper left), electron temperature	
	(upper right), pressure (bottom left) and deposited laser en-	
	ergy (bottom right) for cavity used during PALS experiment	
	at 3.2 <i>ns</i> of simulation time	60

3.25	Time evolution of maximum values of thermodynamic param-	
	eters during simulation time for cavity used during PALS ex-	
	periment	61
3.26	Alpha particle energy spectrum for different thickness of pure	
	boron-11 catcher - calculated in FLUKA using energy spec-	
	trum obtained in shot no. 59104	62
3.27	Total alpha particle (solid line) and neutron (dashed line) yield	
	as a function of catcher thickness	63
3.28	2D map of residual alpha particles fluence in $20 \mu m$ pure boron-	
	11 target volume	64
3.29	2D alpha particle distribution for 20 µm boron-11 catcher for	
	shot no. 59104 proton spectrum	64
3.30	2D map of residual alpha particles fluence in $100  \mu m$ pure boron-	
	11 target volume	65
3.31	2D alpha particle distribution for 100 $\mu m$ boron-11 catcher for	
	shot no. 59104 proton spectrum	65
3.32	2D map of residual alpha particles fluence in $300  \mu m$ pure boron-	
	11 target volume	66
3.33	2D alpha particle distribution for 300 $\mu m$ boron-11 catcher for	
	shot no. 59104 proton spectrum	66
3.34	Total alpha particle (solid line) and neutron (dashed line) yield	
	as a function of pure boron-11 (green) and natural boron (black)	
	catcher thickness for shot no. 59104	67
3.35	Alpha particle energy spectrum for different thickness of pure	
	boron-11 catcher - calculated in FLUKA using energy spec-	
	trum obtained in shot no. 59125	68
3.36	Total alpha particle (solid line) and neutron (dashed line) yield	
	as a function of pure boron-11 (blue) and natural boron (red)	
	catcher thickness for shot no. 59125	69
3.37	2D map of residual alpha particles fluence in $20  \mu m$ pure boron-	
	11 target volume (shot no. 59125)	70
3.38	2D alpha particle distribution for 20 µm boron-11 catcher for	
	shot no. 59125 proton spectrum	70
3.39	2D map of residual alpha particles fluence in $100  \mu m$ pure boron-	
	11 target volume (shot no. 59125)	71
3.40	2D alpha particle distribution for 100 $\mu m$ boron-11 catcher for	
	shot no. 59125 proton spectrum	71

3.41	2D map of residual alpha particles fluence in 300 µm pure boron-	
	11 target volume (shot no. 59125)	72
3.42	2D alpha particle distribution for 300 $\mu m$ boron-11 catcher for	
	shot no. 59125 proton spectrum	72
3.43	Result of Bethe-Bloch calculation of stopping 3.7 MeV pro-	
	ton in pure <sup>11</sup> B. Calculation was made using tool available	
	at https://web-docs.gsi.de/ lestinsk/beamcalc/bb.php	73
3.44	Total alpha particle (solid line) and neutron (dashed line) yield	
	as a function of catcher thickness - comparison of three de-	
	scribed cases.	74
3.45	Total normalized alpha particle (solid line) and neutron (dashed	
	line) yield as a function of catcher thickness	75
3.46	Ratio of total neutron and alpha particle yield calculated in	
	FLUKA as a function of target thickness	75
3.47	Numerical results presented in this work compared to exper-	
	imental campaigns performed in last 20 years. Reused and	
	edited from [35]	77

# **List of Tables**

1.1	Table of considered fusion reactions cross-sections for future	4.0
	power plants	10
2.1	Dimensions of cavity "A" and "B" discussed in this paragraph	17
3.1	Cut-off energy of protons for different thickness of Al filters	
	calculated in SRIM code	55
3.2	Parameters used for simulation of PALS laser pulse interaction	
	with the cavity used during experimental session	59

# 1 Introduction

# 1.1 Laser-based approach to fusion - a brief overview

Shortly after the development of first lasers, the idea of applying them in nuclear research was obvious. One of the most prominent concepts involving lasers is so called Inertial Confinement Fusion (ICF) - the fusion scenario firstly proposed by Nuckolls [1] - in which, contrary to Magnetic Confinement Fusion, the ignited plasma lifetime is determined only by its own inertia.

Along the years, ICF branched into three main approaches: direct-drive, in-direct drive and fast ignition scenario as pictured on Figure 1.1. Direct-drive implosions of deuterium-tritium (DT) fuel pellet require irradiation of the spherical target by multiple laser beams, granting direct energy transfer between laser pulses and the pellet surface. However, the non-uniformities and instabilities arising during the later stages of shell compression are highly dynamic and difficult to control.

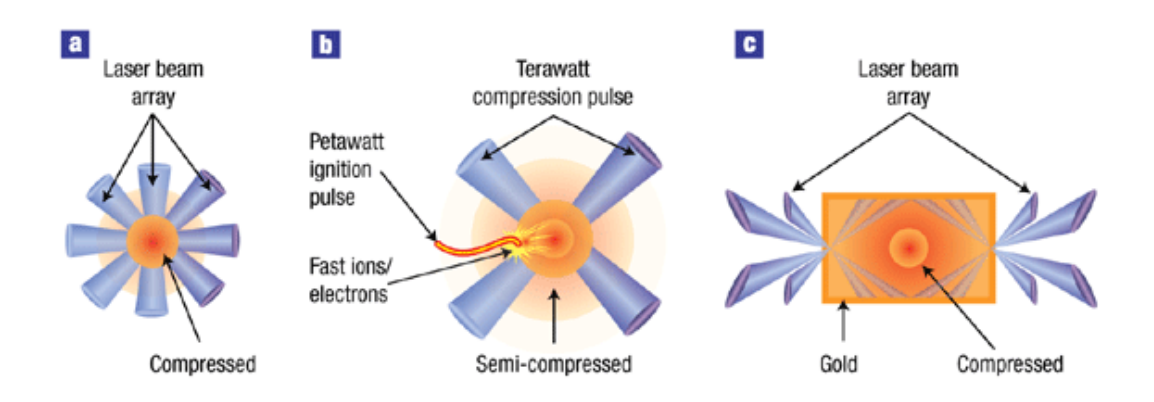


FIGURE 1.1: Basic approaches to inertial confinement fusion -direct-drive (a), fast ignition (b) and in-direct drive (c) schemes.

Taken from [2]

In-direct drive scenario of ICF is based on irradiation of the high-Z hohlraum's inner wall to produce X rays which then ablate the fuel pellet shell. This approach grants smoothing of the nonuniformities comparing to direct-drive, however at the cost of two-staged (laser - x ray - target) energy transfer which results in lower efficiency of the process comparing to direct irradiation of the target. Despite that, in last years the experiments conducted at Natinal Ignition Facility (USA) [3, 4, 5] resulted in breakthrough of achieving ignition of the fuel (Q = 1.54) for the first time in history on December 5th, 2022, providing 3.15 MJ of fusion energy from 2.05 MJ transported to target by means of 192 laser beams [6].

Although successful, the DT-based indirect-drive fusion experiments are in minority of the laser-induced fusion research due to specific technical difficulties and requirements, as well as limited accessibility of facilities capable to perform them. In spite of increasing number of laser systems around the world, offering impulse power up to petawatts, attempts to examine other candidate reactions for laser induced fusion arose. This thesis is devoted to the proton - boron fusion (1.1.3), which in recent years is intensively explored both by experimental and theoretical groups.

One of the key aspects of this reaction when utilizing lasers is generation of proton beam of suitable parameters to drive it, one of which is roughly 650 keV of centre-of-mass energy, therefore the basics of laser-induced ion acceleration will be presented in the next subsection of this document.

# 1.1.1 Laser ion acceleration - Target Normal Sheath Acceleration

Dating back to year 2000, three independent laser-matter experiments [7, 8, 9] reported presence of multi-MeV (1.5 MeV, 18 MeV and 58 MeV respectively) protons when irradiating solid, several microns thick targets with intense laser pulses. These ions were detected on the opposite side to the laser-illuminated surface and exhibited geometrical collimation rather than isotropic emission. In 2001 for the first time the Target Normal Sheath Acceleration model was introduced, explaining the generation mechanism of these energetic particles [10].

As of today, a number of other laser ion acceleration mechanisms were reported, such as Radiation Pressure Acceleration (RPA) [11, 12], Collisionless Shock Acceleration (CSI) [13], Break-Out Afterburner [14] or Magnetic Vortex Acceleration [15], however the TNSA approach is the most relevant to this thesis due to laser pulse intensity level available in Institute of Plasma

Physics and Laser Microfusion's High Power Laser Laboratory, where part of the experimental results was gathered.

In majority of laser ion acceleration experiments, the laser-plasma interaction occurs with use of the solid targets, for which electron density of created plasma  $n_e$  exceeds the critical (or cutoff) density

$$n_c = \frac{m_e \omega^2}{4\pi e^2} = 1.1 \times 10^{21} \text{ cm}^{-3} \left(\frac{\lambda}{1 \ \mu m}\right)^{-2},$$
 (1.1)

where  $\omega = \frac{2\pi c}{\lambda}$  is laser frequency,  $m_e$  is mass of an electron, c is the speed of light and  $\lambda$  is the wavelength of laser pulse. The  $n_e > n_c$  condition grants that no propagation of laser pulse in plasma can occur. However, the absorbed energy is transported inside the target by energetic (often referred as hot or fast) electrons accelerated from the plasma plume, which temperature is in the range  $T_e \approx 10~keV - 10~MeV$ . These electrons penetrate the volume of the target and reach it's rear side, creating a so-called electron Debye sheath. Due to unbalance of the charge in the system, the electric field is generated along normal to the rear side of the target.

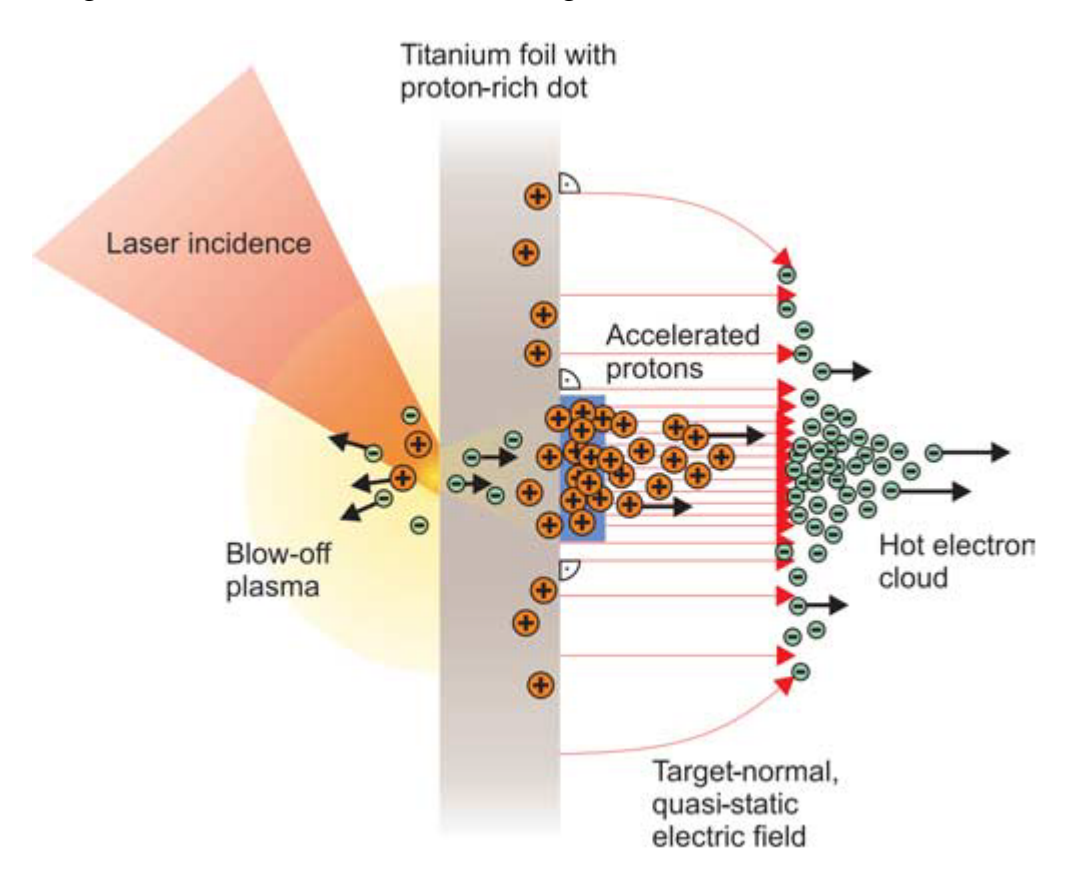


FIGURE 1.2: Schematic of Target Normal Sheath Acceleration mechanism. Taken from [16]

The intensity of generated electric field can be estimated as

$$\epsilon_{acc} = \frac{T_e}{e\lambda_{De}},\tag{1.2}$$

where  $\lambda_{De}$  is Debye length. According to range of  $T_e$ , the  $\epsilon_{acc}$  is in the range  $10^8 - 10^{11} \frac{V}{cm}$ . Such value of electric field results in ionization of contaminations on the rear side of the target and their acceleration together with light, positively charged ions that were ionized within the target volume.

In the last 20 years, since the TNSA model of laser ion acceleration was firstly proposed, the mechanism of accelerating ions using super-intense laser fields (corresponding to intensities of pulse and wavelength by relation  $I_L\lambda_L^2>10^{18}\,W/cm^2$ ) was verified and tested in hundreds of experiments using different levels of laser intensity, revealing in great detail the properties of TNSA ion beams, such as quasithermal distribution with a sharp cutoff at a maximum energy [17] or compact angular and spatial distribution of the beam [18]. In recent years, both influence of target characteristics [19] and sophisticated laser pulse parameters [20] are under heavy investigation to further improve the key features of laser-induced ion beams.

More recent exeriments preformed on frontier laser facilities, due to power of pulses reaching PW level, exploit hybrid acceleration scenarios, where TNSA mechanism is accompanied by other mentioned earlier acceleration scenarios. In most cases, as the laser-matter interaction enters so-called Relativistic Induced Transperency (RIT) regime when very thin ( $< 1 \, \mu m$ ) targets are used, both TNSA and RPA mechanisms are being observed [21, 22], revealing possibility to obtain proton energies up to 100 MeV [23].

# 1.1.2 Cavity Pressure Acceleration

In 2005, a concept of so-called Impact Fast Ignition (IFI) was proposed as an alternative scenario for direct-drive approach to ICF [24]. This approach is based on accelerating a fraction of independently compressed DT fuel in a hollow conical target, which then ignites pre-compressed fuel pellet. The key requirement for this scenario to be successful is very high velocity of the accelerated projectile (which will be from now on described as *macroparticle*), exceeding values of  $v_p > 10^8 \frac{cm}{s}$  while maintaining compression density in the range  $300 - 400 \frac{g}{cm^3}$  during impact. The main drawback of this method was poor hydrodynamic efficiency of the ablative acceleration (following so-called *rocket* model) of the impactor.

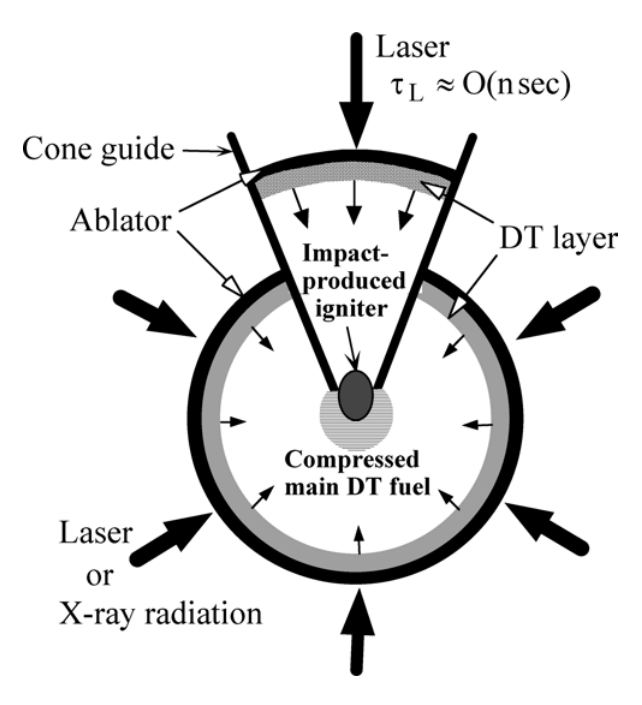


FIGURE 1.3: Schematic of Impact Fast Ignition method. Taken from [24]

In 2008 an alternative method of accelerating the flyer, named Reverse Acceleration Scheme (RAS) was demonstrated during an experimental campaign at Prague Asterix Laser System (PALS) in Prague, Czech Republic [25]. Briefly, the idea was to produce hot, expanding plasma during laser irradiation of the massive Cu target, which then served as a piston for thin Al foil, resulting in acceleration of the flyer without removing significant fraction of it's mass when using classic ablative acceleration approach (Fig. 1.4). In result, a velocity of the  $10~\mu m$  Al flyer equal to  $v_f = 1.3 \times 10^7~\frac{cm}{s}$  was obtained. Moreover, the accelerated foil mass appeared to be approximately constant during acceleration stage, as it was predicted in [26].

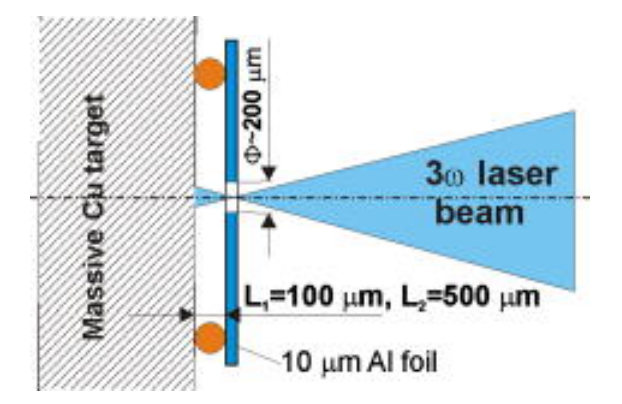


FIGURE 1.4: Initial experimental design of target for Reverse Acceleration Scheme. Taken from [25]

A year later, in 2009, the previously successful target design was further upgraded by implementing a cavity, which serves role of energy trap which confine and pressurize the plasma before accelerating the flyer [27] (Fig. 1.5). The confinement of the plasma inside the cavity proved to be very efficient way to accelerate not only thin foils, as described in previous experiment, but even heavy macroparticles ( $300 - 500 \, \mu m$  thick foil fragments). From now on, described mechanism of acceleration was referred to as Cavity Pressure Acceleration (CPA).

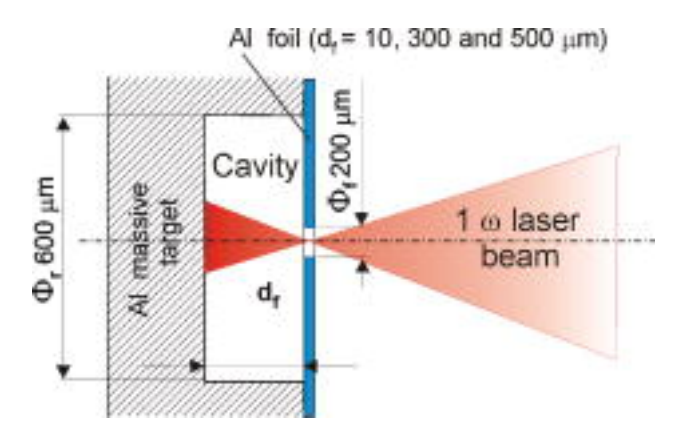


FIGURE 1.5: Reverse Acceleration Scheme target with cavity - the first Cavity Pressure Acceleration experimental design.

Taken from [27]

In 2011 another article devoted to CPA method was published. In contrary to Cavity Pressure Acceleration demonstrated previously, which is quite difficult to use in applications due to the direction of the accelerated macroparticle, during this experiment another variant of CPA, namely Forward Acceleration Scheme (FAS), was introduced [28] (Fig. 1.6).

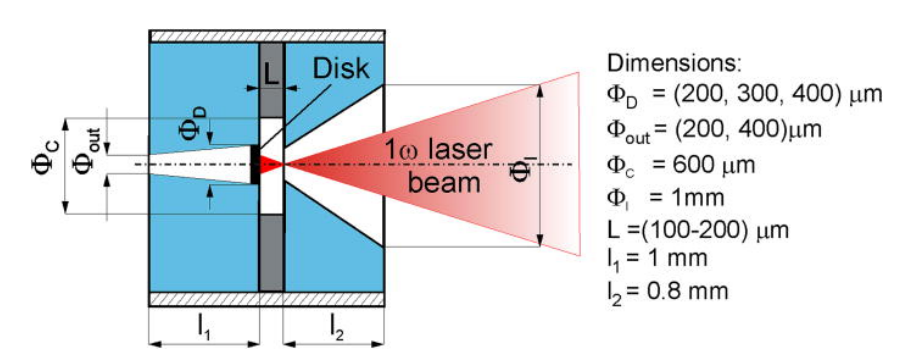


FIGURE 1.6: Target design for Forward Acceleration Scheme experiment. Taken from [28]

This approach allows to accelerate flyer disks in forward direction in the ablative acceleration manner, however the introduced conical exit channel guides and stabilizes the macroparticle and the cavity helps to sustain the high pressure of the plasma. Moreover, it was observed that covering the exit channel with thin metallic foil further increase the density of the projectile, however at the cost of macroparticle speed (Fig. 1.7).

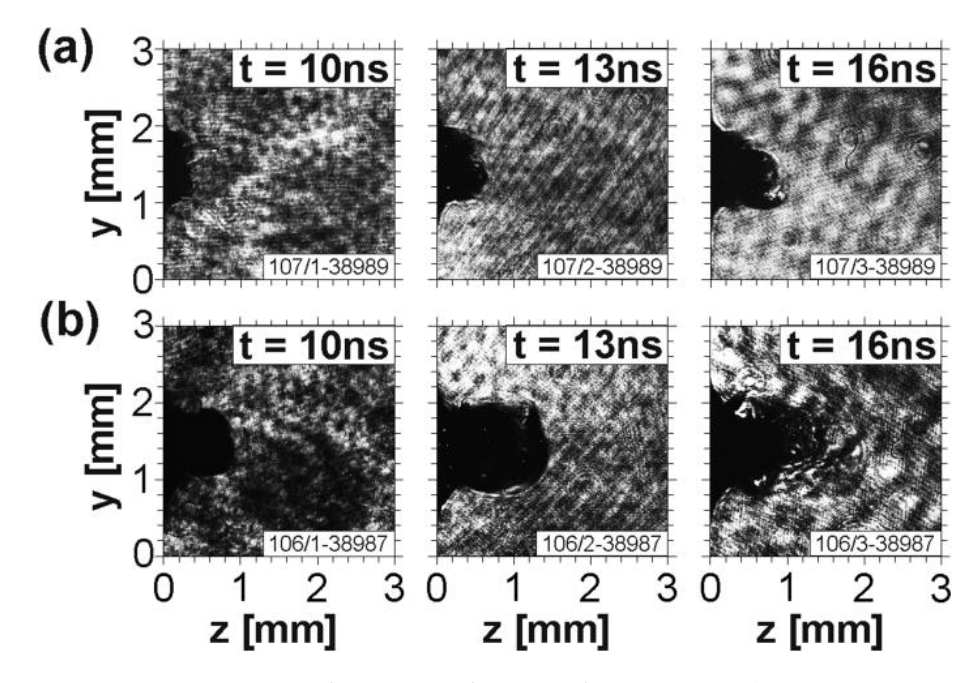


FIGURE 1.7: Interferometric frames of macroparticle propagation using open channel (a) and closed channel (b) of FAS type targets. Taken from [28]

The RAS method was also modified and tested during this experimental campaign. Instead of producing plasma by directly irradiating the cavity chamber wall, a low density (polystyrene (PS) or Al) ablator was mounted inside the cavity (Fig. 1.8).

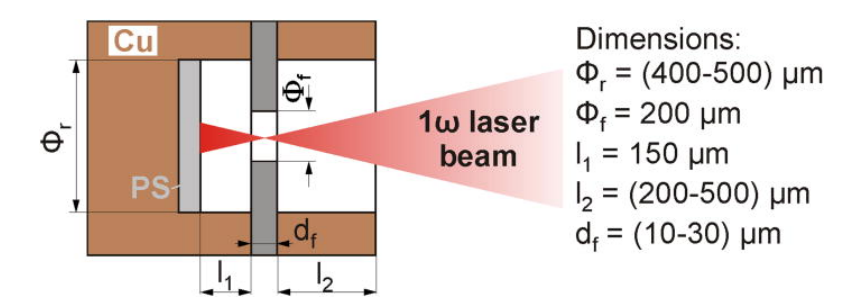


FIGURE 1.8: New Cavity Pressure Acceleration target design with low density ablator. Taken from [28]

This modification improved the measured velocity of the macroparticle comparing to previous findings of Borodziuk, resulting in  $v_f > 7 \times 10^7 \, \frac{cm}{s}$  for both 10  $\mu m$  Al and 20  $\mu m$  PS foils (Figure 1.9). Considering that at the time the highest velocity of flyer was obtained at NRL facility (Washington, USA) using krypton fluoride laser NIKE and 10.5  $\mu m$ 

thick CH foil targets [29], one can say that CPA method matched or even exceeded these results.

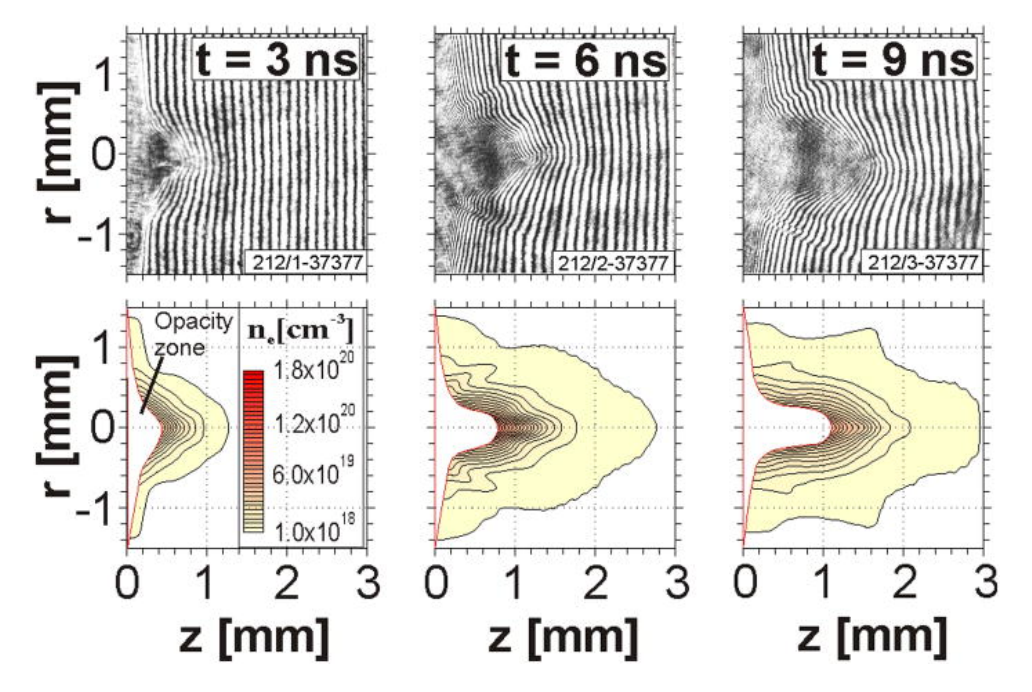


FIGURE 1.9: Measurement of macroparticle velocity using interferometric system for ablator-equipped cavity type targets.

Taken from [28]

Aside from already mentioned works, a similar concept of cavity-type target was also proposed in context of laser-ion acceleration rather than macroparticle acceleration, formerly called LICPA (Laser Induced Cavity Pressure Acceleration). In this approach, the light of ultra-high intensity  $(I_L > 10^{20} \frac{W}{cm^2})$ irradiates thin, sub-micron thick target which is placed inside the cavity. At such high intensities, the ion acceleration is dominated by so-called Radiation Pressure Acceleration (RPA) mechanism, in which the target bulk is accelerated instead of contaminants at it's rear side [30]. The introduction of the cavity allows the light to reflect back into the target, which results in an increase of both energy conversion (between laser pulse and the ions) and maximum energies of ions up to a few times higher comparing to the conventional RPA approach [31]. It was also experimentally proven that following LICPA approach, shocks characterized by Gbar level of pressure and over 100km/s velocity can be obtained (Fig. 1.10), which are of great importance for inertial fusion energy research in terms of equation-of-state of matter in extreme conditions [32].

In 2020, roughly 10 years after last experimental activities regarding CPA

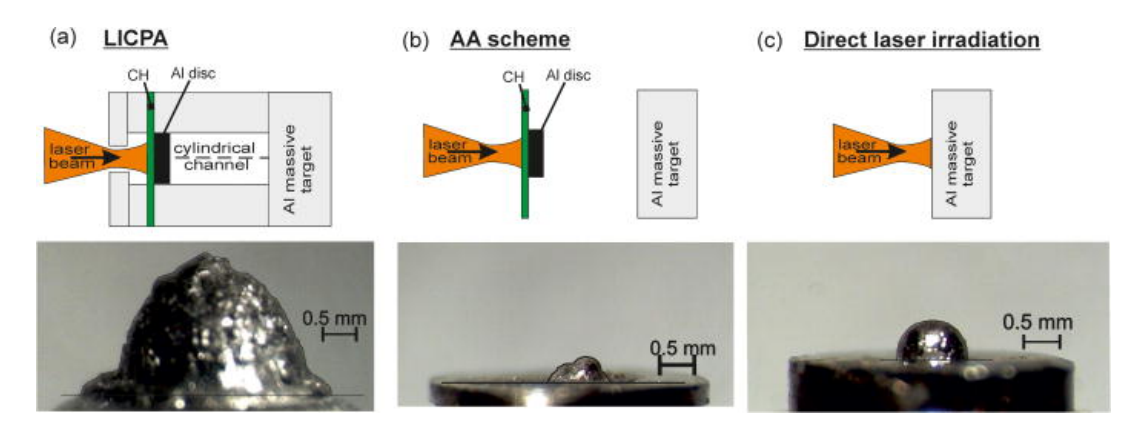


FIGURE 1.10: Dimensions of craters created during impact of LICPA-accelerated flyer (a) in comparison to ablative acceleration (b) and direct laser irradiation (c). Taken from [32]

scheme, the idea was revisited with slightly different setup. Instead of metallic flyers, deuterated polyethylene  $CD_2$  was used [33] (Fig. 1.11). This addition allowed to verify that the energy of released plasma stream is sufficient to enable  $D + D \rightarrow {}_2^3He + n$  reaction and diagnose the impact conditions similarly to work of Karasik et al. [29]. Similar to previous experiments with CPA method [28], a channel was introduced to improve acceleration process. In result, the observed neutron yield of  $N_n \approx 3 \times 10^6$  was comparable with yield values obtained in laboratories equipped with shortwavelength lasers of significantly higher energies.

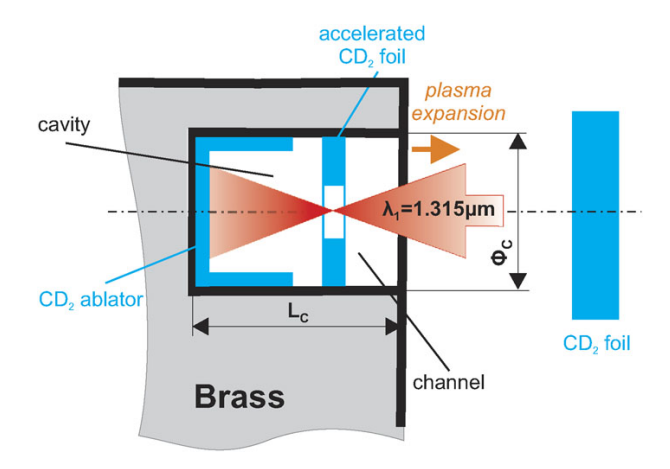


FIGURE 1.11: Latest iteration of Cavity Pressure Acceleration targets suitable for neutron production. Taken from [33]

In 2022 the most recent CPA related experiment was performed at PALS laboratory, resulting in extraordinary results (yet to be published) in regard of neutron production, placing CPA method among the most efficient experiments devoted to generation of neutrons using lasers. Importantly, unusual at first, streams of very energetic protons ( $E_{max} > 4 \, MeV$ ) were observed. The

explanation of generation and potential application of these proton beams are fundamental for this thesis and will be covered in greater detail in 2.1 and 3.2.1.

# 1.1.3 Proton - boron fusion scenario - laser-based approach

Despite recent scientific breakthroughs, both in Magnetic Confinement Fusion and Inertial Confinement Fusion, the fusion in which DT fuel is used faces severe challenges, related to both engineering and general physics. Availability, breeding and on-site managment of tritium, as well as the radiation damage caused by high-energy neutrons created during this fusion scenario and activation of materials used to build reactor are the biggest concerns of this approach. Awareness of these issues is the main motivation to pursue alternative approaches in attempt to simplify the road to commercial fusion energy.

Reaction	$\sigma_{10kev}$ (barn)	$\sigma_{max}$ (barn)	$E_{CoM}$ at $\sigma_{max}$ (keV)	Q (MeV)
$D+T \rightarrow {}^{4}He+n$	$2.72 \times 10^{-2}$	5.0	64	17.59
$D+D \rightarrow T+p$	$2.81 \times 10^{-4}$	0.096	1250	4.04
$D+D \rightarrow {}^{3}He+n$	$2.78 \times 10^{-4}$	0.11	1750	3.27
$T+T \rightarrow \frac{4}{2}He+2n$	$7.90 \times 10^{-4}$	0.16	1000	11.33
$D + {}^{3}He \rightarrow {}^{4}_{2}He + p$	$2.2 \times 10^{-7}$	0.9	250	18.35
$p + {}^{6}Li \rightarrow {}^{4}_{2}He + {}^{3}He$	$6 \times 10^{-10}$	0.22	1500	4.02
$p + {}^{11}B \rightarrow 3_2^4 He$	$4.6 \times 10^{-17}$	1.2	675	8.68

TABLE 1.1: Table of considered fusion reactions cross-sections for future power plants

One of the most interesting known fusion reactions is synthesis of proton and boron, which leads to production of three alpha particles carrying total energy of 8.76 MeV. The crucial aspect of this fusion scenario is absence of the neutrons among the products, which eliminates issue of material activation and limits nuclear waste. Another advantage of proton-boron fusion is that only abundant and stable isotopes are required, therefore no breeding, radiation protection and special security requirements need to be adressed, contrary to reactions involving tritium. These properties are the reason for considering  $p + {}^{11}B$  reaction as a "holy grail" of fusion energy [34].

Despite all the advantages, due to requirement of sustaining extreme temperatures of plasma in order to achieve ignition, proton-boron fusion field did not receive as much attention as DT fusion and in result was abandoned by majority of groups. However, due to rapid growth and advancements of

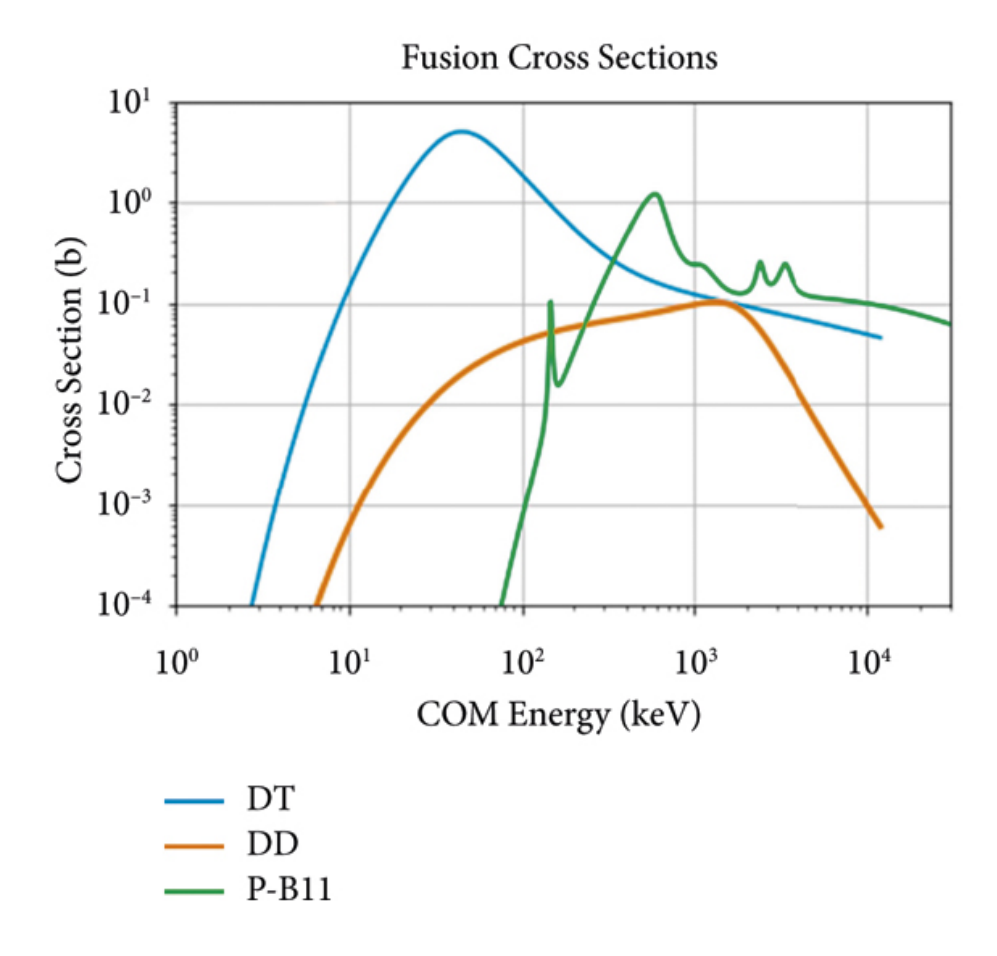


FIGURE 1.12: DT, DD, and P-B11 cross-sections. Taken from [35]

laser technology, in the last decade a number of experiments demonstrated possibility of obtaining high  $\alpha$  particle yields during interaction of intense laser pulses with materials containing isotopes of boron.

The beginning of the revival of aneutronic fusion experiments dates back to 2005, when for the first time production of alpha particles in thermonuclear reaction  $^{11}B(p,\alpha)^8Be$  was experimentally observed [36], resulting in  $N_\alpha=2\times 10^5\,sr^{-1}$  yield of alpha particles. In this case, laser pulses of energy up to 15 J, wavelength of 1.055  $\mu m$  and pulse duration 1.5 ps were used to irradiate either 300  $\mu m$  or 500  $\mu m$  thick composite targets  $^{11}B+(CH_2)_n$  (50% of weight being  $^{11}B$ ). The next experimental evidence of  $\alpha$  production from  $p+^{11}B$  reaction was published 3 years later, using ABC laser (Frascati, Italy) of intensity on the level of  $3\times 10^{15}\frac{W}{cm^2}$  ( $E_L\approx 100\,J$ ,  $\tau_L\approx 2\,ns$ ) and resulting in  $N_\alpha\approx 10^4\,sr^{-1}$  [37]. In both of these experiments, the proton acceleration and alpha production took place in the volume of the single target, thus such experimental setup is often referred to as in-target.

Several years later, another approach was presented by Labaune et. al

[38]. The alpha production in this case was separated into two stages. Firstly, acceleration of protons from solid, thin foils (both Al or CH targets were used) by means of TNSA mechanism was performed using laser pulses delivering 20 J in 1 ps at 0.53  $\mu m$  wavelength. Then, interaction of produced proton beam with secondary, natural boron target placed 1.5 mm away took place. The secondary target was either solid or irradiated with 400 J, few ns, 0.53  $\mu m$  laser light in order to produce boron plasma before interaction with protons. This new two-staged approach, resembling beam-target experiments, resulted in orders of magnitude higher then previously alpha yield the highest measured fusion rate reached  $N_{\alpha} = 9 \times 10^6 \, sr^{-1}$ . Such configuration of primary (pitcher) and secondary (catcher) target is often referred to as pitcher-catcher.

From that point on numerous successful experiments were performed [39, 40, 41, 42, 43, 44] (Fig. 1.13), following either *in-target* or *pitcher-catcher* scenarios. Currently, the highest reported number of produced alpha particles in aneutronic reaction experiments is reaching  $N_{\alpha} \approx 10^{11}$  [42].

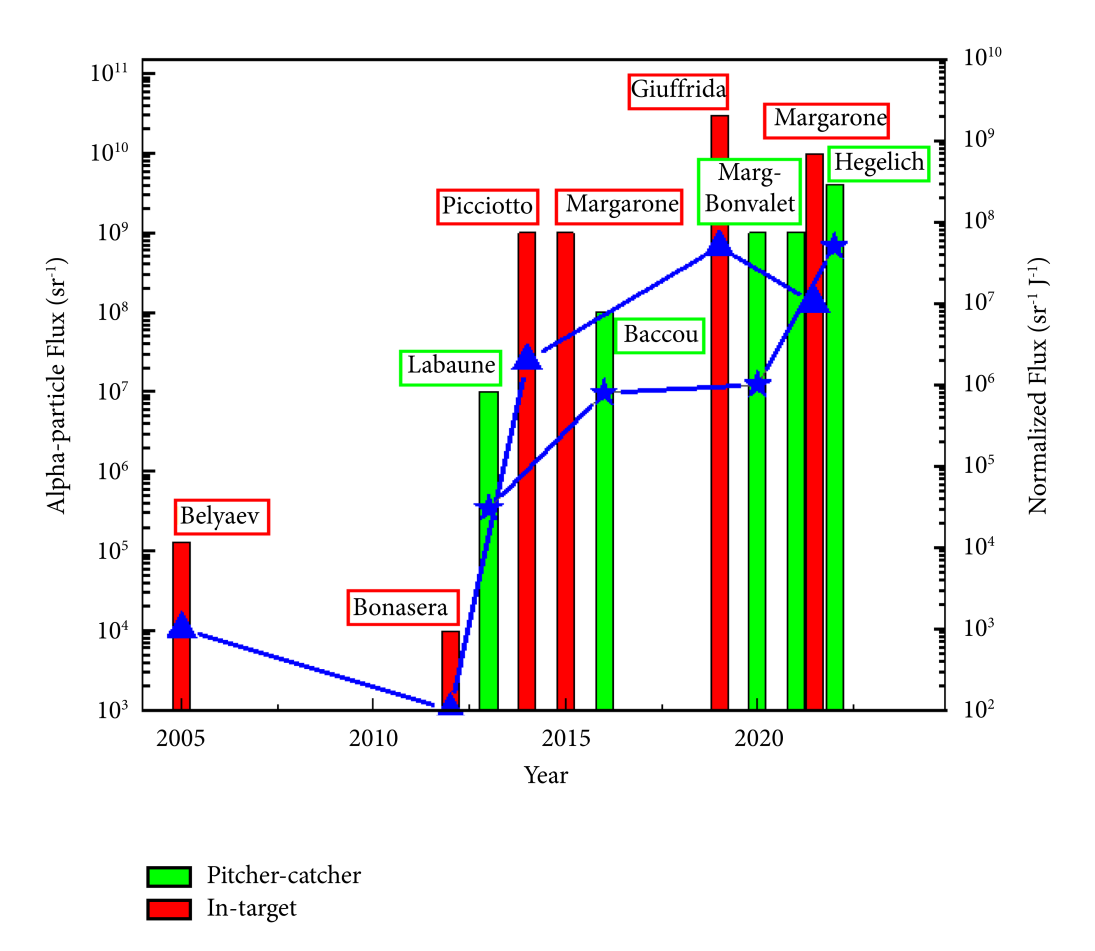


FIGURE 1.13: Progress of alpha particle production in laser-based experiments in past years. Taken from [35]

Although successive increase of alpha yield over the last few years is impressive, these values are still far from obtaining the scientific breakeven level of fusion reactions rate. Taking into consideration the Q-value of  $p + {}^{11}B$  reaction equal to  $Q = 8.76 \, MeV$  and the fact that so far best results were obtained using kJ-class laser systems, one would need to produce  $2.15 \times 10^{15}$  alpha particles to reach energy output equal to energy input of  $1 \, kJ$  [35], meaning that the current maximum normalized yield is at  $10^{-4}$  of this value. To close the gap between what's achievable and what has to be achieved, novel approaches to both targetry and proton beam production in proton-boron reaction have to be developed and tested.

#### 1.1.4 Thesis statement

Except for the work of Labaune et al. [38], the success of all recent experiments devoted to proton-boron fusion and increase of fusion rate and alpha yield was possible mostly as a result of increasing the laser pulse intensity by exploiting up to PW-class laser systems which provide hundreds of Joules in times as short as single femtoseconds. Higher intensities of laser pulse allow to increase the maximum energy, as well as the number of accelerated protons that undergo the reactions with atoms of boron. Despite the possibility of employing thick boron catchers, which in principal slow down the protons as they propagate through the bulk of boron in order to increase amount of particles with favoured energy to initiate  $p + {}^{11}B$  reaction, significant number of the protons is crossing the target without producing alpha particles even when few milimeters catchers are used [43]. Additionally, due to short range of alpha particles in materials (assuming energy of 10 MeV, which is the maximum energy of experimentally observed alpha particles produced in proton-boron reaction [44], the  $\alpha$  range inside <sup>11</sup>B is roughly 50  $\mu$ m), remarkable amount of fusion products are not leaving the catcher's bulk.

All of the above lead to conclusion that using thin, tens of micrometer thick catchers and increasing the number of protons in the energy range 0.675 - 5 MeV is the most efficient approach to proton-boron fusion using lasers. Basing on recent experimental results obtained with Cavity Pressure Acceleration method (described in detail in Section 3.2.1), the statement of this thesis can be formulated as follows: The intense proton beam generated through thermonuclear reaction of D + D via Cavity Pressure Acceleration method allows to more efficient generation of alpha particles by means of  $p + {}^{11}B \rightarrow 3\alpha$  fusion reaction comparing to

standard approach to laser ion acceleration methods using TW-class laser system.

In order to confirm and verify this thesis, proton beams obtained both in TNSA and CPA approach were characterized using Thomson Parabola Spectrometer during experimental campaigns using TW-class laser systems. Afterwards, a set of Monte Carlo simulations were performed, where interaction of both proton beams with different boron targets were benchmarked in terms of alpha production in  $p+^{11}B \rightarrow 3\alpha$  reaction using code FLUKA [45] in search of the optimal thickness for maximizing the alpha particle emission, where both pure boron-11 and natural boron were chosen as the material. The output of the simulations were compared for TNSA- and CPA-produced proton beam, based on which final conclusions were formulated.

# 2 Characterization of CPA-accelerated ion beams and their interaction with boron target

# 2.1 Radiative-hydrodynamic simulations of lasermatter interaction employing cavity geometry

In the approach depicted in this thesis, generation of high energy ion beams by means of Cavity Pressure Acceleration mechanism is realised via one of the deuterium-deuterium fusion channels in which 3 *MeV* proton is produced. This reaction can be either driven by collisions of deuterium ions realised in so-called "beam-target" scenario, where accelerated ions collide with cold, solid-state, deuterium-rich target foil, or in volume of the plasma where thermonuclear reactions occurs. The latter solely relies on maintaining thermodynamical parameters of the plasma (such as density, pressure and temperature) on sufficient level during the time of confinement of the plasma.

While applying Cavity Pressure Acceleration mechanism in DD fusion, depending on the chosen geometry and variant of the cavity (either the ablator-flyer configuration as in the [28, 33] or powder-based configuration described later in 3.2.1) both of these scenarios are contributing to the production of protons and neutrons with different weight. In case of early designs of the cavity targets, due to the plasma-turned ablator colliding with flyers, beam-target effects are dominant. If the simplified design is used, in which ablator is replaced with a layer of deuterated plastic-based powder, the character of the fusion is mainly thermonuclear and the beam-target contribution is negligible.

In both cases the proper choice of cavity geometry is required, depending on the laser pulse parameters that are going to be applied in particular laser-matter interaction, for optimization of the parameters responsible for maximizing the nuclear reaction rate. Due to numerous effects that are crucial for the efficiency of the CPA mechanism, such as physics related to plastics and stress of materials, electromagnetic phenomena, particle production, equation of state (EOS), propagation of shock wave fronts, thermal conductivity, ionization and recombination of a medium, radiation losses, inverse bremsstrahlung, magneto-hydrodynamics and multilayer structure of irradiated targets, numerical modelling of plasma state inside the cavity is very important aspect of preparatory stage of the experiment. To picture the importance of proper choice of the cavity geometry, and at the same time to demonstrate how the laser-matter interaction and created plasma state changes by applying cavity geometry, results of numerical simulations of high-power, nanosecond laser pulse interaction with two cavity targets will be discussed below based on the results of the FLASH code [46] simulations.

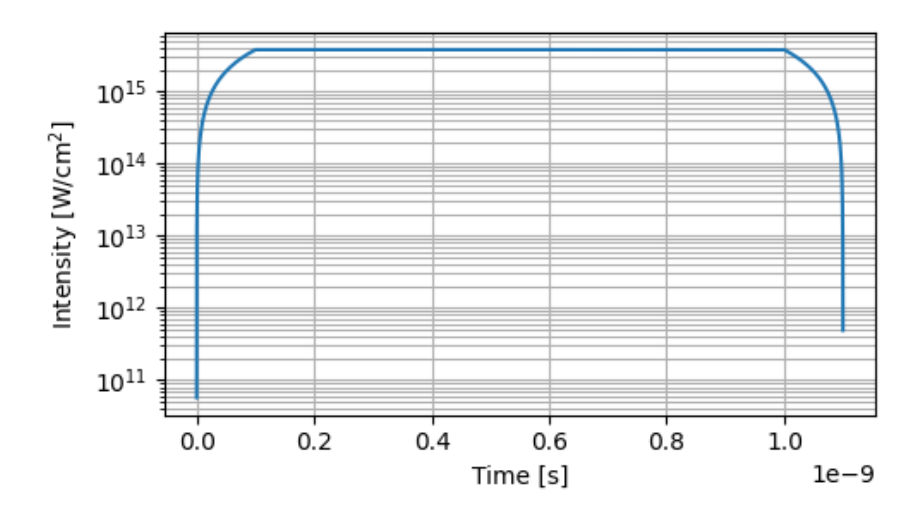


FIGURE 2.1: Temporal profile of laser pulse used for simulations of laser-matter interaction with cavity targets using nanosecond, kJ-class laser system

Laser pulse of  $\tau=1$  ns duration (with 100 ps build-up time as shown on Figure 2.1),  $E_L=300$  J of energy, focal spot diameter equal to  $d=100~\mu m$  and wavelength  $\lambda=532~nm$  was used to irradiate two cavity-type targets of different geometries. The reason of choosing the nanosecond pulse duration at given energy is to mimic the L4n laser system located in Dolní Břežany (Czech Republic) which belongs to the ELI Beamlines facility. In both cases the cavity was made of copper (assumed initial density  $\rho_{Cu}=10\frac{g}{cm^3}$ ) and layer of polyethylene powder (to mimic structure of powder, the initial average density was assumed to be  $\rho_{PE}=1\frac{g}{cm^3}$ ) deposited inside the cavity -

however the thickness of the polyethylene layer and the diameter of the cavity was varying (Fig. 2.2). The laser was focused centrally on the surface of the polyethylene volume (propagating from z = 0 to higher values).

Cavity geometry	Length [µm]	Diameter [µm]	Polyethylene thickness [ $\mu m$ ]
A	300	700	300
В	300	200	300

TABLE 2.1: Dimensions of cavity "A" and "B" discussed in this paragraph

The simulation time was equal to  $3\,ns$ , during which values of three thermodynamic quantities were tracked: density  $\rho$  in units of  $\frac{g}{cm^3}$ , electron temperature  $T_e$  in Kelvins (later converted to keV) and pressure P in units of Barye (centimeter-gram-second unit system, later in the text converted to bar for easier interpretation when time-dependent plots will be displayed). Although only half of the cavity is displayed on all the presented below graphs, due to cyllindrical symmetry the values are representing correct values for the whole cavity.

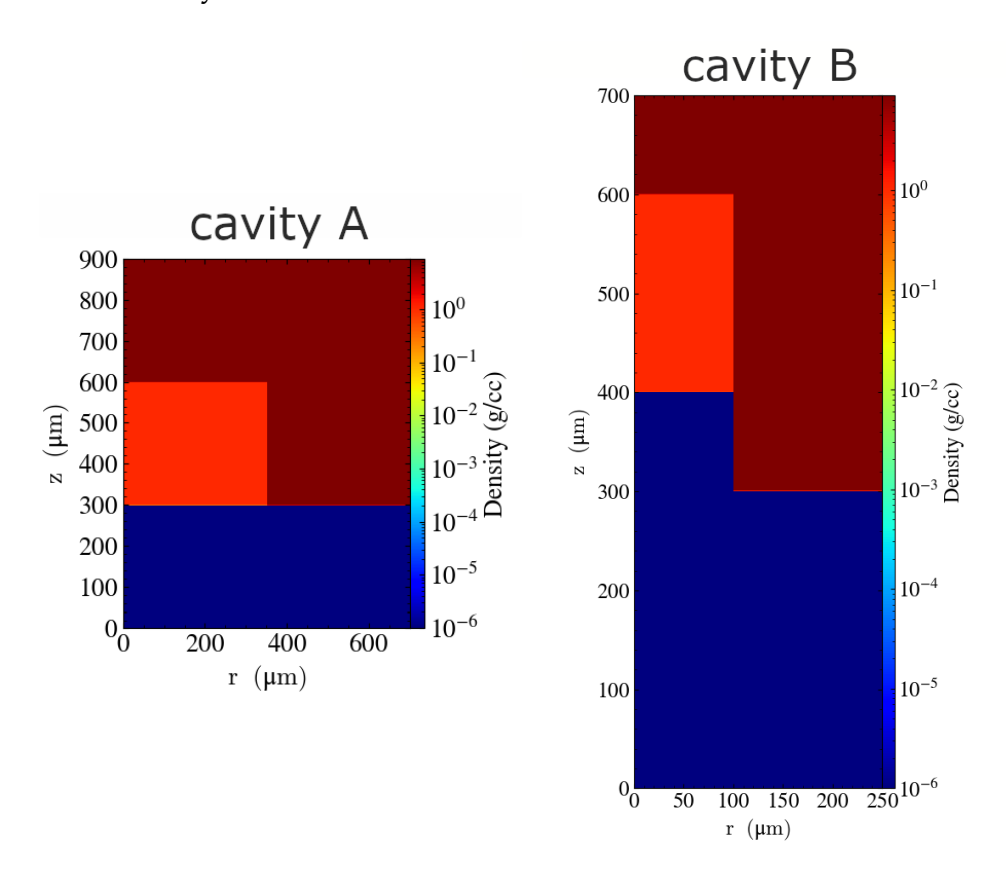


FIGURE 2.2: Initial 2D density distribution of cavity "A" (left) and cavity "B" (right)

In case of cavity "A", the polyethylene layer of 300 µm thickness filled entire volume of the cavity channel. During the duration of the pulse, one can observe the front of the shockwave propagating inside the volume of the fuel, followed by creation of plasma and increase of the pressure and the temperature of the ionized material (Figure 2.3). After the interaction is finished, all of the parameters values start to decrease as the plasma expands (Figures 2.4, 2.5, 2.6). The notable feature of this case, visible on distribution of every tracked parameter, is diffraction of expanding plasma on the joint surface between polyethylene layer and copper housing wall. However, the evolution of the plasma parameters does not exhibit a notable influence of the cavity geometry (of given dimensions) from what one could expect from interaction of the laser pulse with the flat target. It becomes clear that in the described case the physics related to Cavity Pressure Mechanism are not present due to overfilling the cavity with the polyethylene, which prevented the build up of pressure and collisions of plasma corona with cavity walls that otherwise would lead to formation of shockwaves propagating through plasma plume.

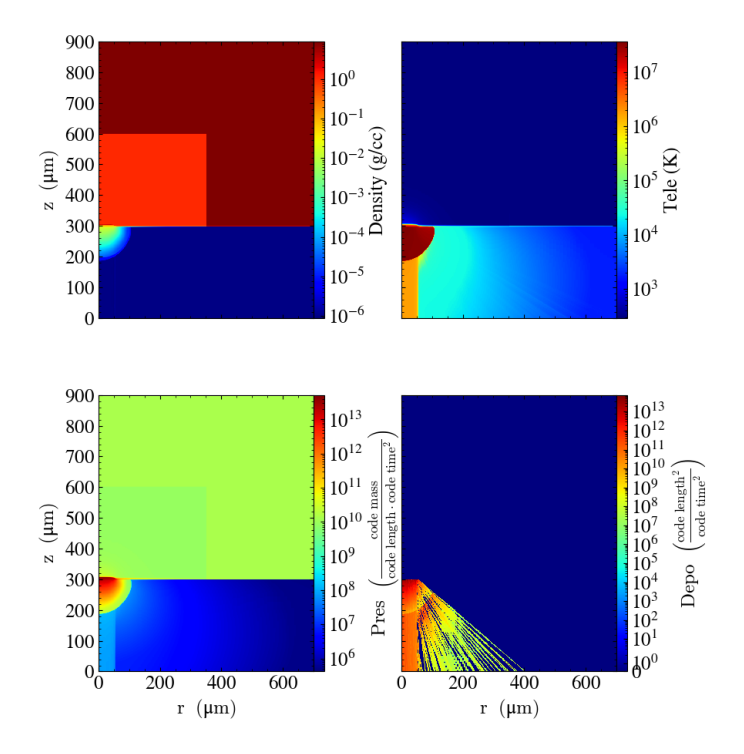


FIGURE 2.3: 2D distributions of density (upper left), electron temperature (upper right), pressure (bottom left) and deposited laser energy (bottom right) for cavity "A" at 100 *ps* of simulation time

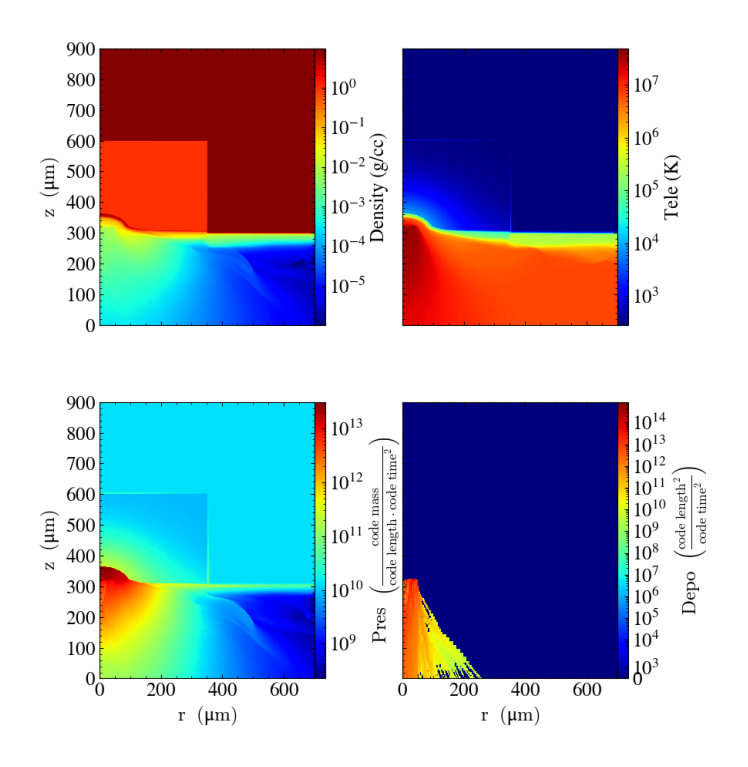


FIGURE 2.4: 2D distributions of density (upper left), electron temperature (upper right), pressure (bottom left) and deposited laser energy (bottom right) for cavity "A" at 1 ns of simulation time

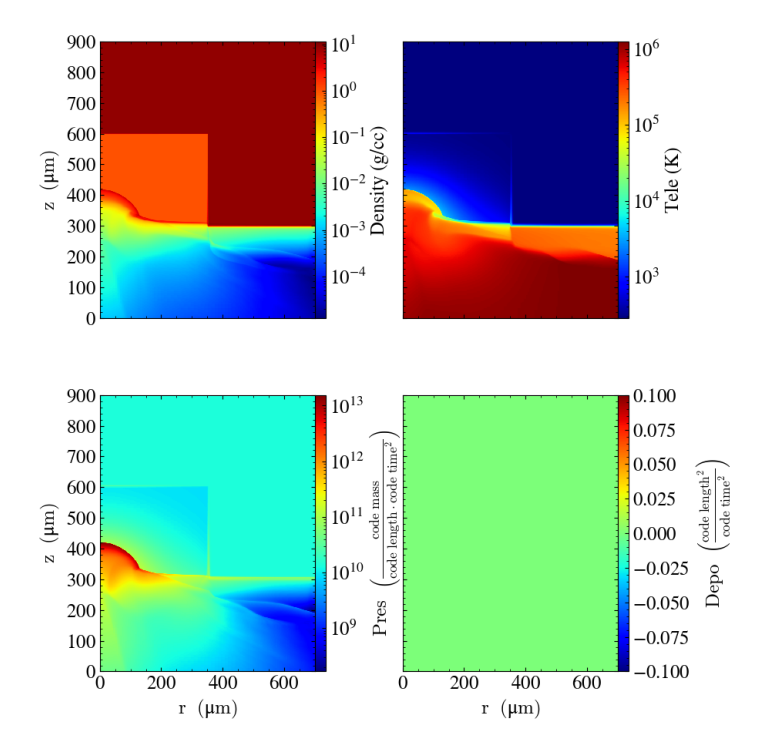


FIGURE 2.5: 2D distributions of density (upper left), electron temperature (upper right), pressure (bottom left) and deposited laser energy (bottom right) for cavity "A" at 2 ns of simulation time

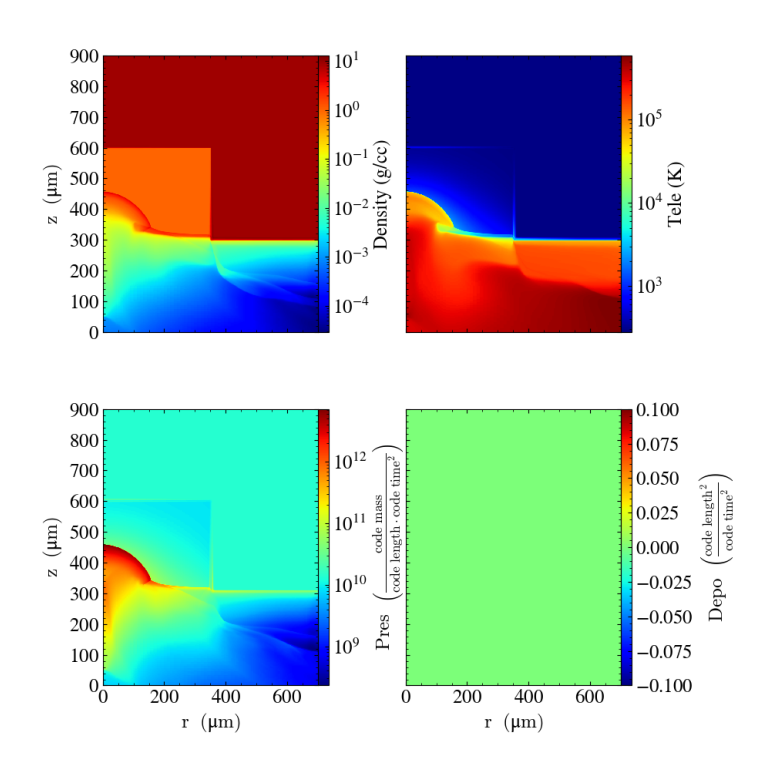


FIGURE 2.6: 2D distributions of density (upper left), electron temperature (upper right), pressure (bottom left) and deposited laser energy (bottom right) for cavity "A" at 3 *ns* of simulation time

In case of the cavity "B" geometry, the plasma behaviour exhibits several phases of its evolution. In the very early stage of the interaction, due to the narrow cavity channel equal to  $200 \, \mu m$ , the expanding polyethylene plasma is colliding with the walls of the cavity, driving additional shockwaves which are reflecting back into the plastic plasma volume (Fig. 2.7). This marks the beginning of the heating phase, in which  $T_e$  rapidly increases and is maintained on maximum level for the duration of the pulse. At the same time, the density reaches critical value and prevents further penetration of laser pulse inside the cavity, which can be seen by difference of depths at which the laser energy is deposited (bottom right part of Figure 2.7, 2.8(a) and 2.8(b)).

After 1 nanosecond, the plasma is released and the temperature starts to decrease. In this phase of plasma evolution, the notable increase in both pressure and density is observed, ultimately leading to formation of dense, compact plasma jet which propagates outside. Basing on these findings, it is evident that the fronts of shockwaves which are partially reflected from the high-Z material of cavity walls are of great importance for designing optimal cavity target for particular laser system - the lateral distances between interaction point and cavity walls are determining the timing of increase of the electron temperature, which is one of the most important physial quantities

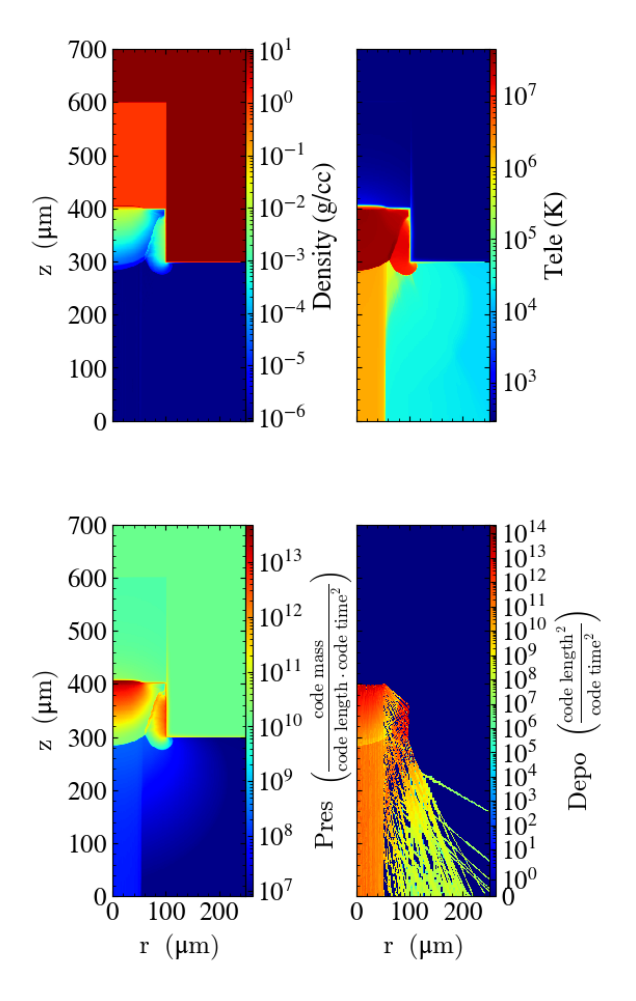


FIGURE 2.7: 2D distributions of density (upper left), electron temperature (upper right), pressure (bottom left) and deposited laser energy (bottom right) for cavity "B" at 100 *ps* of simulation time

in terms of driving nuclear reactions. In the most optimal scenario, the temperature spike should occur when the density of the plasma is the highest in order to maximize the number of expected nuclear reactions when deuterated polyethylene is used.

To better understand the dynamics of plasma evolution in these two cases, maximum values of density, electron temperature and pressure obtained along the z axis were plotted versus time of the simulation, where the first dashed line marks the end of laser-matter interaction  $(t_1)$  and the second represents the peak of maximum pressure (equal to  $P_{max}=0.115~GBar$  obtained for cavity "B"  $(t_2)$ , at which the density remains at the maximum of  $\rho_{max}=14\frac{g}{cm^3}$  (Figure 2.9). The time delay between the end of the laser pulse and the peak of both pressure and density is equal to  $\Delta t=t_1-t_2=1.2~ns$ .

The values presented in Figure 2.9 show at least two-fold increase in all of the tracked parameters when cavity of smaller diameter and thinner layer

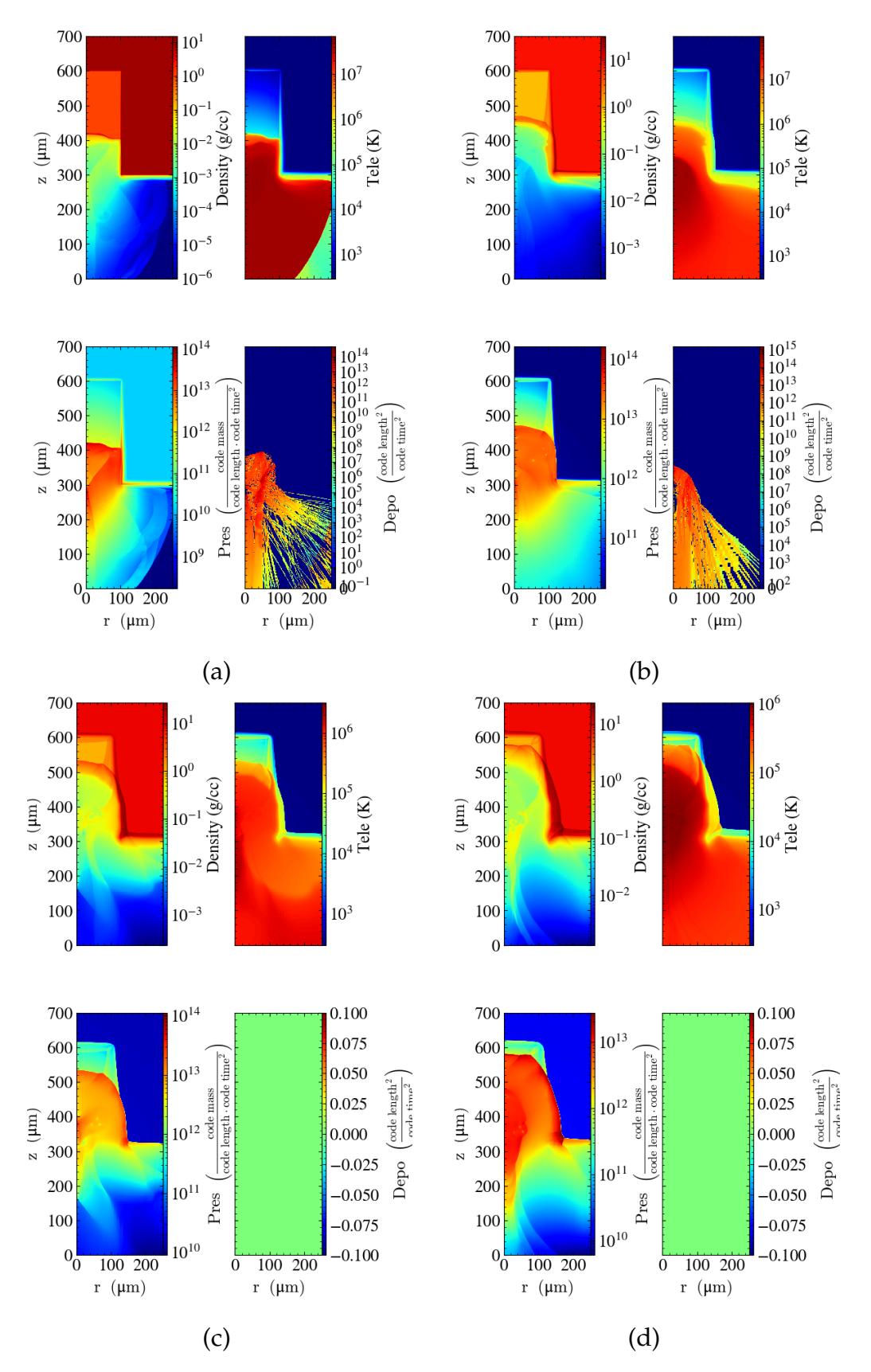


FIGURE 2.8: 2D distributions of  $\rho$  (upper left),  $T_e$  (upper right), P (bottom left) and deposited laser energy (bottom right) for cavity "B" at: (a) 300 ps, (b) 1 ns, (c) 2 ns and (d) 3 ns of simulation time

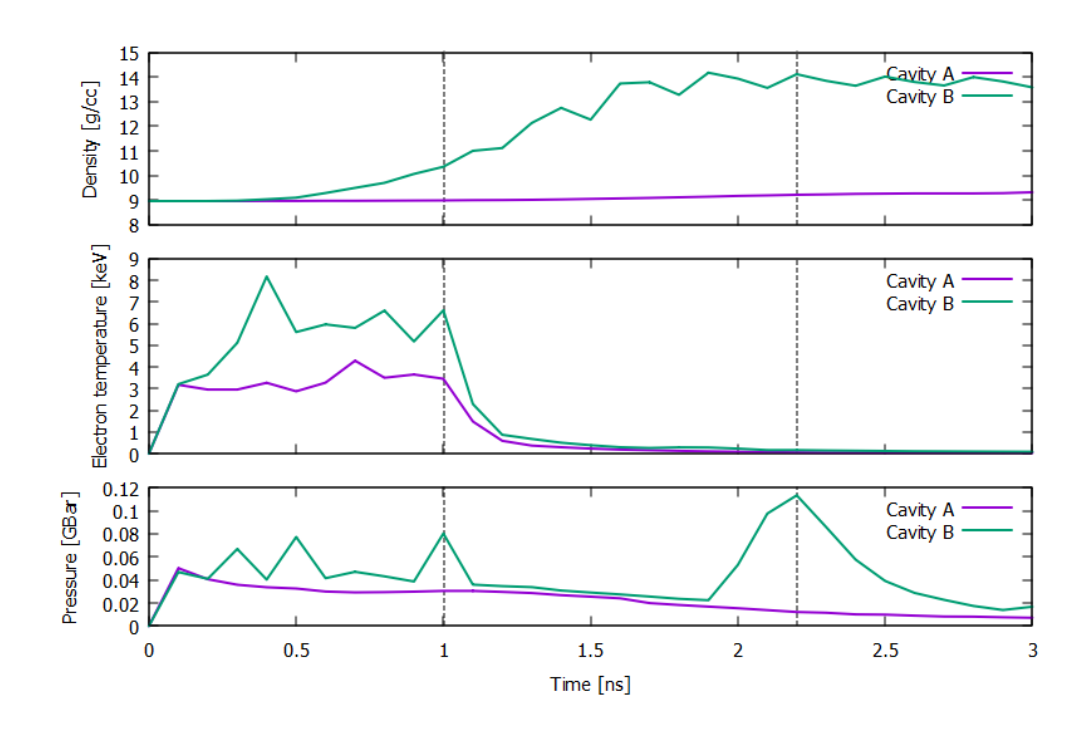


FIGURE 2.9: Time evolution of maximum values of thermodynamic parameters during simulation time for cavity geometries A and B

of the polyethylene is used. The conclusion based on this comparison is that precise designing the cavity geometry for particular laser system is required to maintain optimal environment for driving nuclear reactions following Cavity Pressure Acceleration scheme.

## 2.2 Thomson Parabola Spectrometer (TPS)

Although recently PW-class laser systems are bringing attention of majority of the people working in laser-plasma field of physics, current advent of proton-boron-related research encourages scientists to revisit possibilities of generating ion beams using laser systems which for a long time were not considered as tools capable of being used in efforts of bringing clean, fusion energy to life. One of the properties of aforementioned  $p + {}^{11}B$  reaction is relatively low center-of-mass energy of the protons at main peak of the reaction cross-section (675 keV) compared to other widely considered fusion schemes, at the same time being based only on stable isotopes (Fig. 1.12).

Present day laser systems designed for laser-plasma research are in most cases capable of providing protons of such energy via different laser ion acceleration scenarios, one of which is the most explored so far Target Normal Sheath Acceleration (TNSA) approach, where ponderomotive forces which arise during laser pulse interaction with solid, thin foil targets, accelerate electrons which form sheath behind the target. As they propagate, due to charge separation, light contaminant ions located on the rear of the foil are being accelerated as well. This phenomena is commonly observed using terawatt, femtosecond long laser pulses.

Such laser system is located at in High Power Laser Laboratory, laser-oriented division of Institute of Plasma Physics and Laser Microfusion, Poland. "Pulsar 10TW" is able to provide approximately 0.4J energy (after compression), 40fs pulse duration, resulting with 10 TW of effective power. It was designed to perform laser ion acceleration-related experiments and has been used in multiple laser-plasma studies over the last decade [47, 48, 49, 50]. Recently, as an addition to arsenal of diagnostics used during the experiments, our team designed and developed Thomson Parabola Spectrometer (TPS), a diagnostic tool widely used in the laser-plasma research, which allowed observation of phenomena crucial for this work.

## 2.2.1 Principal of TPS operation

Thomson parabola spectrometer is a diagnostic device which uses magnetic and electric field to deflect charged particles from their initial path by means of Lorentz force (Eq. (2.1), (2.2), (2.3), where  $D_B$  is deflection by means of magnetic field,  $D_E$  is deflection by means of electric field,  $L_B$  and  $L_E$  are lengths along z-axis over which respective fields are applied and  $d_E$  and  $d_B$  are distances between the end of the electric and magnetic fields and the detector, respectively). Due to multispecies character of laser-accelerated ion beams and wide range of velocities of these particles, applying such fields in principal results with multiple parabola-like tracks registered on the detector of choice. Each of these parabolas represent ions with given charge-to-mass ratio  $\frac{q}{m}$ , where  $\frac{q}{m} = 1$  corresponds to hydrogen ions (protons).

$$\vec{F} = q\vec{E_{El}} + q(\vec{v} \times \vec{B}) \tag{2.1}$$

$$D_B = \frac{qBL_B}{mv_z} (\frac{1}{2}L_B + d_B)$$
 (2.2)

$$D_E = \frac{qEL_E}{m{v_z}^2} (\frac{1}{2}L_E + d_E)$$
 (2.3)

In classic design of TPS, the electrodes responsible for generation of electric field are parallel to each other, granting constant electric field along their length.



FIGURE 2.10: Raw image of deflected parabolas registered with multi-channel plate and a camera at High Power Laser Laboratory (IPPLM, Warsaw)

However, considering recent increase of available laser intensities and multiple experiments demonstrating capability of acceleration protons up to hundred of mega-electronvolts [51], this approach would require ten of kilovolts of voltage to maintain reasonable level of dispersion and thus separation of accelerated particles. As a consequence, majority of modern TPS employ wedge configuration of electrodes, following the design proposed by scientists from CLF, UK [52].

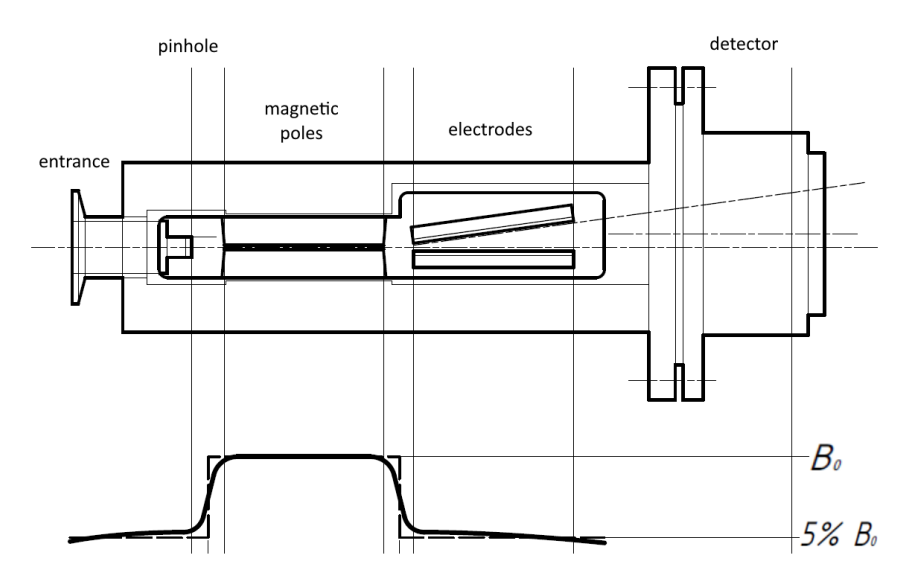


FIGURE 2.11: Schematic of Thomson Parabola Spectrometer designed at IPPLM (up) together with magnetic field profile measured along magnetic poles (down)

This configuration allows to maintain the same level of deflection while applying lower voltage than in traditional approach. However, due to varying electric field along the electrodes, equations (2.2) and (2.3) are no longer applicable. Instead, the software designed by an author of this thesis to analyze the TPS results relies on a particle tracking algorithm, where a set of points (x,y,E) is obtained by solving equations iterating over user defined range of energies:

$$\begin{cases} \frac{qU}{d(z)} = m_i \ddot{x} \\ qv_z B = m_i \ddot{y} \end{cases}$$
 (2.4)

where q and  $m_i$  are respectively the charge of considered ion specie and its mass, U is the applied voltage, d(z) a distance between plates at given z position,  $v_z = \sqrt{\frac{2E}{m_i}}$  is the velocity of ion along z-axis. The algorithm takes  $d(z) = A \cdot z + B$ , where  $A = \frac{d_2 - d_1}{Ze_2 - Ze_1}$ ,  $B = d_1 - A \cdot Ze_1$ , where  $d_2$  and  $d_1$  are the distances between plates at the beginning and the end of the electrodes,

 $Ze_1$  and  $Ze_2$  beginning and the end of electrodes in respect to the entrance pinhole. Such model assumes linear decrease of electric field along the electrodes and that there is no electric field outside of the plates. The technical aspects of this particular TPS device were presented in a greater detail in a recently published paper [53].

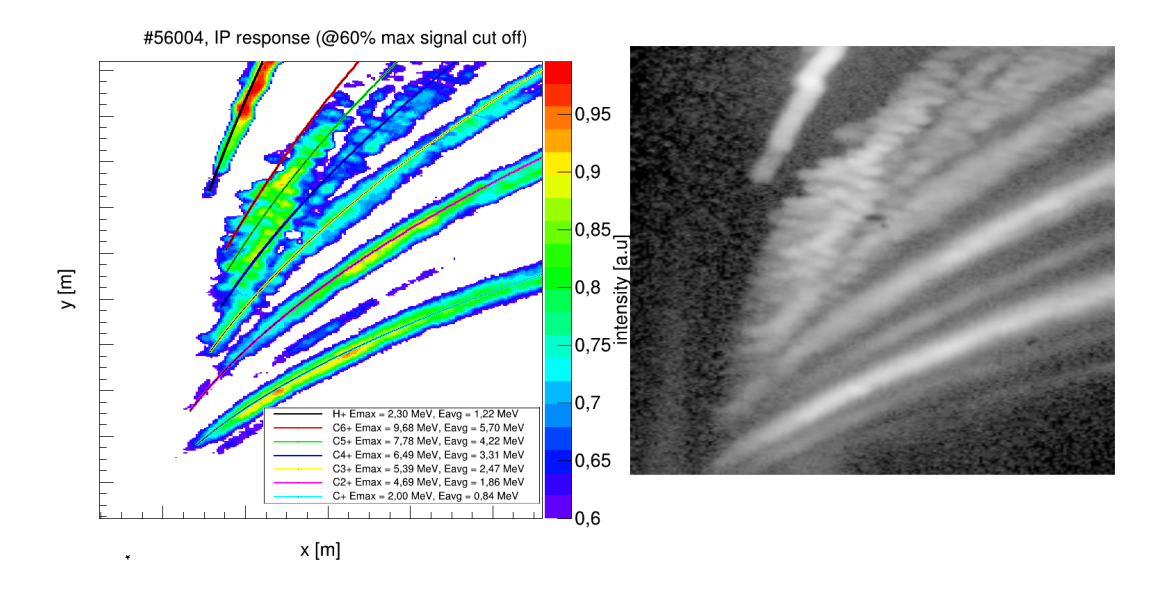


FIGURE 2.12: Left: Fit of theoretical parabolas to high-energy part of parabolas of different ions registered using Image Plate during one of experiments performed at Prague Asterix Laser System (CZ). Right: Corresponding area of original image

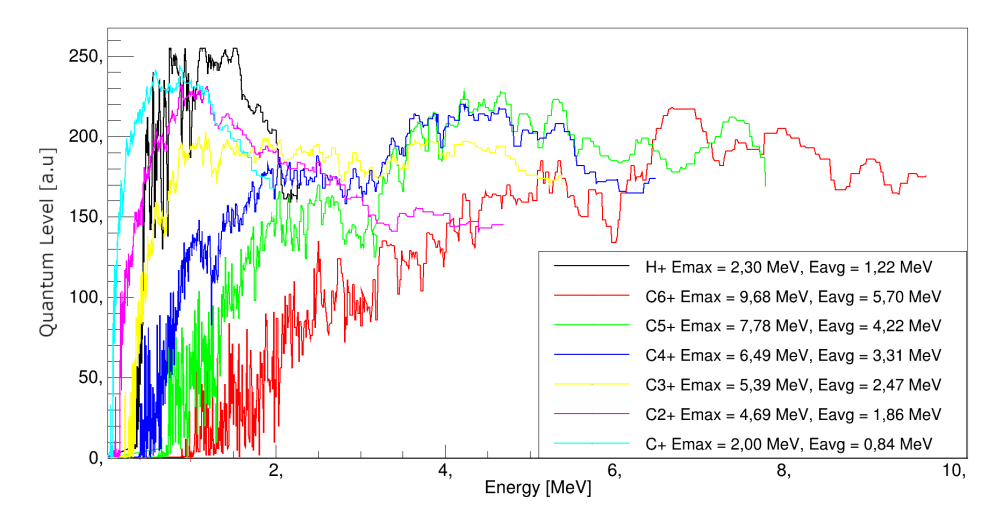


FIGURE 2.13: Energy spectrum of parabolas from Fig. 2.12 (left) in units of quantum-level.

The computed parabolic shape is then fitted to experimental data by using an iterative method applied by the user, changing the range of energies that define the start and end point of the track in the way that it is perfectly aligned with image registered during the experiment (example of such fitting is displayed on Fig. 2.12). Afterwards, the intensities of the pixels overlapping with the parabola points are extracted from the image and coupled with given E (Fig 2.13), resulting (after applying calibration curves for given detector of choice) in  $N_i(E)$ .

#### 2.2.2 Data analysis software

It is worth noting that the described software is not bound to specific TPS unit – introduced parametrization of geometry allows to reconstruct any spectrometer chamber (Figure 2.15), therefore it can be coupled with different TPS designs and used by other groups according to their needs when official released.

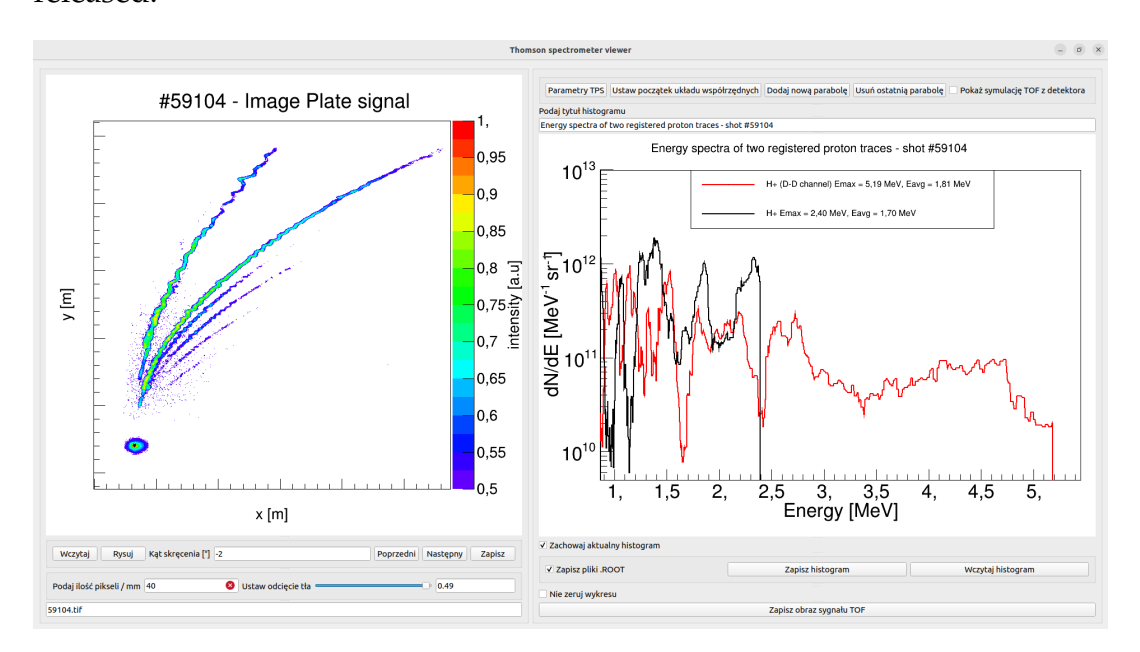


FIGURE 2.14: Snapshot of TPS results analysis process using TPSeer software.

Although still in development, recently a Graphical User Interface was implemented in order to both improve and facilitate the efficiency of analysis process without the need of programming knowledge. "TPSeer" was written in C/C++ using the ROOT framework [54], which is associated with CERN facility and used for various applications related to high energy-density physics and nuclear physics, while the GUI is provided by Qt package (Fig 2.14).

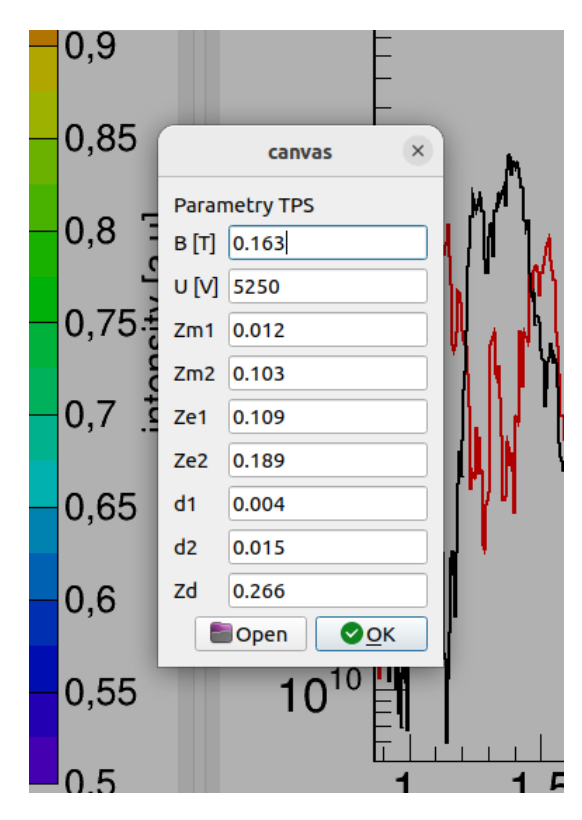


FIGURE 2.15: Snapshot of "TPSeer" geometry definition of spectrometer.

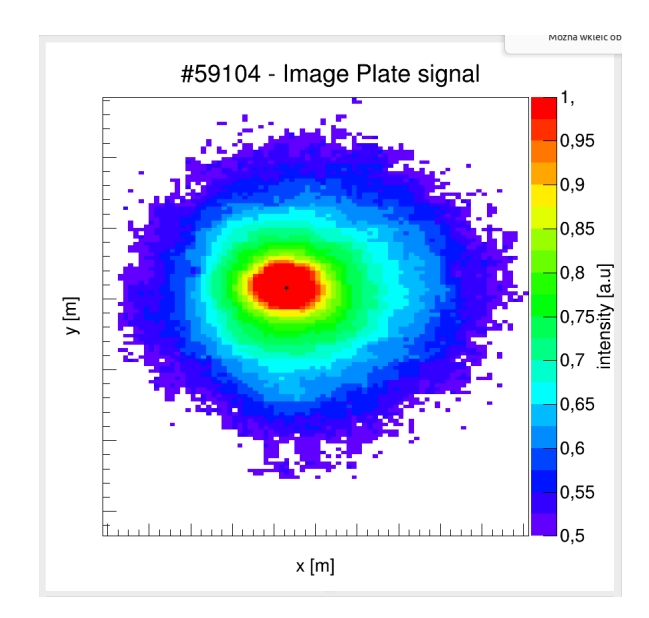


FIGURE 2.16: Positioning of origin of calculated fitting parabolas

The supported file type for input image are any of the most common file types, such as JPEG, .BMP, .PNG, .TIF. After choosing designated source file and obtaining the initial image, user has to provide parameters required to

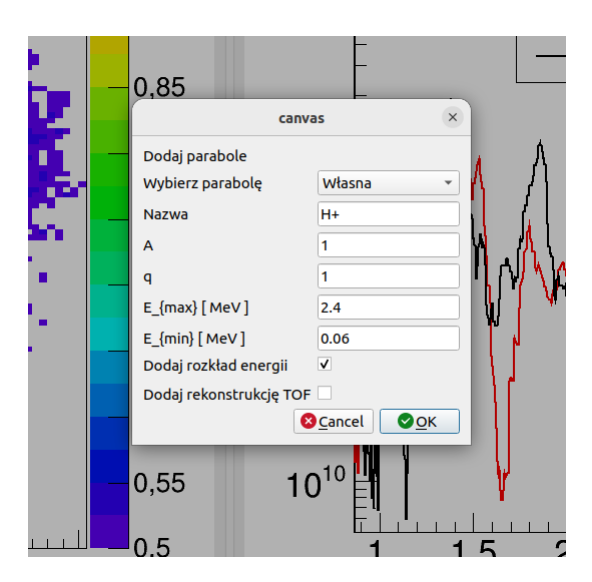


FIGURE 2.17: Snapshot of "TPSeer" module responsible for defining the theoretical parabola.

created chamber geometry (Fig 2.15) and so-called zero point, which corresponds to center of pinhole where particles of neutral charge and electromagnetic radiation is visible (Fig. 2.16).

In case of high repetition rate experiments, common choice of the detector is multichannel plate coupled with phosphor screen coupled with fast camera, therefore the position of zero point does not change during the spectrometer operation. However, when Image Plates are used, the position of mentioned reference point is constantly changing due to frequent replacing of the detector. Therefore, the software utilizes point-and-click mechanism for initialization of zero point and afterwards allows to drag-and-drop the marker to different position when needed. Moreover, repetitive procedure of replacing the detector between the shots often leads to angular displacement of the Image Plate inside the chamber. To address this issue, the software is equipped with possibility to easily rotate the coordinate system by providing user defined value of mentioned rotation angle.

The next step in analysis process is defining specific theoretical parabolic trace, which then has to be fitted to experimental data. A collection of most commonly sought after ion kinds is predefined and available to pick from drop-down list, however the user can request to draw particular ion trace of given mass number A and charge q (Fig. 2.17). The last two parameters that have to be provided are  $E_{max}$  and  $E_{min}$ , which are defining the beginning and the end of a trace to be drawn. Multiple parabolas of different ion parameters can be fitted simultaneously which allows to complex analysis of the experimental results such as identification of accelerated ion kinds (Fig. 2.18) and

retreiving their energy spectra (Fig. 2.13) by applying equations and methods described in Section 2.2.1. By default, two parameters are explicitly given during creation of the energy spectrum graph - the maximum, cut-off energy  $E_{max}$  and the average energy  $E_{avg}$ . The latter represents the mean energy extracted from the drawn parabola. If the entire range of protons are captured on the detector, this value corresponds to average ion energy, however if the low energy part of proton beam is deflected outside of the detection plane, this value will correspond only to the captured part.

Additional feature of TPSeer software is ability to set so called intensity threshold, allowing user to tune visible range of pixel intensities. This functionality is especially useful during analysis of data where high background noise and high number of parabolas is expected. By adjusting this parameter, pixels of intensity lower than specified are not shown, which allows to overlap computed traces with experimental data more precisely.

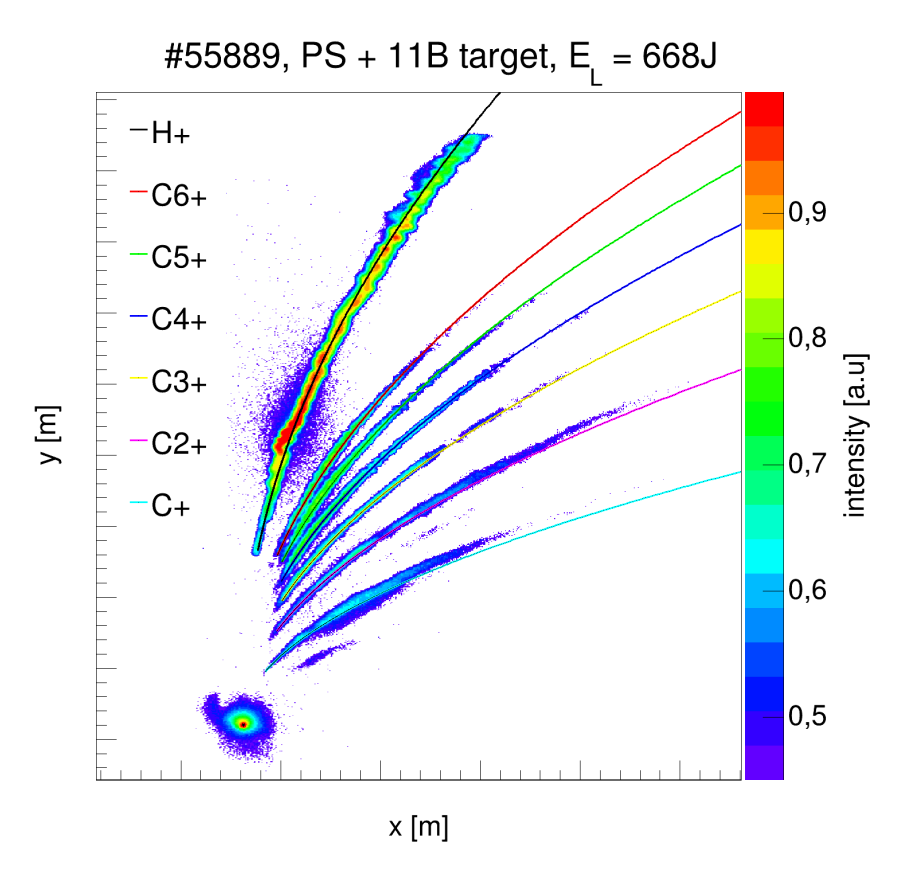


FIGURE 2.18: Result of fitting theoretical ion lines to experimental results.

Graphs and images created while working with the software can be saved as both image files and .ROOT files, allowing the user to access previously saved data such as energy spectrum and load the data with a single button,

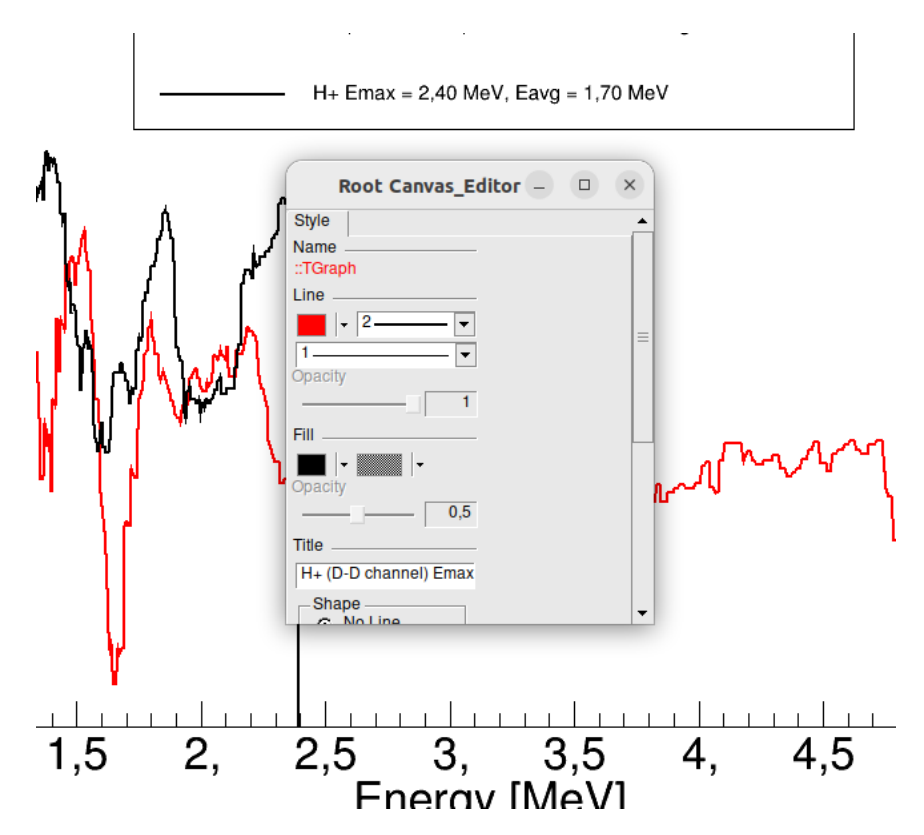


FIGURE 2.19: Snapshot of "TPSeer" graphic edition module window.

simplifying the process of data comparison between different experiments. Another functionality of the software is built-in graphical editor available for any drawn objects which allows to customize produced graphs (label sizes, axis ranges, line colors, etc.), which basic window is presented on Figure 2.19.

Although TPSeer was originally written in order to process the experimental data that is the subject of this thesis, it was successfully used to analyze the TPS data from multiple different experiments [55, 56].

The development process of this software is still not finished. Implementation of calibration curves for ion species different than protons is currently under development, as well as further visual optimization of the interface, RAM/CPU management and portability of software (until then recommended operating system to run the TPSeer is Linux).

#### 2.3 Monte Carlo FLUKA simulations

The Monte Carlo (MC) approach is a numerical integration model very often used in solving complex, statistical physics problems. The main idea of MC method is to randomly sample the events according to given theoretical probability distribution. Due to the nature of nuclear reactions and particle transport, whose in principal are dependent on cross sections (interaction probabilities per unit distance) of particular events, MC method is widely used when estimation of particle-matter (or radiation-matter) results is of interest. In this work, the code of choice to examine the output of given proton beam interaction with boron catchers was the FLUKA code [45, 57].

FLUKA is fully integrated particle physics Monte Carlo simulation package widely used by researchers in different fields, starting from radiation shielding to dosimetry, target and detector design, radiotherapy, acceleration and particle physics etc. Since the development of this code, FLUKA has been constantly updated with modern physical models and up to date experimental databases such as ENDF/B, JEFF, JENDL. Physical models implemented in FLUKA cover broad range of potential phenomena, such as hadron inelastic nuclear interactions, elastic scattering, nucleus-nucleus interactions, transport of charged hadrons and muons, energy loss calculations, as well as electrons, photons and neutrinos physics for energies up to thousands of TeV. Important feature of this tool is handling complex geometries by employing improved version of Combinatorial Geometry package, which is able to track charged particles (with or without presence of magnetic field). Lastly, majority of the proton-boron work published in journals utilize FLUKA to verify experimental data, therefore performing calculations using this code is natural choice when comparing the obtained results with outcome of different groups.

It is worth noting that currently two, concurrent versions of FLUKA are available – one distributed by CERN (Switzerland) and one distributed by INFN (Italy). Historically, both institutions were jointly developing one code, however in 2019 the collaboration was terminated and lead to separate versions of FLUKA. In this work, the INFN distribution of the code is used. One of the reasons is that this version is (and was) used by leading groups working in proton-boron field of research – until just few months before completion of this dissertation, the CERN branch was not covering the energy range of cross section in which probability of  $p + {}^{11}B$  reaction to happen was the highest (675 keV CoM). Therefore the MC calculations presented in this work

are ensured to follow the same physical models as the results which they will be compared to.

## 2.3.1 Interaction of proton beam with boron catcher: geometry design and scoring estimators in FLAIR

The geometry of FLUKA simulations was prepared with the help of FLAIR add-on [58], which is usually bundled with FLUKA distributions. This advanced editor of FLUKA input files allows not only to design the geometry of experiment easily due to drag-and-drop mechanism, but also to manage the virtual detectors, edit input files and prepare plots of scored quantities. The example of FLUKA input created in FLAIR and geometry tab is shown on Figure 2.20 and Figure 2.21.

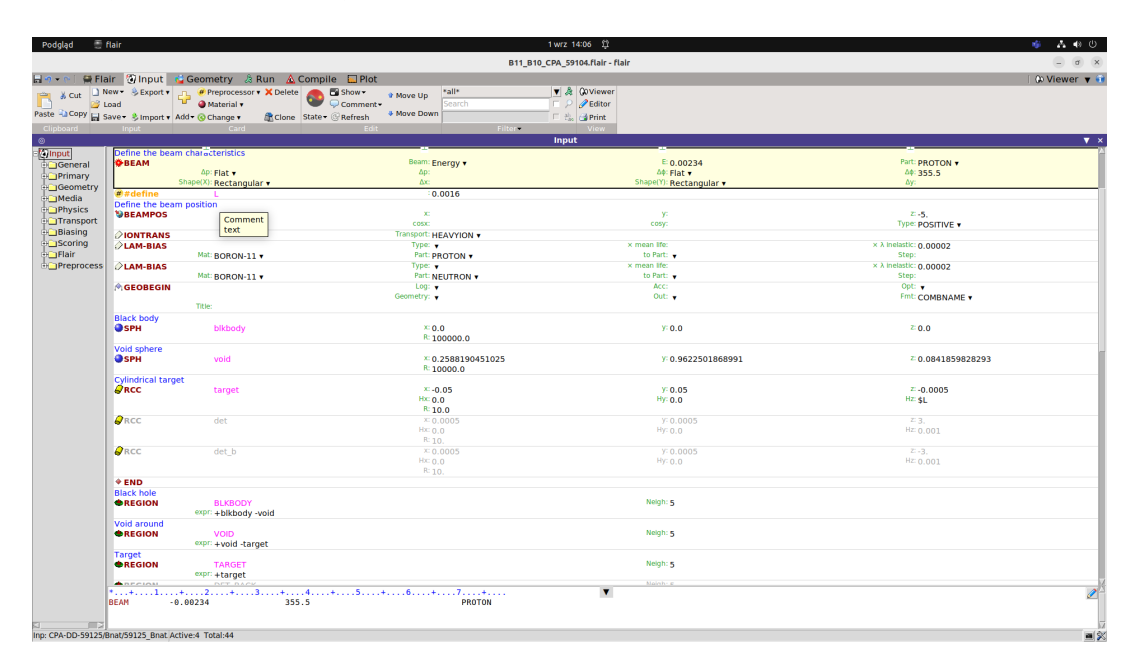


FIGURE 2.20: Snapshot of FLAIR software main window.

The cylindrical boron catcher of R=10cm and thickness (height) varying from  $d=5 \mu m-180 \mu m$ , was placed in the center of void sphere, cocentric with a sphere filled with so-called "black-body" which serve a purpose of beam-dump for any particles exiting the geometry borders. The catcher was placed 5cm away from the proton source of angular divergence set to  $20^{\circ}$  (Figure 2.22).

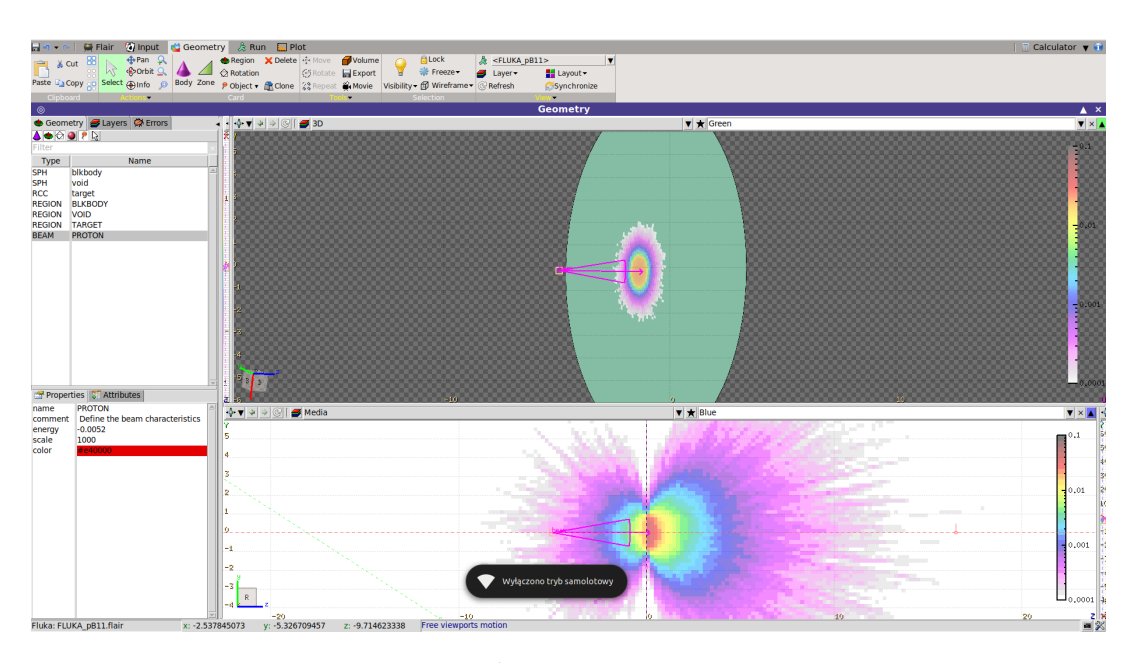


FIGURE 2.21: Snapshot of geometry designer module - proton beam (purple cone) irradiating boron disk target (top) and overlayed USRBIN scoring over one of the geometry ports (bottom).

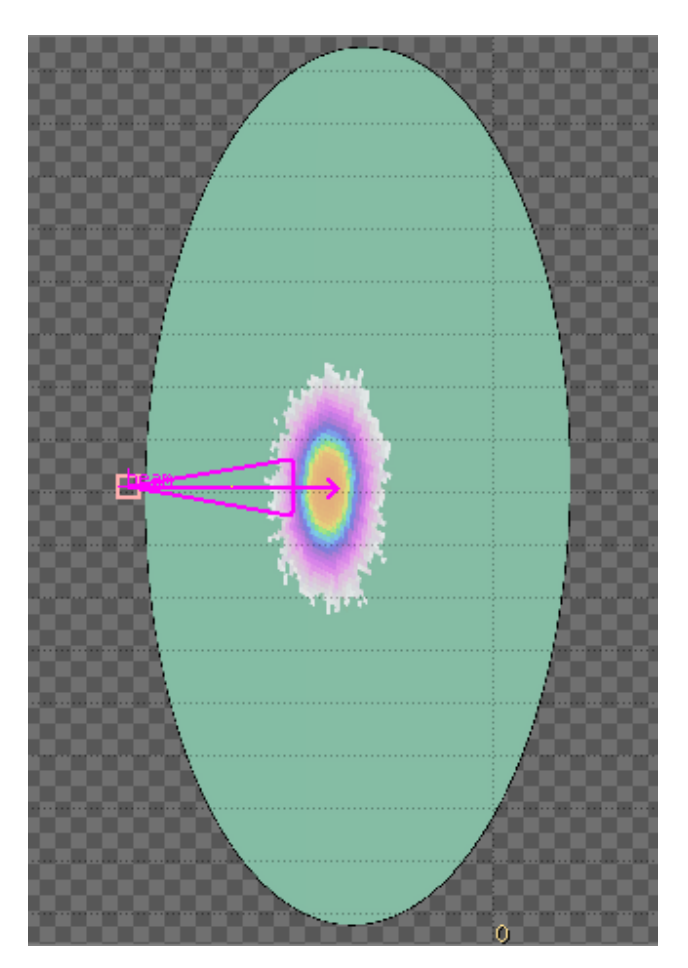


FIGURE 2.22: Enlarged simulation geometry design with overlayed alpha particle fluence on the targets front surface.

The proton spectra that were used in the simulations were extracted from experimental data obtained with Thomson Parabola Spectrometer, described in 2.2.1. The spectrum consisted of 1000 samples, with yield relative to maximum of the measured intensity. The quantities scored with FLUKA simulations are by defult given in units "per primary" (in this case, per proton), allowing to adjust the result to actual number of particles to total number of protons measured experimentally. This allowed to compare spectra obtained during different experiments, which utilized different detectors coupled with TPS. Example of proton energy spectra (intensity in arbitrary units) used in simulations is displayed on Figure 2.23.

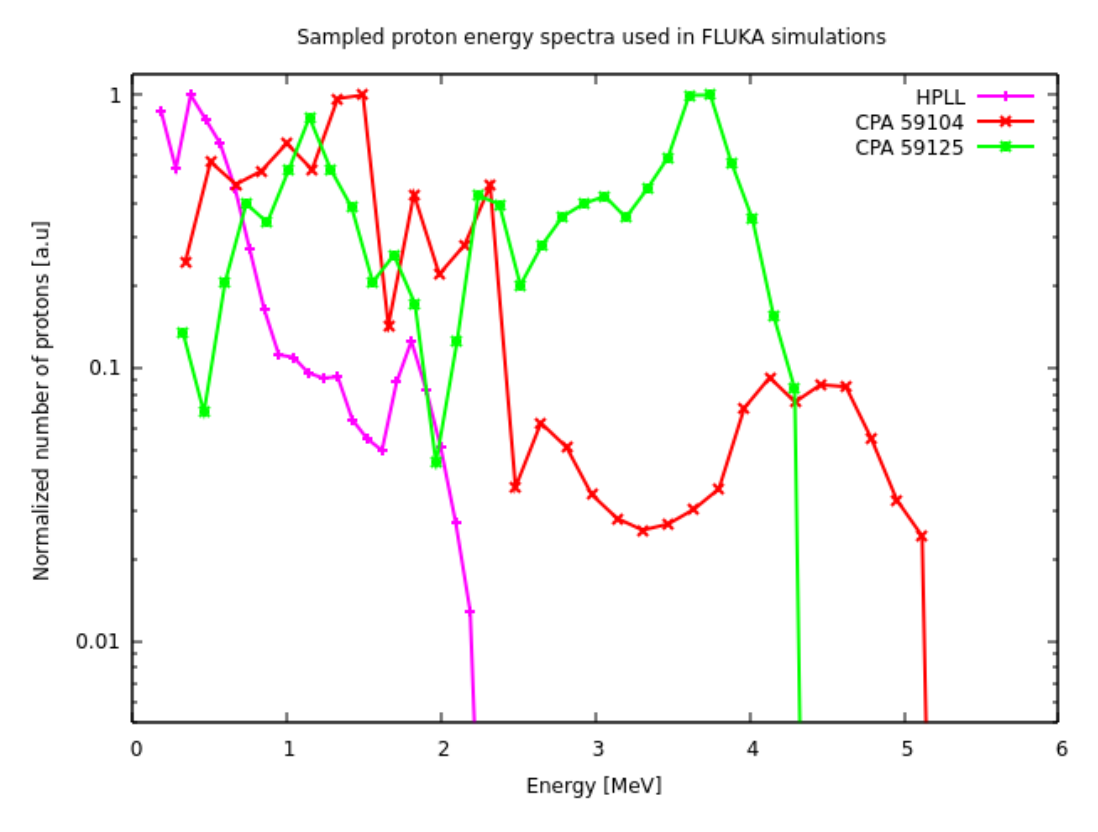


FIGURE 2.23: Experimental energy spectra of proton beams sampled by FLUKA.

Since the main goal of simulations was to estimate total yield of alpha particles exiting the boron catcher, instead of placing virtual detector in specific postion (which is often the case when performing MC simulations to recreate particular experimental conditions), in presented data alpha particles and neutrons energy spectra were scored during crossing the target surface and entering void sphere. This approach eliminated fraction of alpha particles that were produced but did not leave the volume of the target due to stopping processes. The most suitable built-in scoring technique available

for such design was USRBDX boundary-crossing estimator, capable of providing information on either fluence or current, with results given as double differential distributions in energy and solid angle.

Another scoring estimator that was employed in presented results was USRBIN, which brings information about fluence across regular spatial structure (mesh). This tool was used when angular density distribution of produced particles was of interest (Fig 2.24, 3.7, 3.31), allowing to observe the ratio of alpha particles emitted from the boron catcher in forward and backward direction.

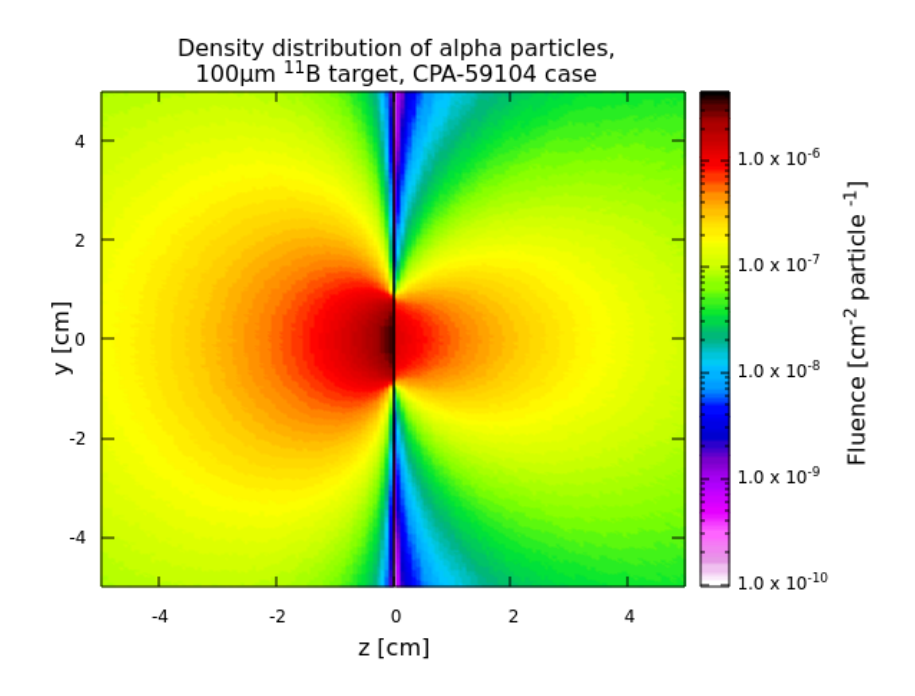


FIGURE 2.24: 2D distribution of alpha particles fluence in FLUKA simulation box.

The fluence calculated by FLUKA scorings is expressed in units of track length density of particle trajectories in given bin volume. Considering the volume generated by the surface S of infinitesimal thickness dt and the particle which is incident to the surface with an angle  $\Theta$  and traveling a segment  $\frac{dt}{\cos\Theta}$  inside the given volume, one can define the average fluence F over the surface S as:

$$\Phi = \lim_{dt \to 0} \frac{\sum_{i} \frac{dt}{\cos\Theta_{i}}}{Sdt}$$
 (2.5)

Since the path length is by default expressed in centimeters and the volume of the bin in cubic centimeters, therefore the basic unit of fluence scored by FLUKA is expressed as  $\frac{1}{cm^2}$  per primary (in this case, per incident proton).

This parameter is used in this work when spatial 2D distribution of alpha particles, obtained with USRBIN estimator, is presented .

Energy spectra of particles shown in this work, obtained with USRBDX estimator, are obtained by scoring average current *J*, which is given by the number of particles *N* crossing the surface of detection area *S*:

$$J = \frac{N}{S} \tag{2.6}$$

By default, contrary to fluence, current is dependent on the orientation of the surface along which it is scored. When flat surface is considered in an isotropic particle field (which is the case in this work), the relation  $J = \frac{\Theta}{2}$  is applicable.

At the time of writing this dissertation, FLUKA code does not cover the interaction of particles with plasma, therefore the secondary target is considered to be "cold", in solid state.

## 3 Results and discussion

In order to assess the capabilities of Cavity Pressure Acceleration mechanism in driving proton-boron reaction using TW-class lasers, the comparison between features of proton beams in both standard TNSA approach (Section 3.1.1) and deuterium-deuterium based CPA approach (Section 3.2.1) will be done.

The results related to the TNSA approach were obtained using Pulsar 10 TW laser system which is available at High Power Laser Laboratory in Institute of Plasma Physics and Laser Microfusion (Warsaw, Poland). This particular laser system generates femtosecond-long laser pulses following the Chirp Pulse Amplification technique. This type of laser system is commonly used in laser ion acceleration experiments since the intensity of generated pulses allow to perform TNSA-based acceleration with moderate repetition rate, which in this case is equal to maximum 10 Hz.

The data related to CPA mechanism were obtained during external experiment performed at Prague Asterix Laser System located in Prague, Czech Republic which is able to generate laser pulses of power approaching 2 TW.

For each case, obtained proton beam serves as an input to a set of Monte Carlo simulations in which the applied proton beam interacts with secondary target made of either pure boron-11 or natural boron (Sections 3.1.2 and 3.2.3). Based on the output of the simulations, the capabilities of both approaches in terms of alpha particles production during  $p + {}^{11}B$  reaction will be addressed.

In both cases, the proton beam characterization is solely based on the results obtained with Thomson Parabola Spectrometer designed and operated by IPPLM team (Section 2.2.1).

## 3.1 Experimental and MC simulations results: High Power Laser Laboratory (HPLL) (Warsaw, Poland)

#### 3.1.1 Experimental results

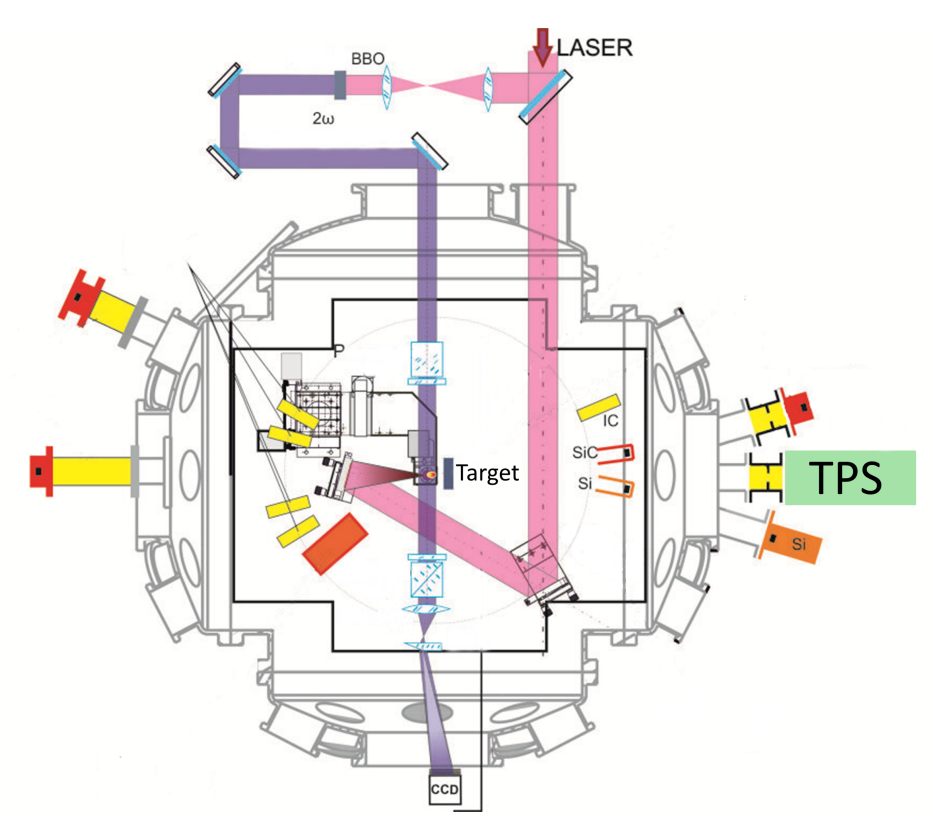


FIGURE 3.1: Schematic drawing of HPLL experimental chamber with standard positions of diagnostic devices.

The experimental chamber routinely used in High Power Laser Laboratory of Institute of Plasma Physics and Laser Microfusion is displayed on Figure 3.1. Depending on the choice of laser parameters, such as the size of focal spot, pulse duration and the pulse energy on target, as well as properties of the target (thickness, chemical composition etc.) it is possible to achieve up to 4 MeV maximum energy of accelerated protons using our laser system when irradiating thin, foil targets. By default, the accessible laser intensity using our laser system is on the level of  $I_L \approx 10^{18} - 10^{19} \frac{W}{cm^2}$ , allowing to perform TNSA ion acceleration. The energy on target, after compression and transmission from compressor chamber to experimental chamber is on the level of  $E_L = 300 \, mJ$ , the pulse duration  $\tau = 45 \, fs$ , with focal spot diameter  $d = 30 \, \mu m$ .

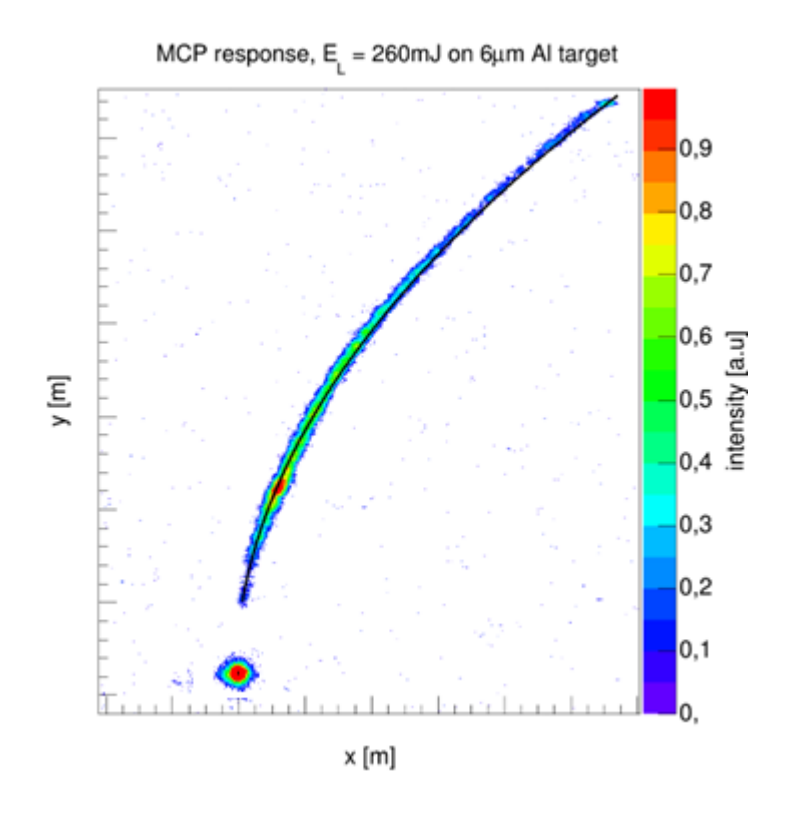


FIGURE 3.2: Parabola of protons captured by Multi-Channel Plate coupled with Thomson Parabola Spectrometer. The image is processed by "TPSeer" software and theoretical proton parabola is fitted (black line).

During recent high repetition rate experiments, one of the goals was to obtain as stable (in terms of maximum and average energy) proton beam as possible – therefore multiple combinations of parameters of the laser-matter interaction were examined. Focusing the laser pulse on Al or CH foils of different thickness (the tests covered  $1.5 \, \mu m - 8 \, \mu m$  range) and adjusting focal spot position in respect to the target front surface (along the propagation axis) revealed that the optimal setup for  $1 \, Hz$  repetition rate of laser-matter interaction (in terms of proton beam stability) was Al target of thickness  $d = 6 \, \mu m$ , focal position  $+150 \, \mu m$  inside the target at pulse energy  $E_L = 260 \, mJ$ .

In result, an example of the typical reproducible characteristics of the proton beam obtained with TPS are displayed on Figure 3.2, 3.3.

At the cost of lowering maximum proton energies (which are accessible at lower target thickness and higher energy of the laser pulse) to  $E_{p^+max} = 2.4 \, MeV$  we were able to maintain the shape of energy spectrum with visible peak around 500keV in multiple consecutive shots (Fig. 3.3, averaged over 6 shots). In these TPS measurements we used multi-channel plate

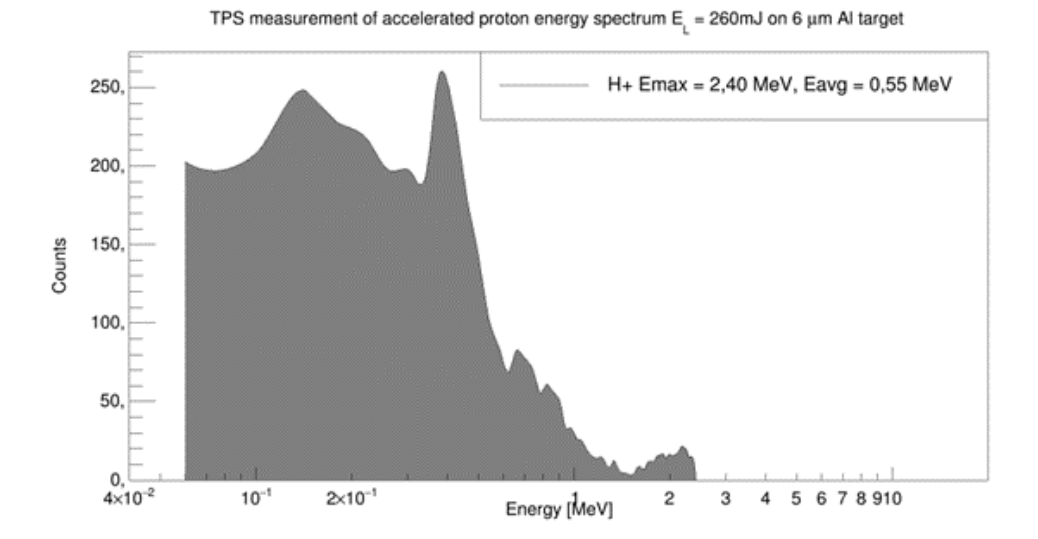


FIGURE 3.3: Energy spectrum of protons captured on Fig. 3.2.

coupled with phosphor screen to register ion traces. This detection system is yet to be calibrated, therefore the number of particles at particular energy is given in arbitrary units.

Measured energy spectrum of accelerated protons exhibits properties suitable for performing studies on  $p+{}^{11}B\to 3\alpha$  reaction. To confirm possibility of exploring this phenomena in our laboratory and provide more information about optimal setup of potential proton-boron experiments, a series of Monte Carlo simulations were performed. The tool which was used to examine the outcome of such interaction in this case was FLUKA package distributed by INFN (Italy), which was described in Section 2.3 .

# 3.1.2 FLUKA simulations for HPLL case of proton beam energy spectrum

Following the simulation setup described in 2.3.1, the possibility of producing alpha particles using proton beams accessible in High Power Laser Laboratory at IPPLM was examined. Two target compositions were tested - pure  $^{11}B$  and natural boron (80% of  $^{11}B$  and 20% of  $^{10}B$ ). The energy spectra of produced alpha particles were obtained through scoring particles crossing the bonduary between the region of target and void with USRBDX estimator and are presented on Fig. 3.4 and Fig. 3.5.

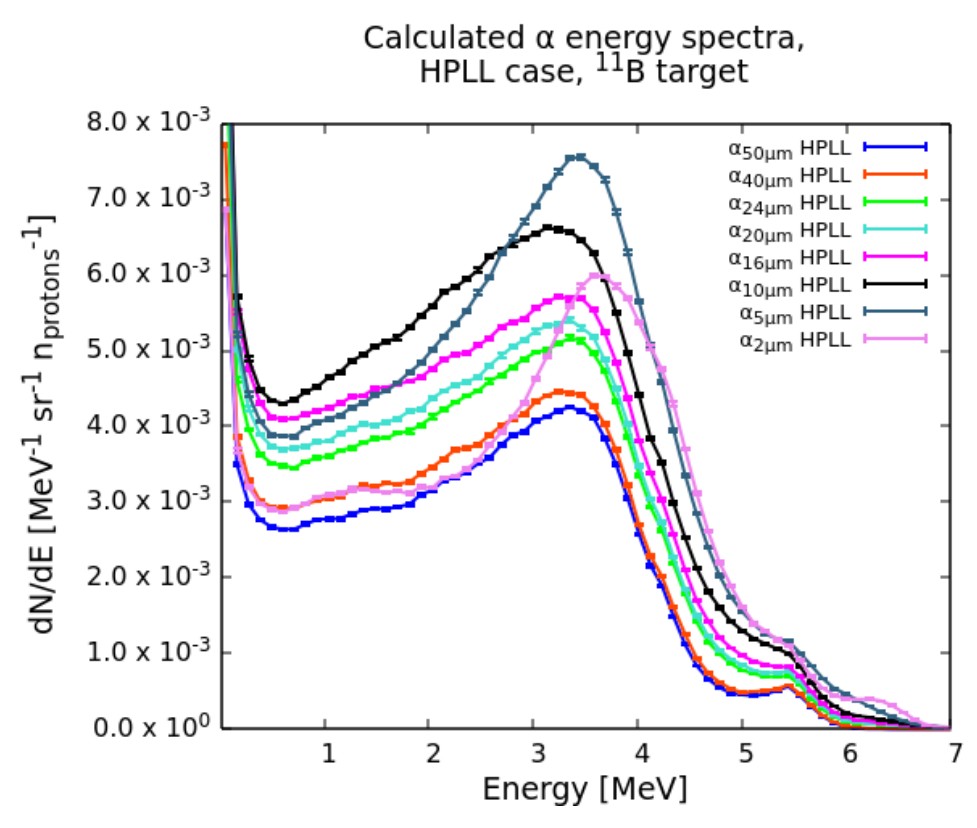


FIGURE 3.4: Alpha particle energy spectrum for different thickness of pure boron-11 catcher - calculated in FLUKA using energy spectrum obtained in HPLL.

As the target thickness increase and therefore the amount of released alpha particles is decreased, two distinct peaks are becoming more visible sharp peak at 5.5 MeV and broad peak centered around 3.5 - 4 MeV. These structures are representing primary alpha particles generated in one of two possible reaction channels of  $^{12}C^* \rightarrow \alpha_{primary} + ^8Be^{(*)}$  break-up process described by Laursen et al. [59]. If  $^8Be$  is in ground state, the energy of primary

alpha particle ( $\alpha_0$ ) is equal to  $\sim 6 \, MeV$ , whereas the first excited state of  $^8Be$  ( $\alpha_1$ ) results with broad peak in the energy spectrum around 4 MeV.

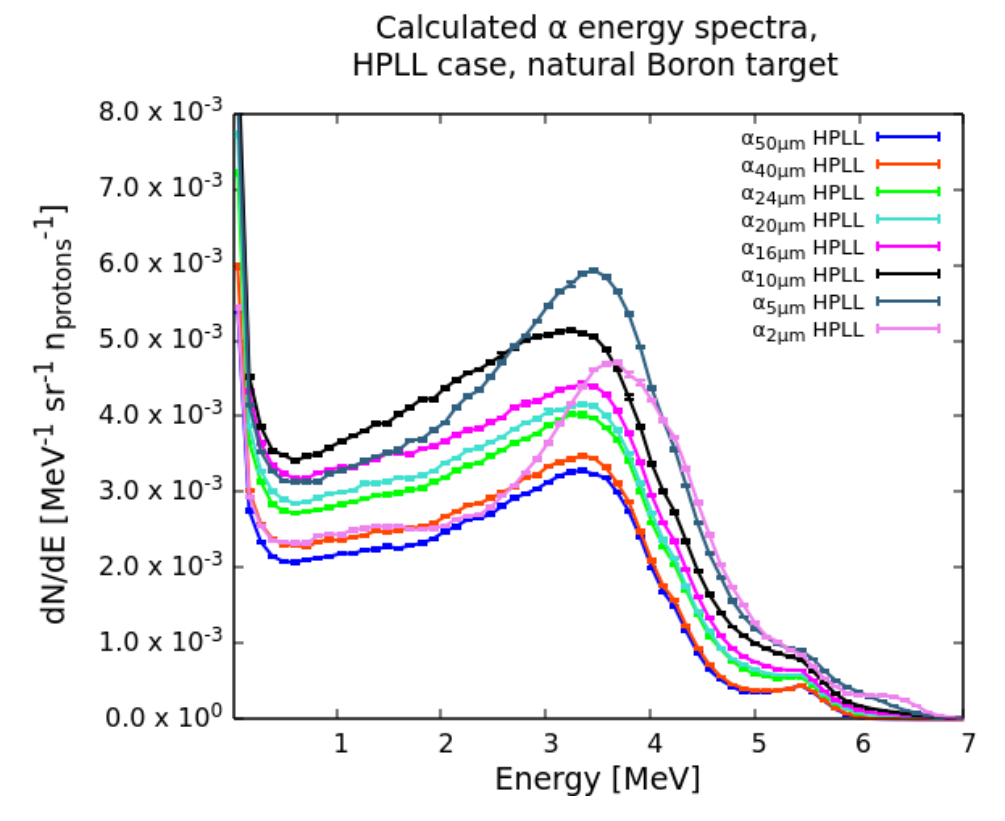
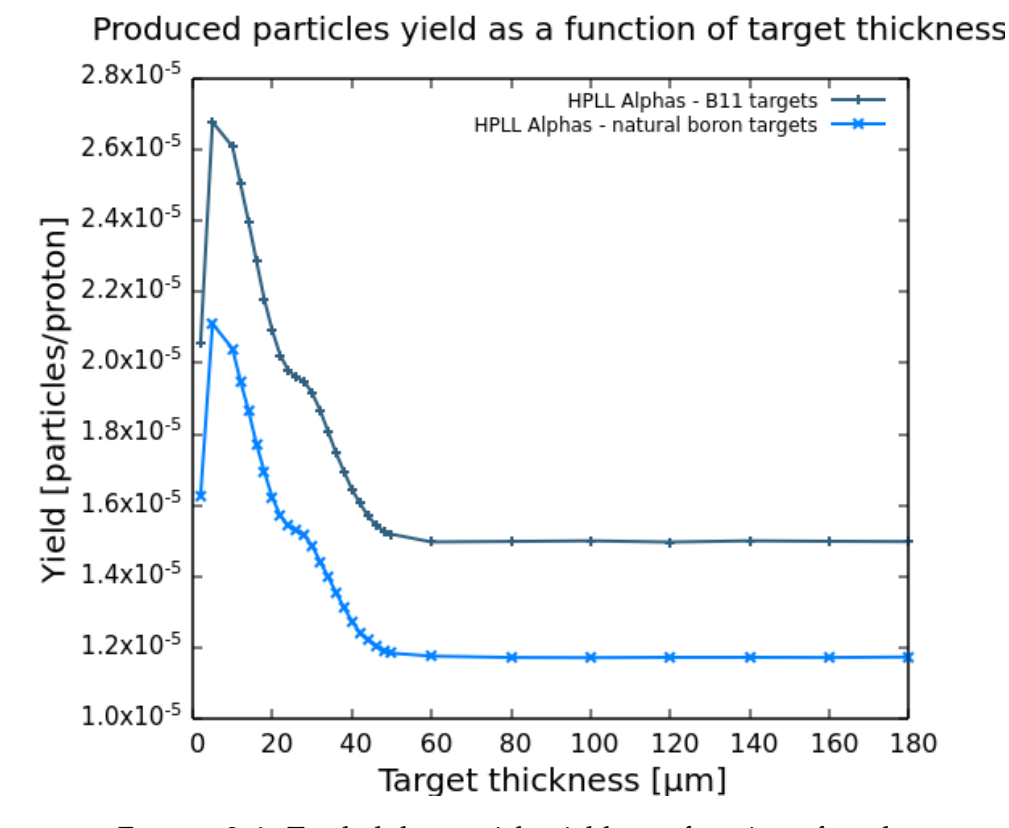


FIGURE 3.5: Alpha particle energy spectrum for different thickness of natural boron catcher - calculated in FLUKA using energy spectrum obtained in HPLL.

Set of simulations was performed to identify the most optimal target thickness for pitcher-catcher scheme of proton-boron experiment (Fig. 3.6). Using targets thicker than 5  $\mu m$  one can observe rapid decrease of produced  $^4_2He$  yield, and for thickness exceeding 60  $\mu m$  number of alpha particles remains constant. This occurs due to alpha particles being stopped inside the target and not being able to penetrate remaining volume of the secondary boron target, preventing them from leaving the rear side of the catcher (Fig. 3.7). This brings valuable information about the number of alpha particles being produced on surface of the interaction side of the catcher, equal to  $1.51 \times 10^{-5} \frac{\alpha}{p^+}$  for boron-11 and  $1.17 \times 10^{-5} \frac{\alpha}{p^+}$  for natural boron targets. The difference in the amount of produced alpha particles for these two types of targets is equal to 20%, which reflect the difference of boron-11 content in the target volume between two considered materials. The inflection point visible near the 30  $\mu m$  thick targets (Fig 3.6) might correspond to a meaningful fraction of protons achieving energy equal to the favoured value for reaching



## FIGURE 3.6: Total alpha particle yield as a function of catcher thickness.

secondary resonance of the cross-section ( $\sim$  150 keV CoM) at the rear side of the catcher, which was recently explored in the work of Istokskaia et al. [60].

Another important result of FLUKA simulations is no clear evidence of neutrons produced during interaction of such proton beam with the boron catcher (Fig. 3.8, 3.9). The importance of this observation is that despite the fact that proton – boron fusion is often referred to as aneutronic, in majority of experiments generation of neutrons is reported [43, 61]. This is due to the secondary reactions taking place inside the boron target such as  $^{11}B(p,n)^{11}C$  or  $^{11}B(p,n)^{14}N$  (which leads to another reaction:  $^{14}N(\alpha,n)^{17}F$  [61]. However, the accessible energies of protons in this particular case are below the energies required to induce these reactions, therefore the proton-boron fusion in this very case seems to be in fact neutron-less, brilliant source of alpha particles that could be used in medical or material science related applications.

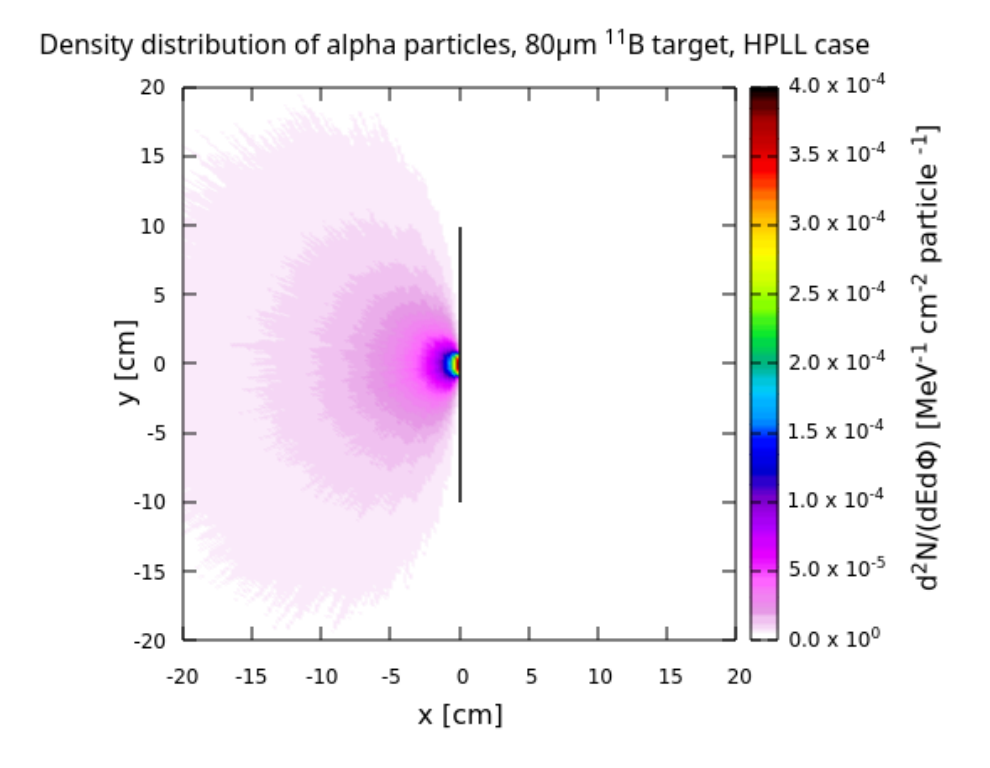


FIGURE 3.7: 2D alpha particle distribution for  $80 \mu m$  boron-11 catcher. Alpha particles are mainly emitted in backward direction.

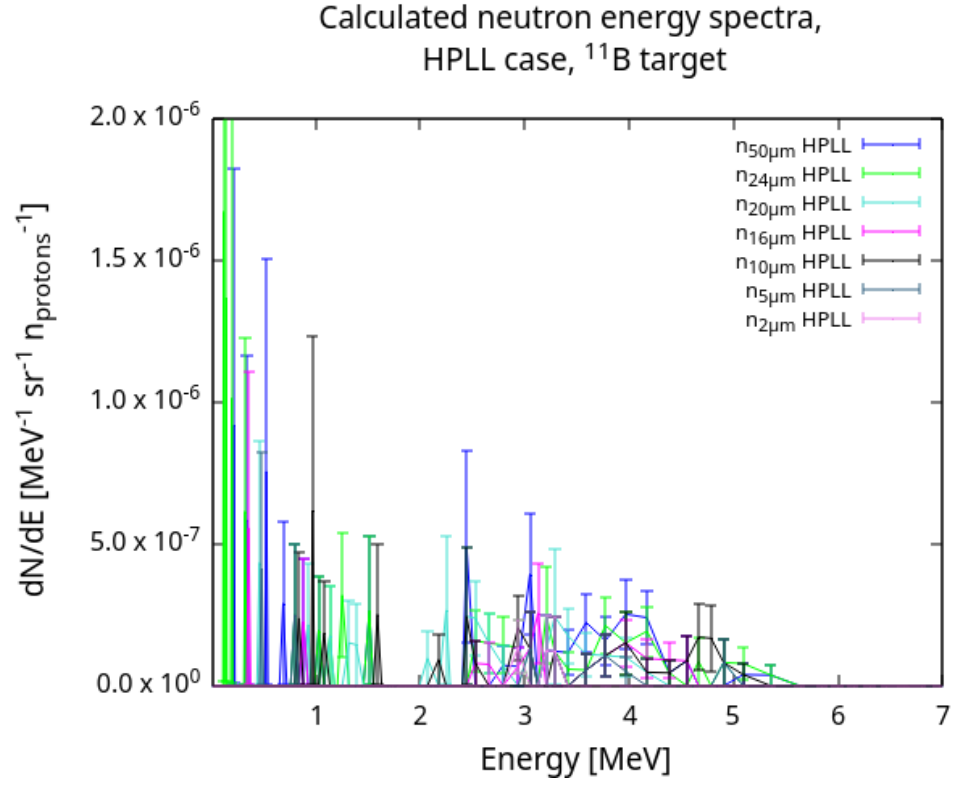
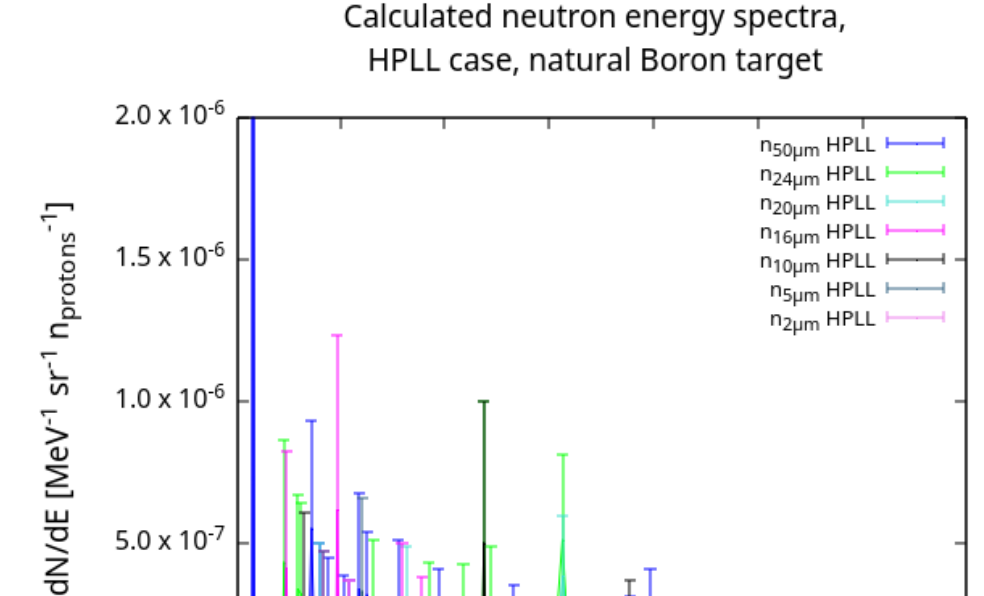


FIGURE 3.8: Neutron energy spectrum for different thickness of pure boron-11 catcher - calculated in FLUKA using energy spectrum obtained in HPLL.



5.0 x 10<sup>-7</sup>

 $0.0 \times 10^{0}$ 

1

FIGURE 3.9: Neutron energy spectrum for different thickness of natural boron catcher - calculated in FLUKA using energy spectrum obtained in HPLL.

3

Energy [MeV]

5

6

7

2

# 3.2 Experimental and MC simulations results: Cavity Pressure Acceleration campaign at PALS (Prague, Czech Republic)

In search of improving the efficiency of this fusion approach, numerous experimental groups are investigating so-called "in-target" scenario, where generation of protons and alpha particles is taking place in the volume of single target. This scenario requires sophisticated and tailored multi-element targets, often multi-layered and precisely designed with techniques which incorporate ion implantation and chemical vapour deposition, which are not internally accessible to our group at the moment and require external collaborations to be performed [44, 62]. Another approach focuses on tuning acceleration process itself, enhancing the primary proton beam with precisely designing the initial laser-matter interaction in the pitcher-catcher scenario, or even reversing the pattern and accelerating boron ions to irradiate hydrogenrich secondary target [63].

During our recent experiments related to macroparticle acceleration, which has been proposed as an alternative approach to fast ignition scheme of inertial confinement fusion (and simultaneously investigated since 2000s by two groups of our division), our group obtained promising results which have shown possibility of producing, characterizing and utilizing intense beams of multi-MeV protons originated in thermonuclear deuterium-deuterium reaction by means of Cavity Pressure Acceleration (CPA) scheme. The crucial parameters of this particle beam are superior to previously shown results (in terms of intensity, shape of the energetic spectrum and both average and maximum energy) obtained by means of TNSA approach to laser acceleration using 10TW laser system available in IPPLM, therefore applying them in proton-boron reaction is heavily considered and will be discussed below.

## 3.2.1 Experimental results

In November 2022 the latest experiment regarding CPA was performed at PALS laboratory in Czech Republic [64]. The goal of the experiment was not only to verify and replicate previous results, further enhancing production of neutrons by means of D + D reaction, but also investigate different designs of CPA targets, displayed in Figure 3.10.

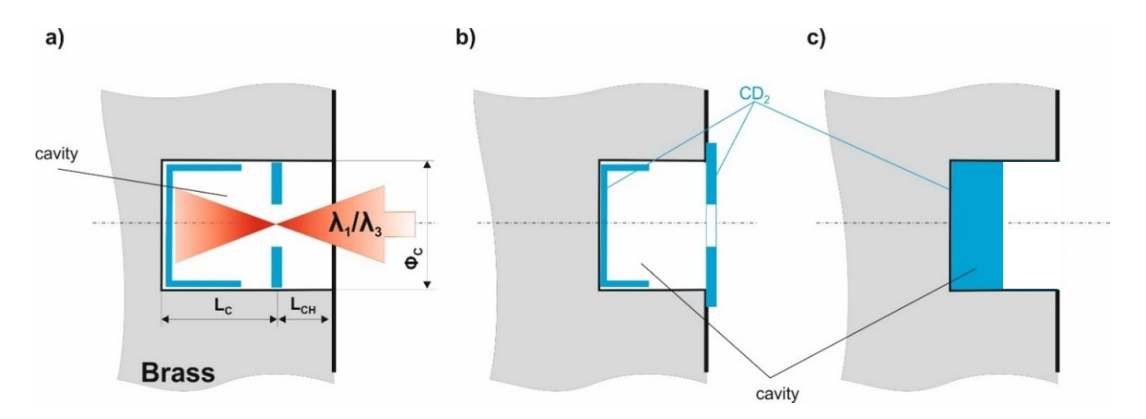


FIGURE 3.10: Three variants of cavity targets - cavity target with the channel (a), cavity target without the channel (b) and cavity filled with  $CD_2$  powder (c).

The first design, presented on Fig. 3.10(a), was the copy of the targets used in previous experimental campaign serving a role of a reference to verify identical laser characteristics as in previous session. In second type of targets, Fig. 3.10(b), the channel was removed. Lastly, the target with cavity filled partially with  $CD_2$  powder was used 3.10(c). This particular type of targets was proposed to verify whether the neutron production occurs following the *beam-target* mechanism [65, 66] or rather due to thermonuclear reaction criteria being met during compression of the deuterium plasma inside the cavity, which was suggested by hydrodynamic simulations.

The laser pulse parameters used in this experimental session were as follows: laser pulse energy in the range 500 - 700 J, pulse duration  $\tau = 300 ps$  and laser wavelength  $\lambda_L = 1315 \, nm \, (1\omega)$ . The key diagnostics used during experiment were: BD-PND type neutron dosimeters (bubble detectors), scintillator-based neutron time-of-flight probes, ion collectors, TPS and 3-frame interferometric system. The simple schematic of experimental chamber is shown on Fig. 3.11.

One of the most prominent results obtained during recent two, consecutive CPA experiments was identification of double-parabolic formation of protons by means of Thomson spectrometer, visible in number of shots

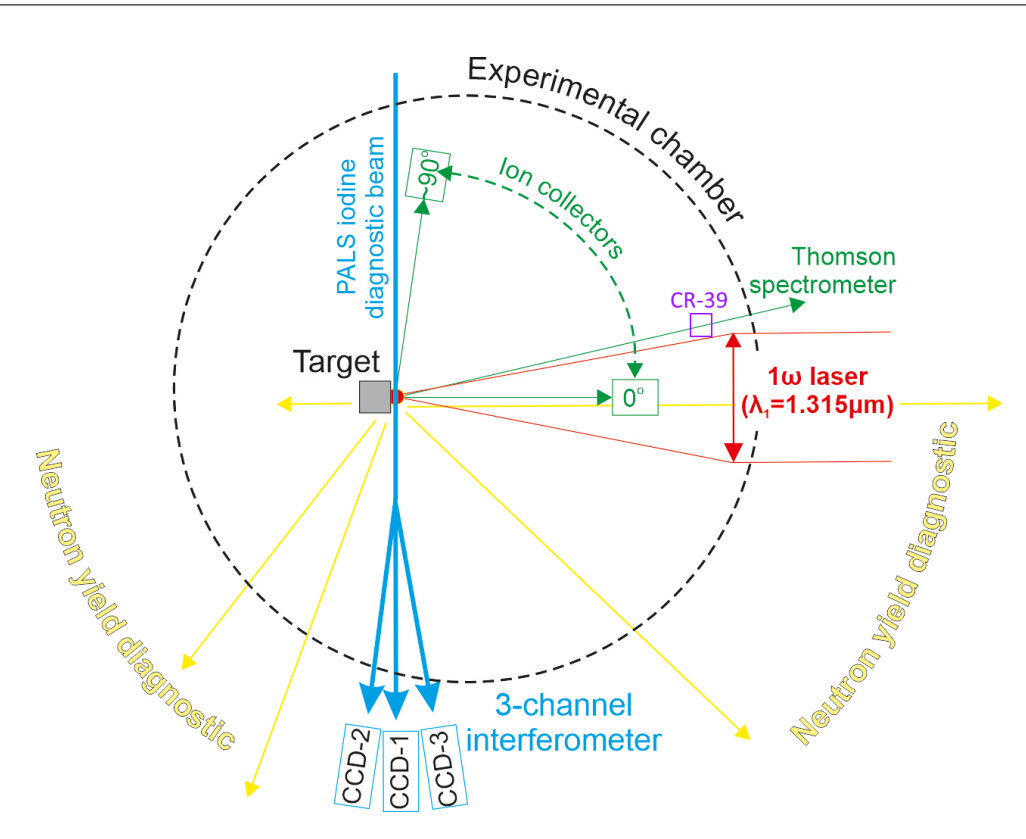


FIGURE 3.11: Schematic of experimental chamber and positions of important plasma diagnostics during described experimental campaign.

(Fig. 3.12). Questionable at first, after investigating results provided by neutron detectors during recent experimental session, it was confirmed that this pattern appeared in shots with extremely high number of registered neutrons. The explanation of this finding lies in the two channels of deuterium-deuterium reaction:

$$D + D \to T + p (3.02 MeV)$$
 (50%)  
 $D + D \to {}^{3}_{2} He + n (2.45 MeV)$  (50%)

Having the same probability of producing either tritium and proton or  ${}_{2}^{3}He$  and neutron, one should expect presence of DD-produced protons in vicinity of thermonuclear deuterium fusion.

In this case, Thomson spectrometer behaved as camera obscura and spatially separated ions that passed through the pinhole but had different origin geometry, resulting in registering two distinguishable, yet partially overlapping proton traces [53].

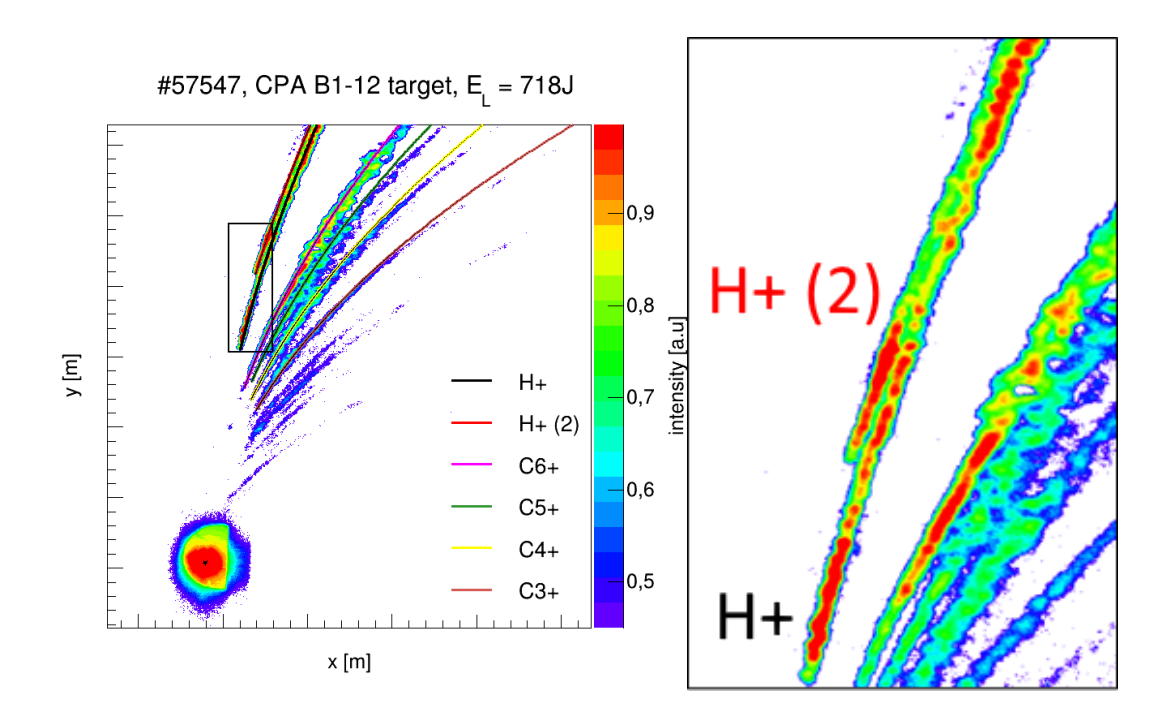


FIGURE 3.12: Ion traces captured by Thomson Parabola Spectrometer together with fitted theoretical curves (left), zoomed in region representing two displaced proton traces (right).

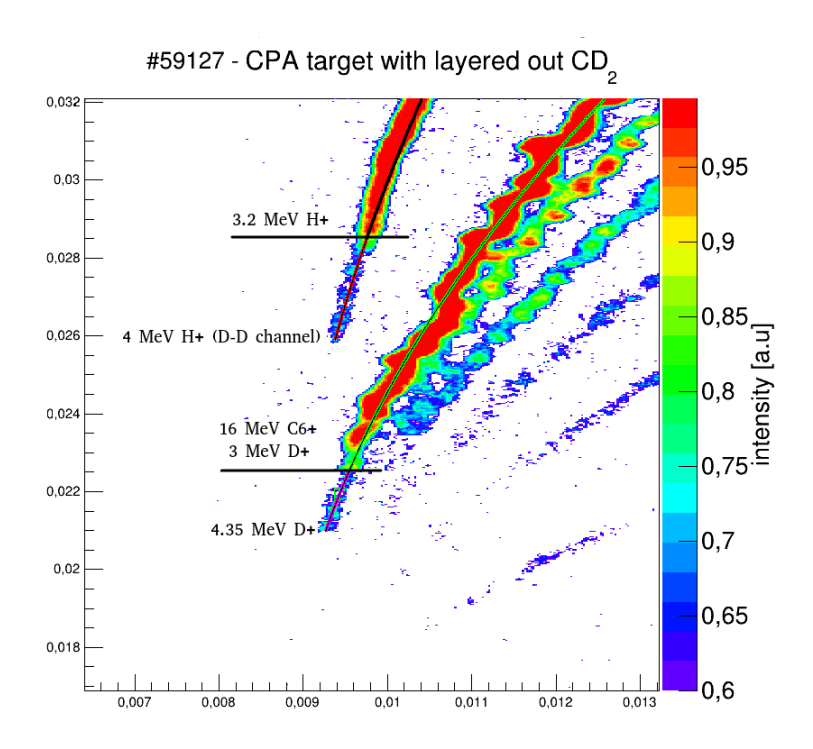


FIGURE 3.13: Identified ion traces captured using Image Plate. Visible drop in intensity of trace is an evidence of overlapping two parabolas of different origin (proton traces on left) or different ions of same  $\frac{q}{m}$  (carbon/deuterium ion trace on right).

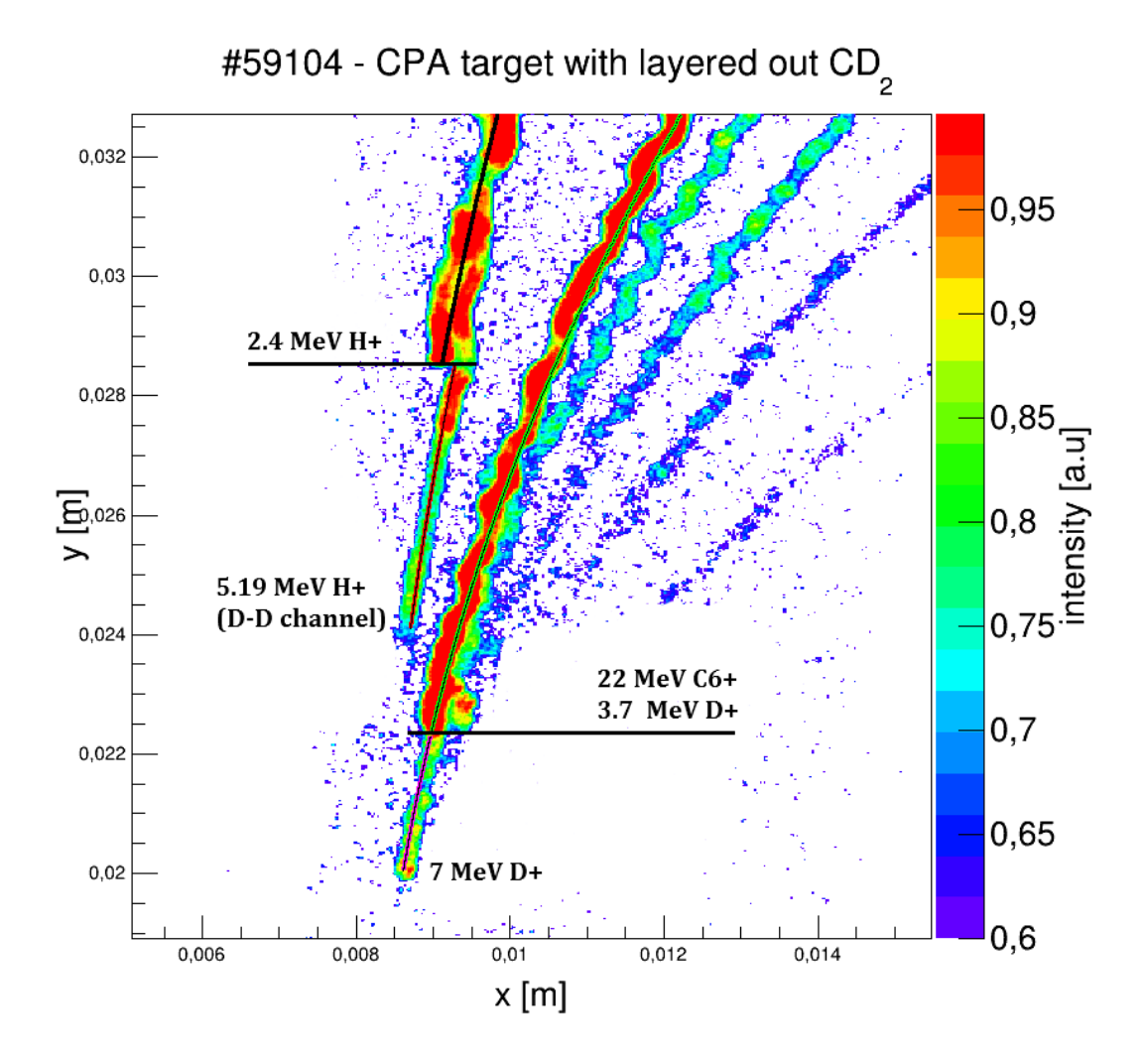


FIGURE 3.14: Zoomed in region corresponding to high energy ions with clear evidence of double-parabola formations.

The similar effect was visible in numerous shots for trace representing ions with charge-to-mass ratio  $\frac{q}{m} = \frac{1}{2}$ . The most common ions represented by this trace are fully ionized ions of carbon,  $C^{6+}$ . In most cases the source of these are contaminations covering the surface of the targets. However, during these experiments ions of deuterium (which share same charge-to-mass ratio as  $C^{6+}$ ) were also accelerated, resulting in sharp drop of intensity of parabolic trace due to overlapping of these two ion kinds on the same parabola (Figure 3.13, 3.14).

The two registered proton bunches not only have different origin, which implicates that these were produced in different processes, but also exhibit different shape of energy spectrum and energy range (Fig. 3.15). The maximal energy by far exceeds value expected from protons created during DD reaction  $E_{p_{DD}^+} = 3.02\,MeV$ . Presented TPS results were recurring for all types

of targets presented on Fig. 3.10, which leads to conclusion that the critical condition for described effect is related with confining the plasma inside the cavity and is not dependant on flyer-ablator geometry. This suggest that simplifying the geometry, i.e applying variant c of Fig. 3.10, might be beneficial when higher repetition of laser pulses is expected in experiment due to easier repositioning of the target. Moreover, the expected peak in energy spectrum near 3 MeV is not visible in majority of collected data (Fig. 3.16).

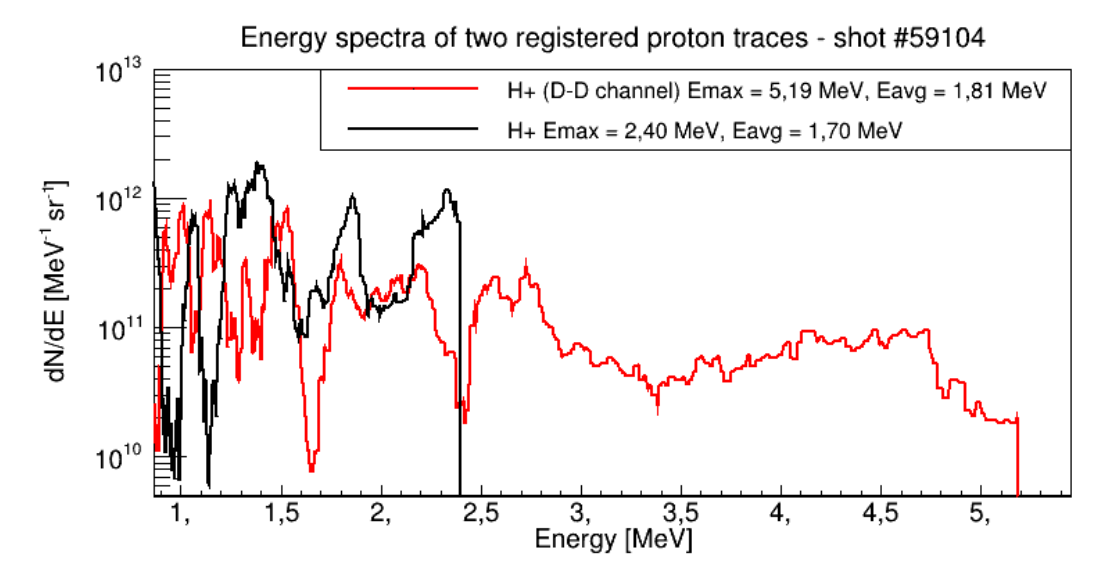


FIGURE 3.15: Energy spectra of protons extracted from concurrent proton parabolas obtained in shot no. 59104 (Fig. 3.14)

#### TPS proton energy spectrum for various shots

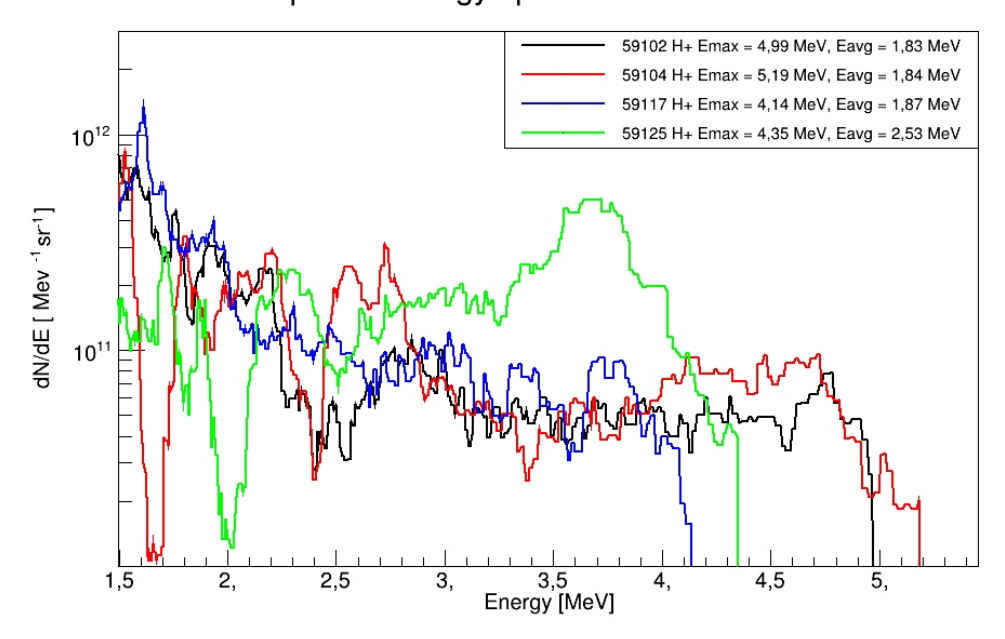


FIGURE 3.16: Examples of DD-induced proton energy spectra from different shots performed in described PALS experiment.

The possible explanation is that DD-originated particles were further accelerated in vicinity of extreme electric fields arising during this particular approach to laser-matter interaction, leading to increase of the maximal energy of the measured particles, thus flattening the observed spectrum. This phenomenon is yet to be further investigated and properly modelled.

Information about protons with energies equal or higher than  $E_{p_{DD}^+}$  can be compared with number of neutrons registered during the shot, eventually confirming obtained neutron yield. Therefore, during recent experimental session for a series of shots where the most energetic protons were expected (in this case shot no. 59104), CR39 track detector was installed in special holder near the entrance to the TPS system.

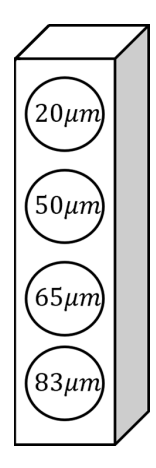


FIGURE 3.17: Schematic picture of track detector holder equipped with Al foils of different thickness used in described experiment.

The holder consisted of 4 sections of entrance holes, each row being covered with different thickness of aluminium foil filters. Thickness of the filters was carefully chosen to enable differential analysis of the number of pits, which could be then cross-checked with the TPS results. To do so, calculations employing Bethe-Bloch formula made in SRIM [67] and LISE++ [68] were performed. The cut-off energies (minimal energies of the particles possible to be registered on the surface of the detector) of chosen set of aluminium foils are presented in the table below.

Such choice of filters allowed to estimate number of DD-originated protons in the sections covered with 83  $\mu m$  Al foil. According to literature [69, 55], in case of protons the size of the pits is decreasing with the particle energy for given etching time. Thus, number of the pits of the biggest diameter should correspond with protons slightly exceeding  $E_{p_{DD}^+}$ . The CR39 detector was placed 50 cm away from the cavity target, 1 cm below the TPS

line of sight. After the experiment, track detectors were etched in NaOH 6.25M solution, bathed at 70 °C. The duration of etching was being chosen according to number of visible pits revealed on the surface of the detector. In case of shots where deuterized cavity was used, due to extraordinary amount of craters emerging in relatively short etching time, the etching process had to be stopped after 60 minutes. For filter thickness lower than 65  $\mu m$  (Fig. 3.18, 3.19) number of pits was too high, resulting in saturation of the detector, eventually making analysis of these sections impossible. The standard approach to analysis of track detectors is based on not only number of tracks, but also measurement of their diameter which allows to distinguish particular ion species and their energy. Presented photographs show that extraordinary number of pits, even for the thickest applied filters, caused the detectors to be nearly saturated, eventually preventing author from performing energy-resolved calculations.

Thickness [µm]	Cut-off energy for protons [MeV]
20	1.75
50	2.25
65	2.65
83	3

TABLE 3.1: Cut-off energy of protons for different thickness of Al filters calculated in SRIM code.

Fortunately, condition of the most important sections corresponding to cut-off energies equal 3 MeV allowed to count the biggest visible craters, which correspond to protons produced in DD reaction. The analysis was carried out using ImageJ software [70], where automatic track counting function is implemented. Due to large amount of tracks and risk of malfunction of the counting algorithm, an area of  $1mm^2$  was selected to count the pits using the software and then to calculate total number of particles at given energy per steradian, which resulted in number  $n_{p@3MeV}=1.3\times10^{10}\frac{1}{sr}$ . This value stands in good agreement with number of neutrons detected using BD-PND detectors (2.15  $\pm$  0.42  $\times$  10 $^9$ , roughly 20% difference in favour of CR39) and proton data obtained by means of TPS ( $\sim$  7  $\times$  10 $^{10}$ , roughly 20% difference in favour of TPS).

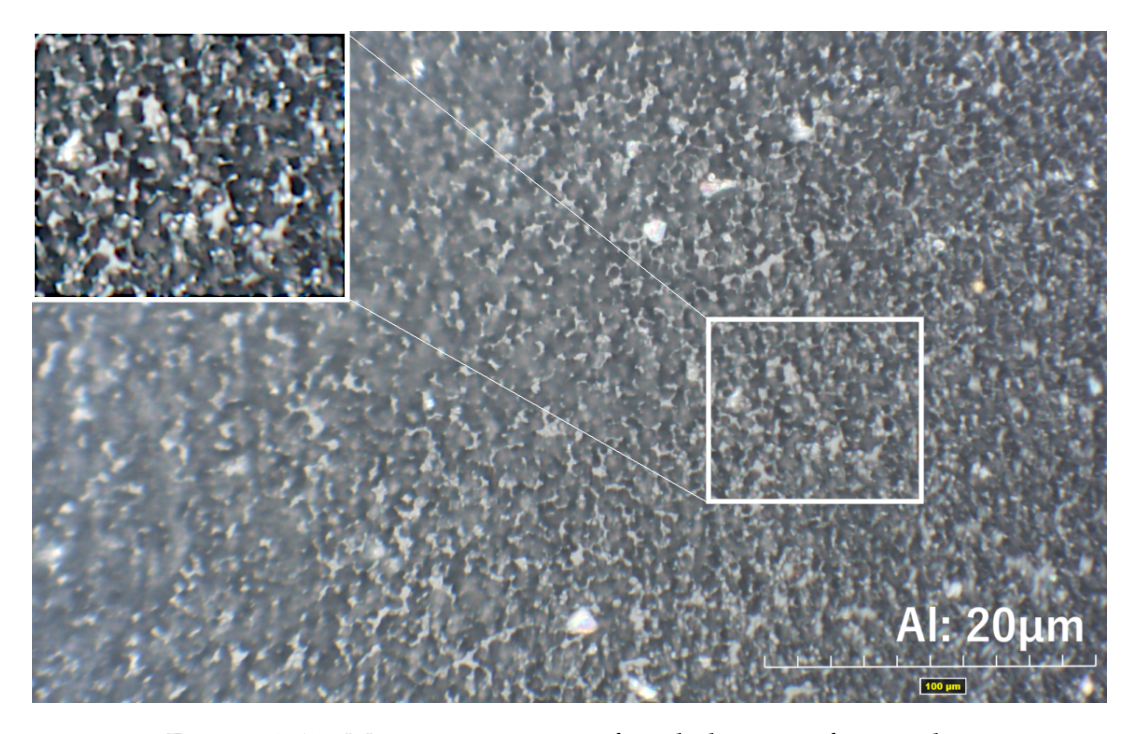


Figure 3.18: Microscopic image of track detector after irradiation through 20  $\mu m$  Al filter.

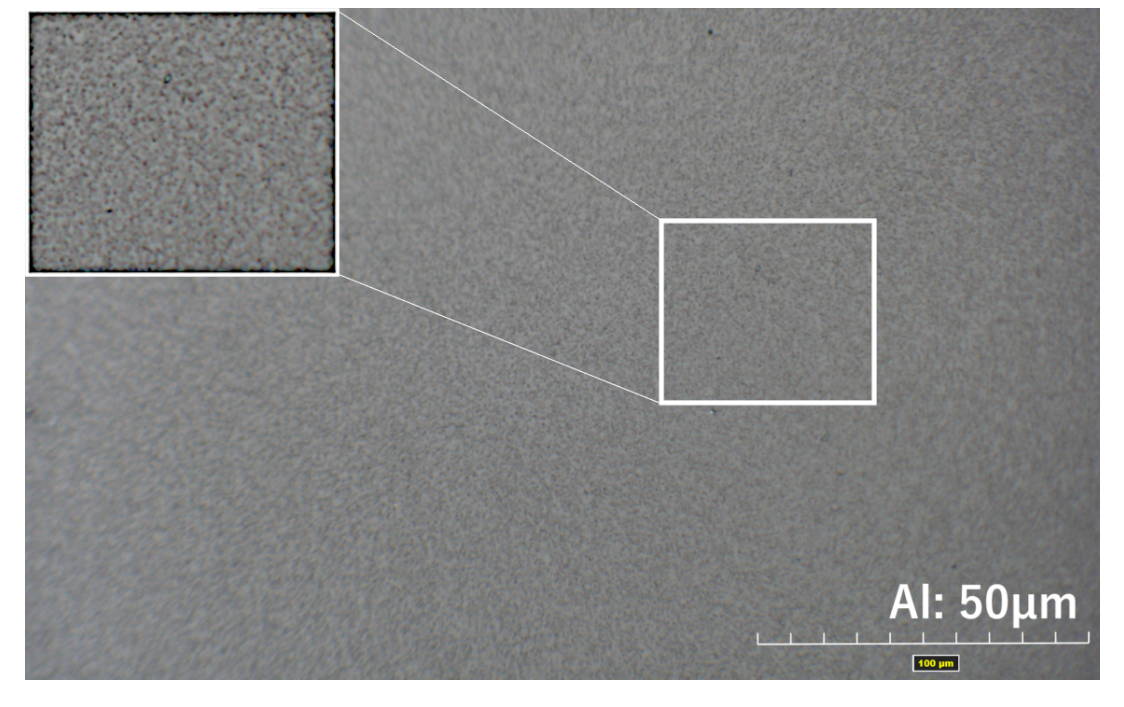


Figure 3.19: Microscopic image of track detector after irradiation through 50  $\mu m$  Al filter.

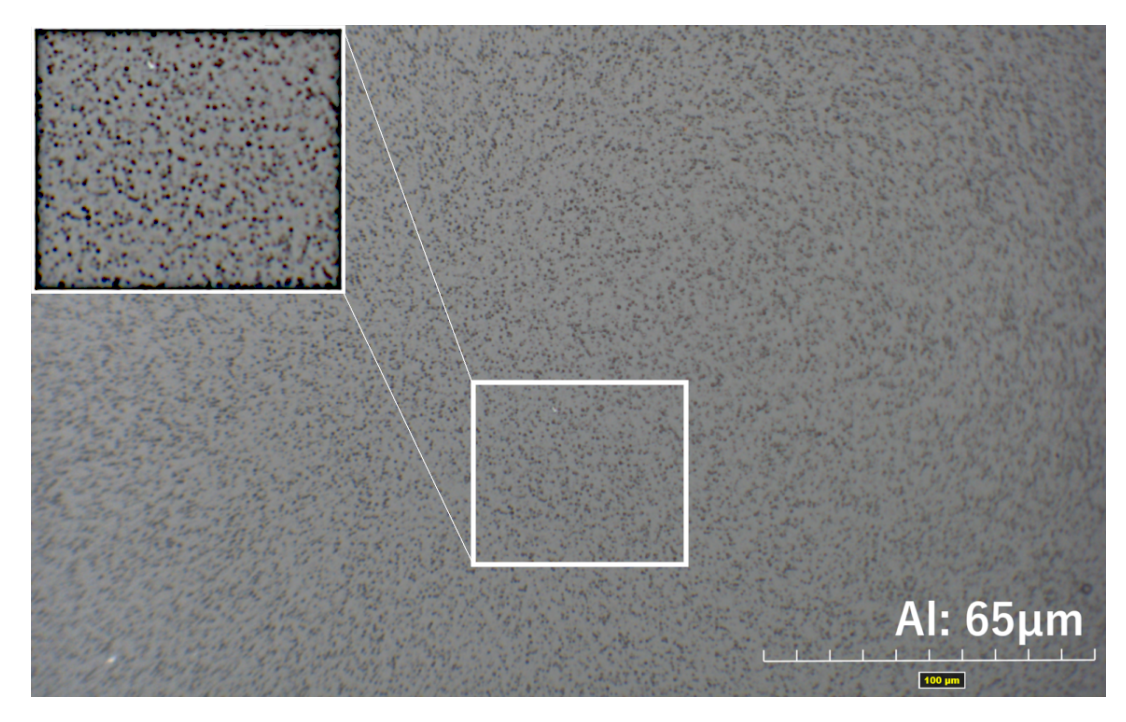


FIGURE 3.20: Microscopic image of track detector after irradiation through 65  $\mu m$  Al filter.

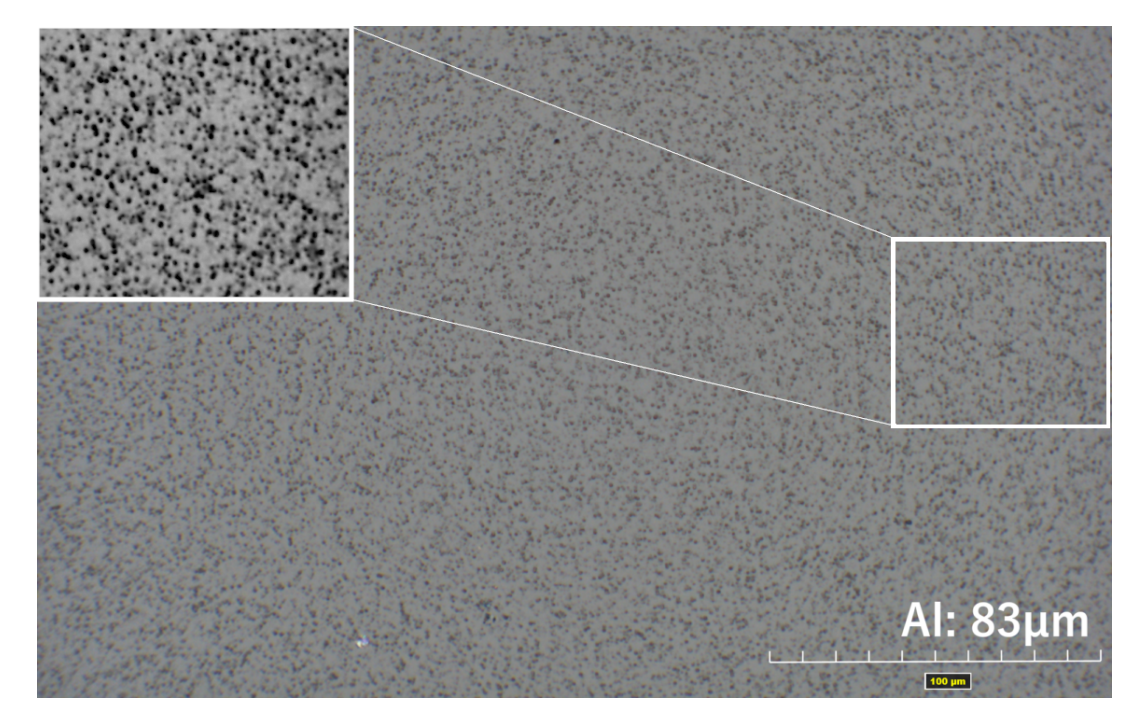


FIGURE 3.21: Microscopic image of track detector after irradiation through 83  $\mu m$  Al filter.

## 3.2.2 Post-experimental FLASH simulations: PALS laser pulse interaction with cavity target

To assess the potential of applied cavity dimensions in driving D-D fusion reaction, MHD simulations similar to these presented in Section 2.1 were performed with the geometry of cavity used in shot 59104, in which the best (in terms of proton energy) results were obtained, following the simulation parameters displayed in Table 3.2.

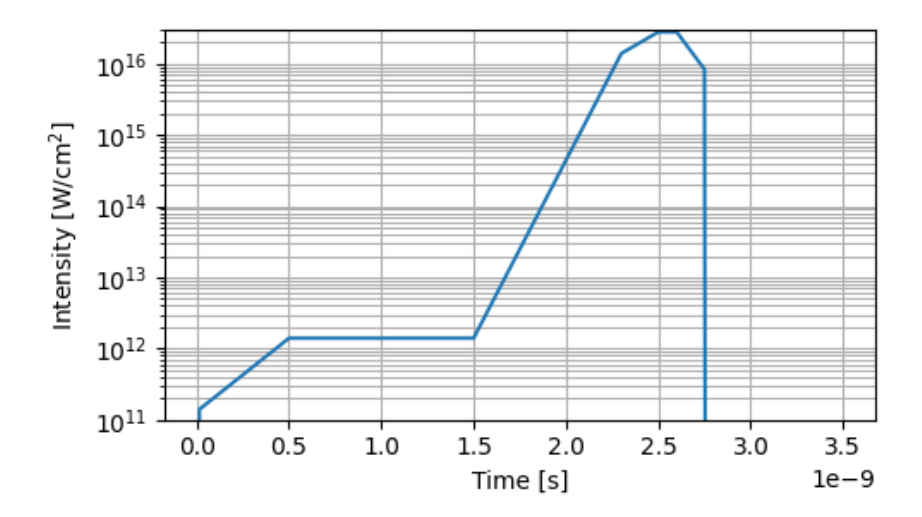


FIGURE 3.22: Temporal profile of PALS laser pulse intensity used for post-experiment simulations of laser-matter interaction with cavity target. The temporal profile is based on experimental data.

The important feature of this particular laser system is extended pedestal of the produced pulse. Although the FWHM value of pulse duration is equal to  $\tau = 350~ps$ , the actual laser-matter interaction lasts for up to several nanoseconds, depending on the desired pulse duration. Obtained levels of intensity allow to produce dilute pre-plasma, which affects the interaction process. In order to take this effect into account, the temporal intensity profile used in simulations was based on intensity profile obtained via contrast measurements performed during one of the experimental sessions (Figure 3.22).

Spatial 2D distributions of tracked parameters (density, electron temperature and pressure) reveal that the time difference between the start of laser-matter interaction and the time at which corona of the polyethylene plasma reached cavity wall was equal to  $t_{shock} = 2.2 \, ns$  (Figure 3.23). Due to the fact that this moment occurs during duration of the energy deposition, while intensity peak of laser pulse is still interacting with the material, it can be

stated that the effect of Cavity Pressure Acceleration was present. After another 1 *ns* the maximum of electron temperature was achieved along the *z* axis of the simulation (Figure 3.24) due to collision of shockwaves reflected from the cavity walls in the centre of the cavity.

Lacor operaty [1]	600
Laser energy [J]	600
Laser wavelength [µm]	1.315
FWHM pulse duration [ps]	350
Focal spot diameter $[\mu m]$	100
Intensity $[W/cm^2]$	$2.2 \times 10^{16}$
Cavity depth [µm]	300
Cavity diameter $[\mu m]$	700
Polyethylene thickness [ $\mu m$ ]	150
Timestep [ps]	100
Simulation length [ns]	10

TABLE 3.2: Parameters used for simulation of PALS laser pulse interaction with the cavity used during experimental session

Based on investigation of the thermodynamical parameters time evolution, it is clear that while both temperature and pressure develop quickly and their highest values are maintained inside the cavity simultaneously for approximately 2 ns (Fig. 3.25), the density of the plasma inside the cavity is not exceeding the value of  $10\frac{g}{cm^3}$ . For this reason, the reaction rate of deuterium-deuterium fusion (that was the source of multi-MeV protons that were detected during the experiment) is far from optimal.

As visible on density distribution presented in Fig. 3.24, due to diameter of the applied cavity, created plasma deflects on the edge of copper wall of the cavity and escapes from the system, which leads to non-optimal performance of the CPA mechanism in terms of dense plasma jet creation. However, the fact that the highest temperature is present with nanosecond-scale delay in respect to the beginning of the interaction corroborate with the experimental observations in terms of two measured proton beams of different energies, discussed in section 3.2.1. The initial proton beam of lower energy is in all probability created before the  $t_{shock}$  due to classical, ablative acceleration processes. The second observed proton beam, where the most energetic protons were detected during the experiment, was produced at later times when high temperature and pressure were maintained inside the cavity. In parallel with temperatures exceeding  $T = 7 \, keV$ , extreme pressure (which according to simulations might increase up to  $100 \, MBar$  inside the cavity (Fig. 3.25) was responsible for deformation of the cavity shape which resulted in

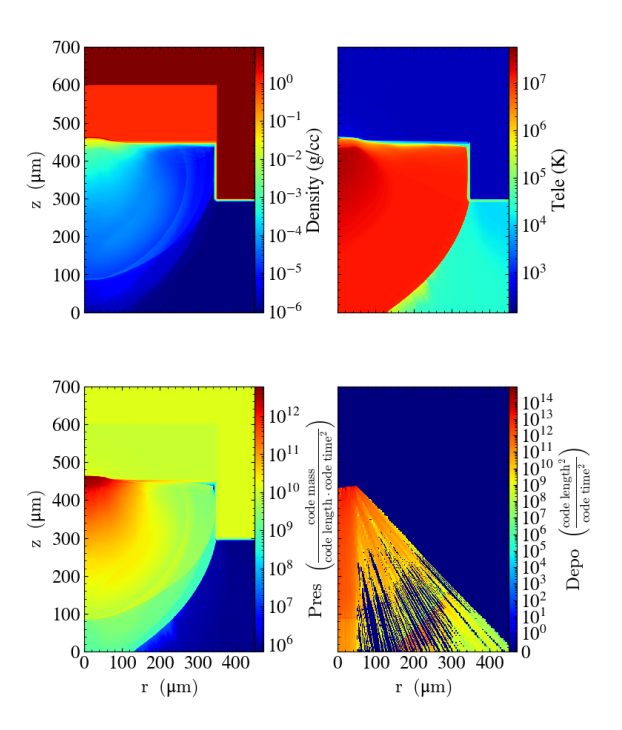


FIGURE 3.23: 2D distributions of density (upper left), electron temperature (upper right), pressure (bottom left) and deposited laser energy (bottom right) for cavity used during PALS experiment at 2.2 *ns* of simulation time.

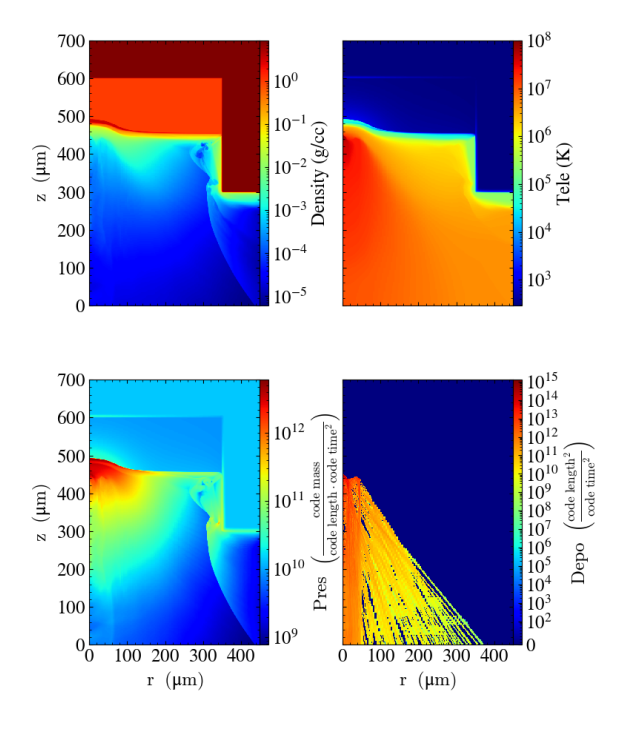


FIGURE 3.24: 2D distributions of density (upper left), electron temperature (upper right), pressure (bottom left) and deposited laser energy (bottom right) for cavity used during PALS experiment at 3.2 *ns* of simulation time.

spatial displacement of the secondary parabola as reported in section 3.11. Furthermore, the time at which the parameters relevant to fusion were noticeably increased suggest the moment at which the additional accelerating force was present which is important finding in context of identifying the mechanism responsible for increasing the energy of protons above the value expected from the D-D reaction, which is one of the goals of future research on discussed topic.

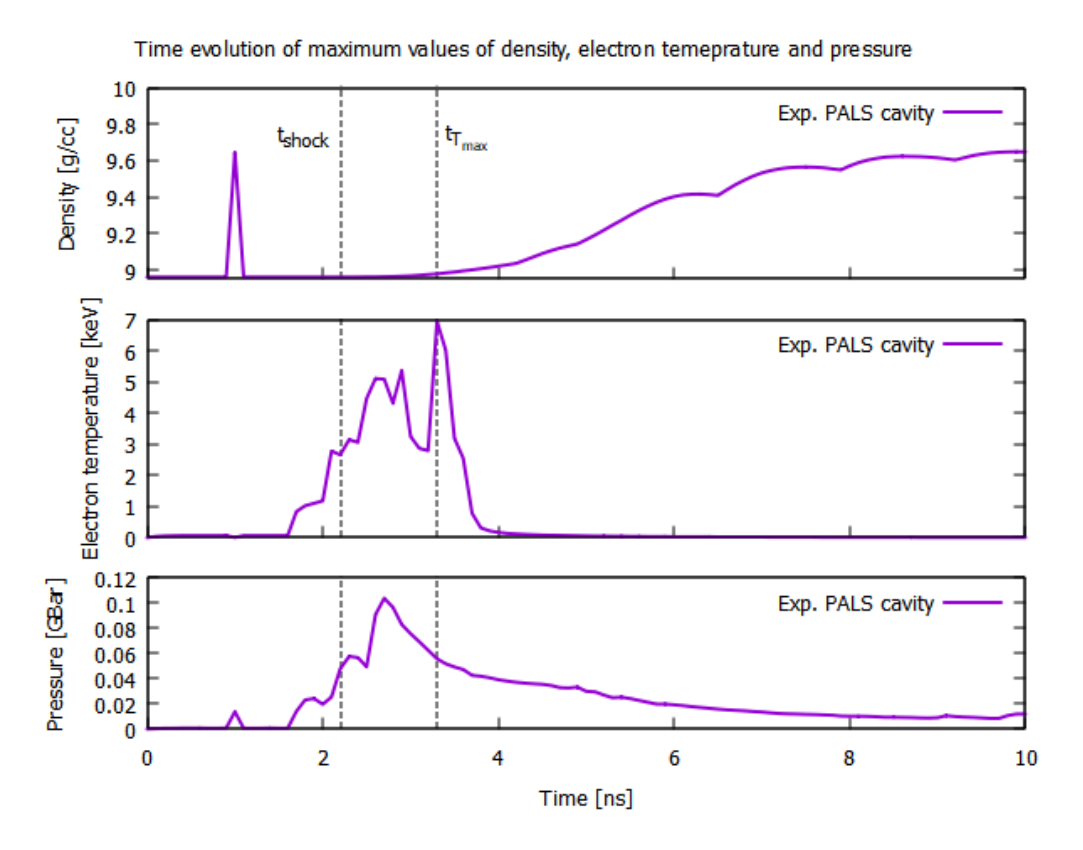


FIGURE 3.25: Time evolution of maximum values of thermodynamic parameters during simulation time for cavity used during PALS experiment

# 3.2.3 FLUKA simulations for CPA-induced proton beam energy spectrum

Coherent results from different diagnostics encouraged attempts to examine possibility of using such DD-CPA accelerated proton beam in proton-boron reaction and compare them with basic, TNSA-oriented approach presented earlier in this thesis. Similarly to previous set of FLUKA simulations, a number of calculations were performed to find optimal thickness of boron catcher when using proton beam enhanced with particles coming from Cavity Pressure Acceleration.

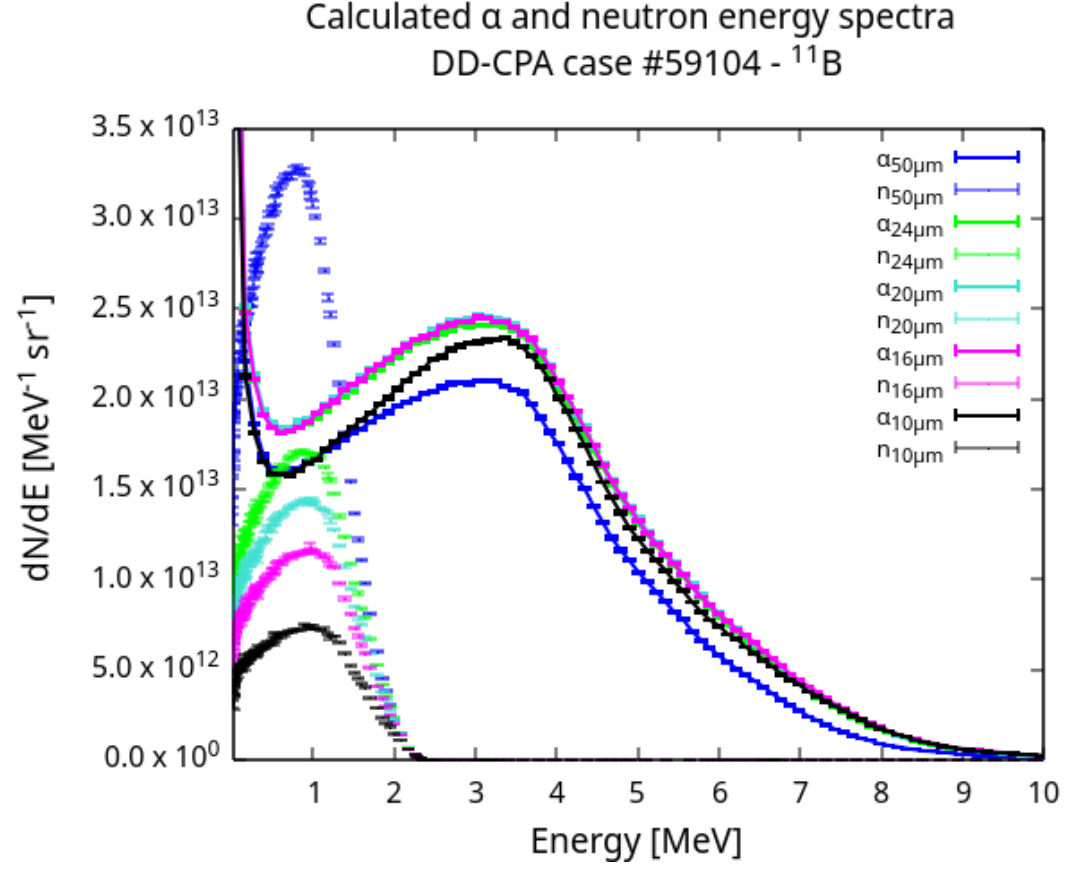


FIGURE 3.26: Alpha particle energy spectrum for different thickness of pure boron-11 catcher - calculated in FLUKA using energy spectrum obtained in shot no. 59104.

Basing on performed Monte Carlo simulations, using such proton beam would result in wide energy spectrum of produced alpha particles, peaking near 3.5 MeV and reaching maximum energies up to 10 MeV (Fig. 3.26). The latter stands in great agreement with previous experimental works of different groups [36, 39, 42]. In contrary to case of using proton spectrum obtained in HPLL, the energy range of proton beam obtained during DD-CPA scenario

enables generation of neutrons when colliding with  $^{11}B$  target, resulting in scoring neutrons of gaussian-like distribution with energies up to 2.3 MeV (Fig. 3.26), which number increases almost linearly up to  $50 \, \mu m$  thick target and reaching plateau for target thicker than  $120 \, \mu m$  (Fig. 3.27). According to obtained results, the optimal target thickness for the highest yield of alpha particles requires catchers in range of  $20-30 \, \mu m$  (Fig. 3.27), at which the neutron yield remains relatively low.

#### Produced particles yield as a function of target thickness

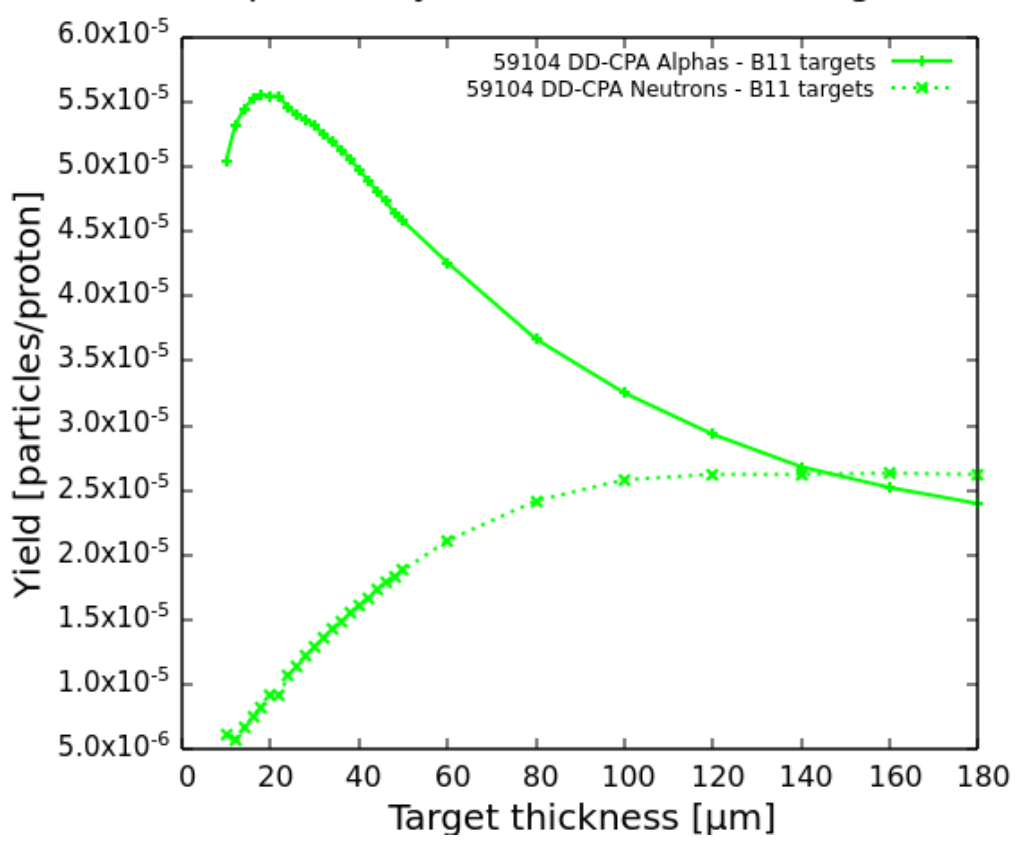


FIGURE 3.27: Total alpha particle (solid line) and neutron (dashed line) yield as a function of catcher thickness.

For target thickness exceeding 140  $\mu m$  the number of scored neutrons is exceeding the number of alphas. This is due to the stopping of  $\alpha$  particles in the target volume due to electronic and nuclear stopping power, opposite to charge-less neutrons which are only affected by collisions. To visualize this effect, 2D USRBIN scoring of the alpha particles fluence inside the target was performed for  $20-120~\mu m$  and  $300~\mu m$  thick targets. As seen on Figure 3.28, alphas are evenly distributed along the target and they are visible on both front and rear sides of the boron catcher (Fig. 3.29). As the target thickness increases, less alphas are reaching the rear side of the foil (Fig. 3.30, 3.31).

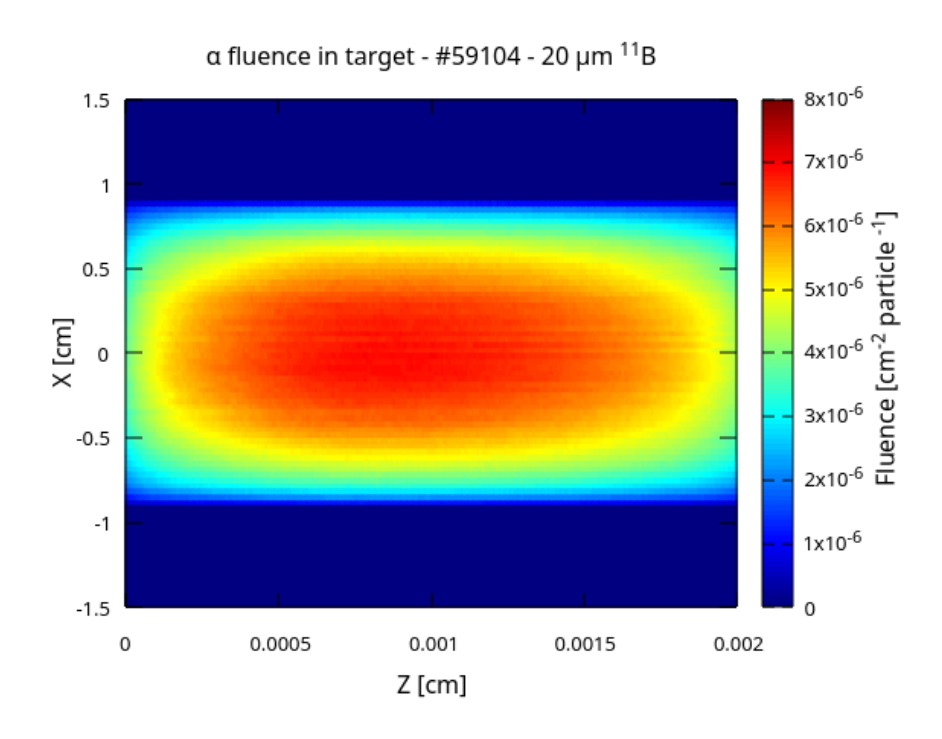


FIGURE 3.28: 2D map of residual alpha particles fluence in 20  $\mu m$  pure boron-11 target volume.

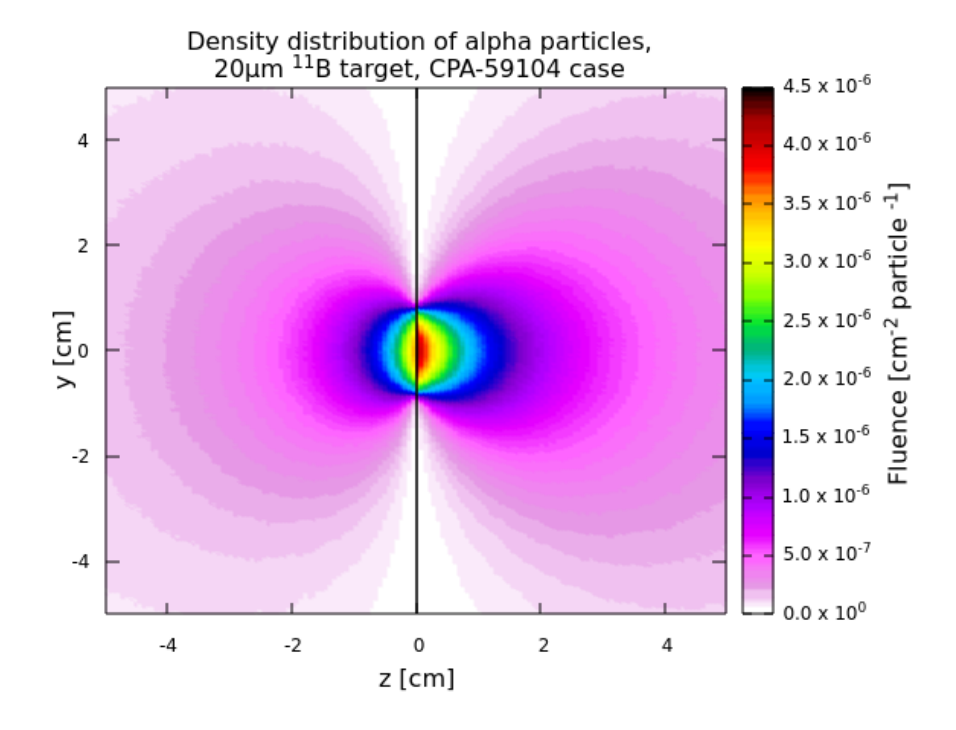


FIGURE 3.29: 2D alpha particle distribution for 20  $\mu m$  boron-11 catcher for shot no. 59104 proton spectrum.

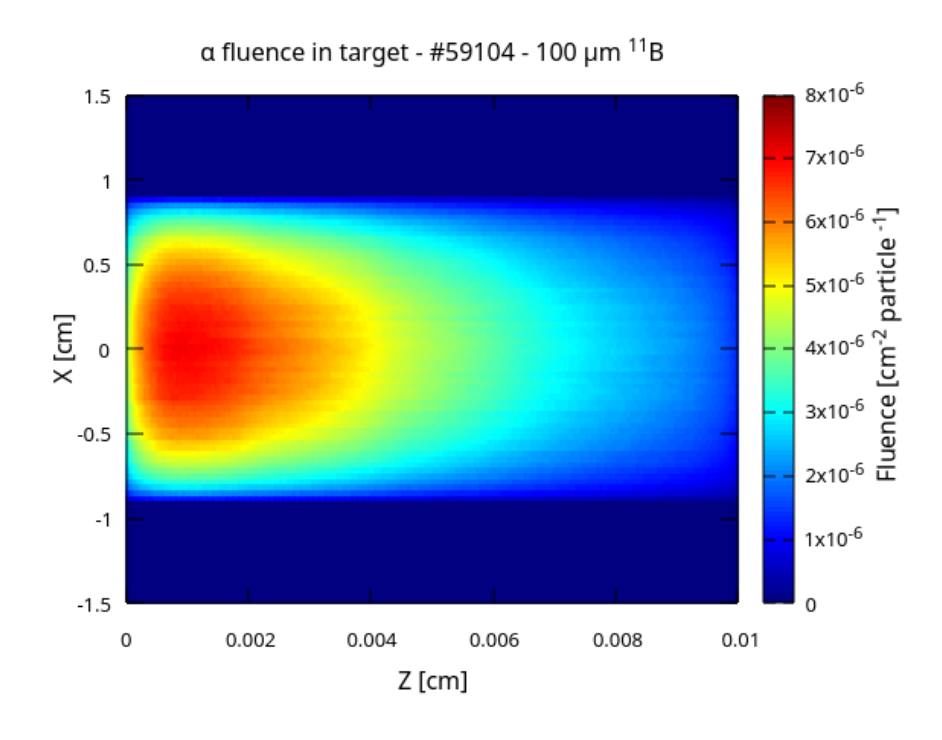


FIGURE 3.30: 2D map of residual alpha particles fluence in 100 μm pure boron-11 target volume.

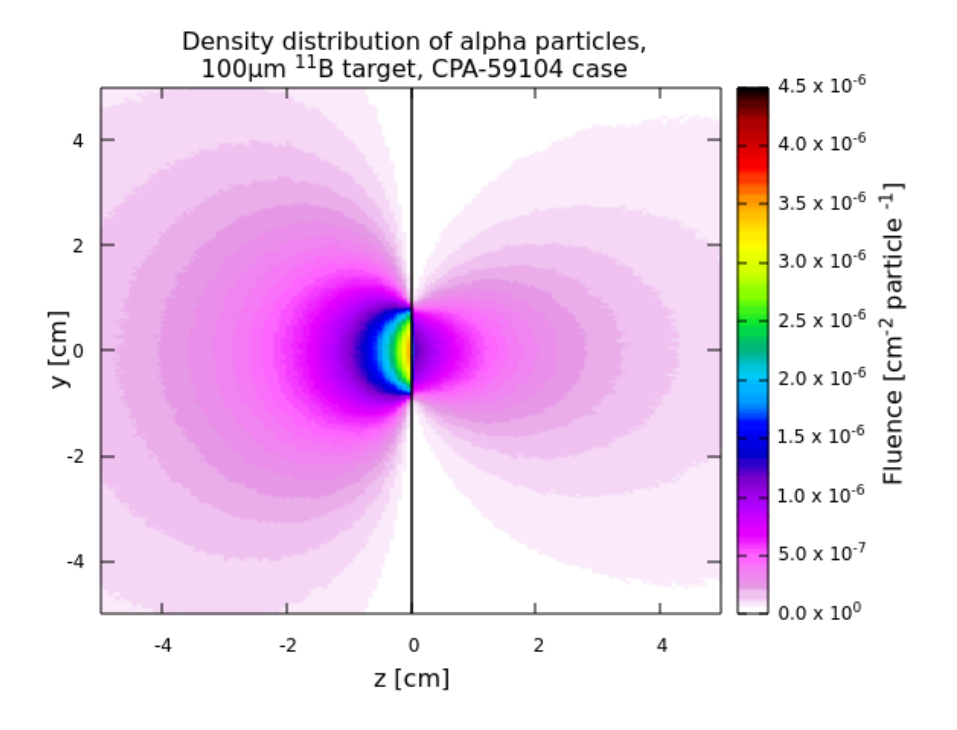


FIGURE 3.31: 2D alpha particle distribution for 100 µm boron-11 catcher for shot no. 59104 proton spectrum.

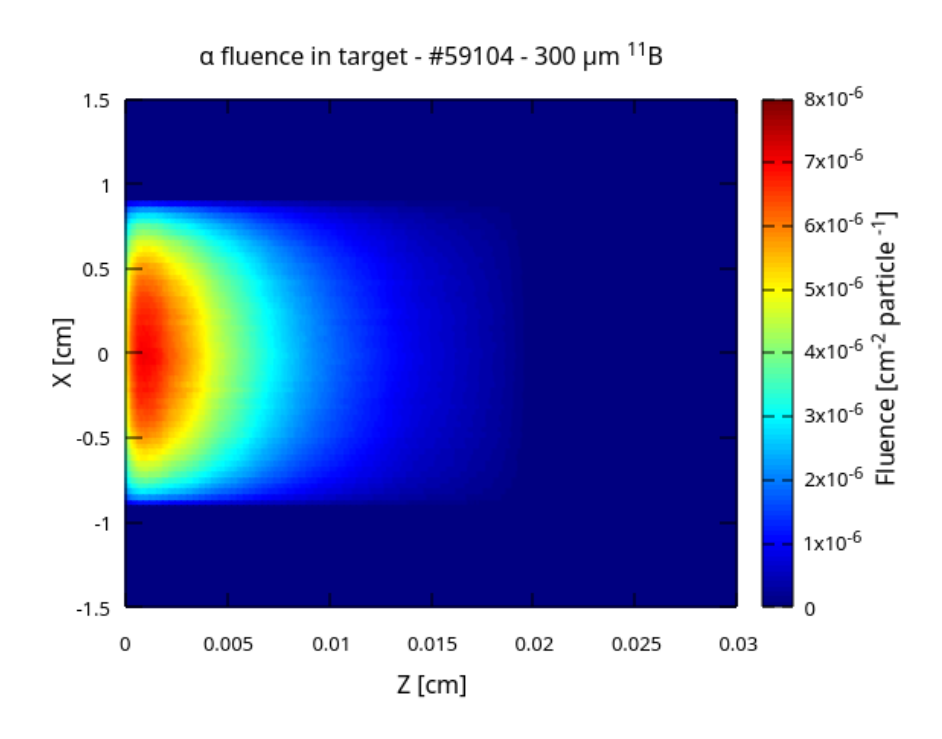


FIGURE 3.32: 2D map of residual alpha particles fluence in  $300 \, \mu m$  pure boron-11 target volume.

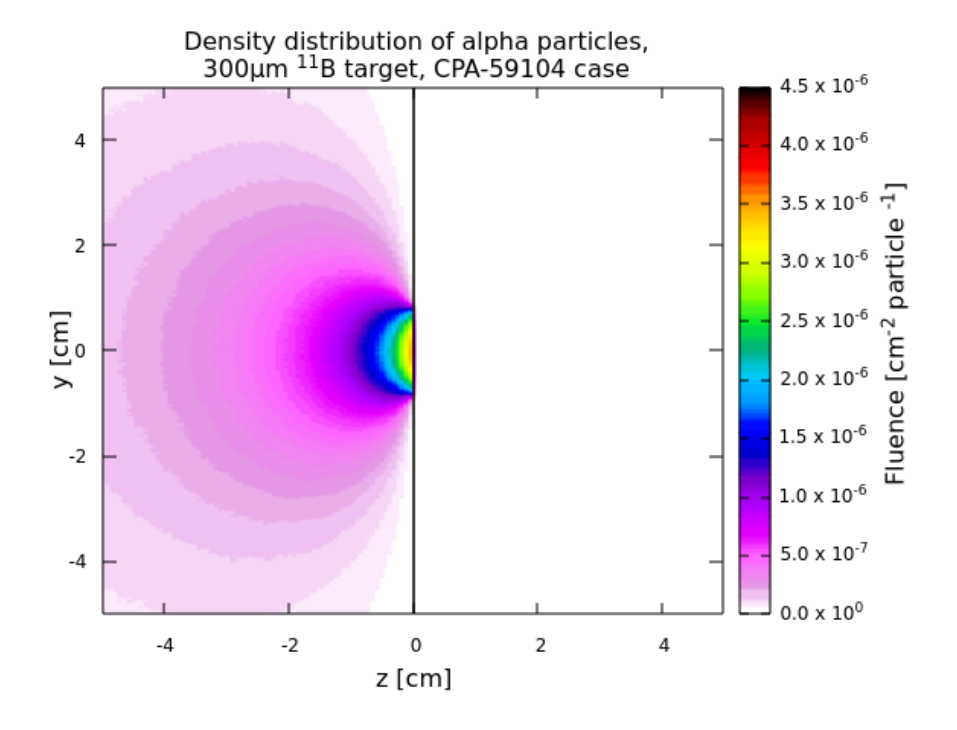


FIGURE 3.33: 2D alpha particle distribution for 300  $\mu m$  boron-11 catcher for shot no. 59104 proton spectrum.

As visible on Figure 3.32, the alpha particles cannot penetrate further than 200  $\mu m$ , effectively resulting in the absence of  $\alpha$  behind the target for thicker targets (Fig. 3.33).

Although for optimal target thickness the neutron yield is relatively low, minimizing number of produced neutrons in secondary reactions such as  $^{11}B(p,n)^{11}C$  and  $^{11}B(p,n)^{14}N$  (products which leads to  $^{14}N(\alpha,n)^{17}F$ ) is important from the radiation threat point of view and of high importance for considered fusion reaction, which aneutronic character should be preserved as much as possible. Therefore, additional simulations were carried out, this time replacing pure  $^{11}B$  with natural boron, which consists of two boron isotopes - 80%  $^{11}B$  and 20%  $^{10}B$ . The  $^{10}B$  isotope is widely used in nuclear science as material which mitigates the yield of neutrons through neutron capture reaction [71].

$$^{10}B + n \rightarrow ^{11}B^* \rightarrow \alpha + ^{7}Li + 2.31 \,MeV$$
 (3.2)

#### Produced particles yield as a function of target thickness

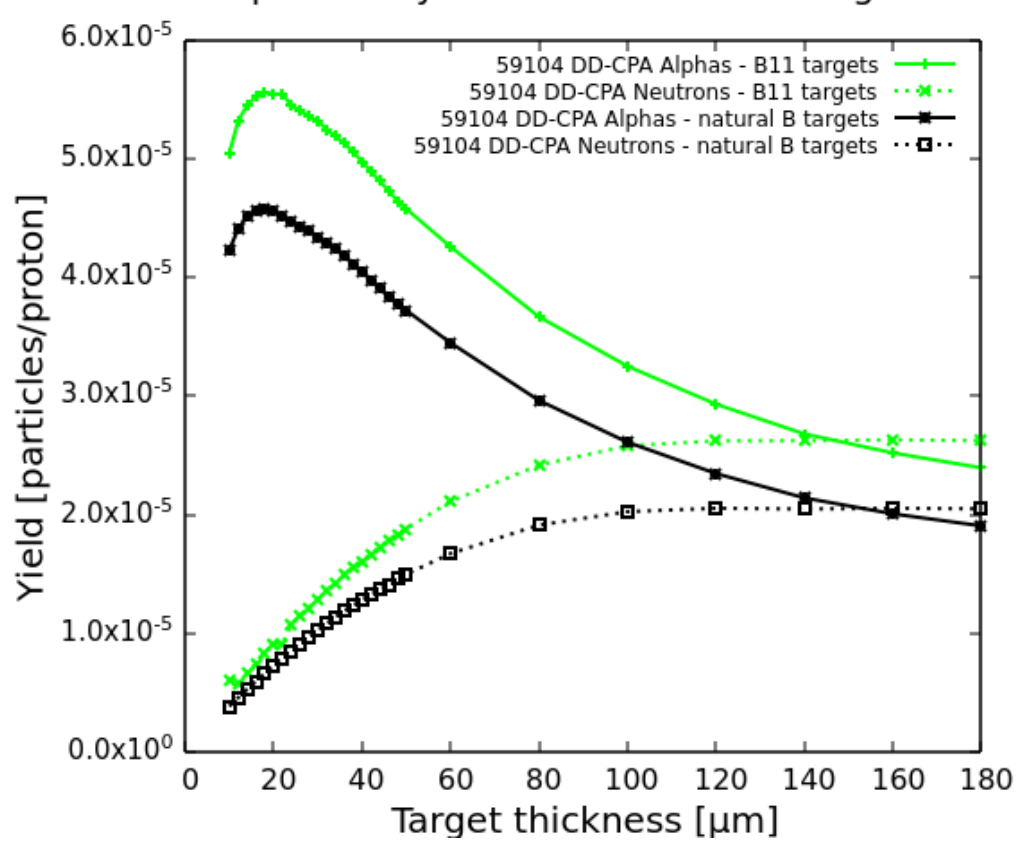


FIGURE 3.34: Total alpha particle (solid line) and neutron (dashed line) yield as a function of pure boron-11 (green) and natural boron (black) catcher thickness for shot no. 59104.

Moreover, above reaction produces alpha particle, which suggests potential impact in terms of increasing total alpha yield. Another benefit of using natural boron is being cheaper and more accessible than pure  $^{11}B$  foils. The results for targets composed of natural boron in fact carry lower number of neutrons, however the amount of produced  $\alpha$  particles is 20% lower comparing to pure  $^{11}B$  catchers at given thickness. This suggests that no actually impactful neutron capture is taking place in case of natural boron targets and the difference in  $^{11}B$  content between pure  $^{11}B$  and natural boron (80%  $^{11}B$ , 20%  $^{10}B$ ) is the only factor responsible for these results.

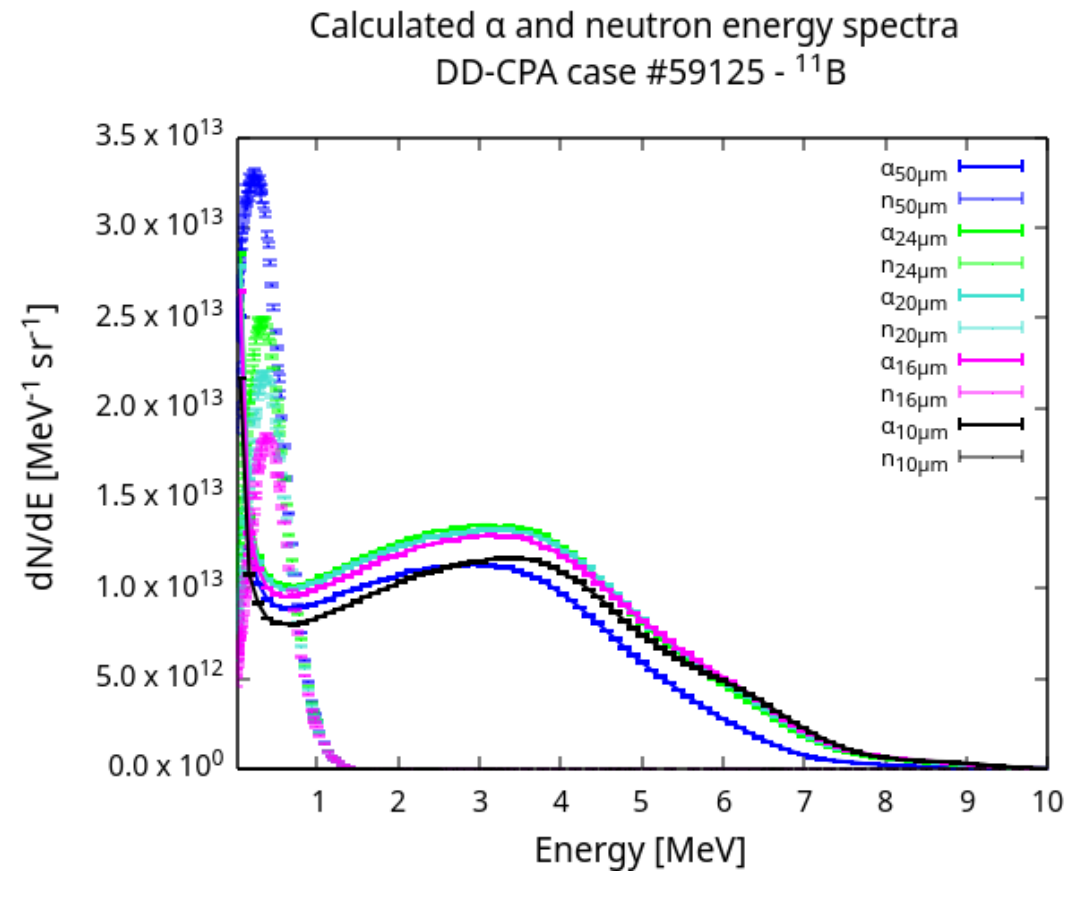


FIGURE 3.35: Alpha particle energy spectrum for different thickness of pure boron-11 catcher - calculated in FLUKA using energy spectrum obtained in shot no. 59125.

While in most cases the energy spectrum of protons reconstructed from the TPS measurements remained relatively flat for energies exceeding 1.5 MeV, one particular case of shot number 59125 (green line, Fig. 3.16) should be emphasized due to visible peak centred at  $E_{p^+} = 3.7 \, MeV$ . As discussed in previous section 3.2.1, the presence of very strong spontaneous electric field

leading to acceleration of DD fusion generated protons resulted in broadening of energy spectra, allowing protons to reach energies by far exceeding range available in other acceleration mechanisms at given laser intensity. However, the shape of energy spectrum of shot 59125 indicate that significant amount of protons remained in energy range which could be expected from process employing nuclear DD reaction. Therefore, a similar set of FLUKA simulations was performed, using proton spectrum from this shot, in order to evaluate the impact of obtained characteristics of the proton beam on the proton-boron reaction.

While energy spectrum of alphas scored during simulations shows similar shape comparing to previous calculations, the population of neutrons presents narrow, strong peak with maximum energy below 1.5 MeV (Fig. 3.35). The total number of produced neutrons reach plateau at 50  $\mu m$  thick targets (Fig. 3.36), however contrary to previous results (Fig. 3.34) number of produced neutrons never exceeds the alpha yield.

#### Produced particles yield as a function of target thickness

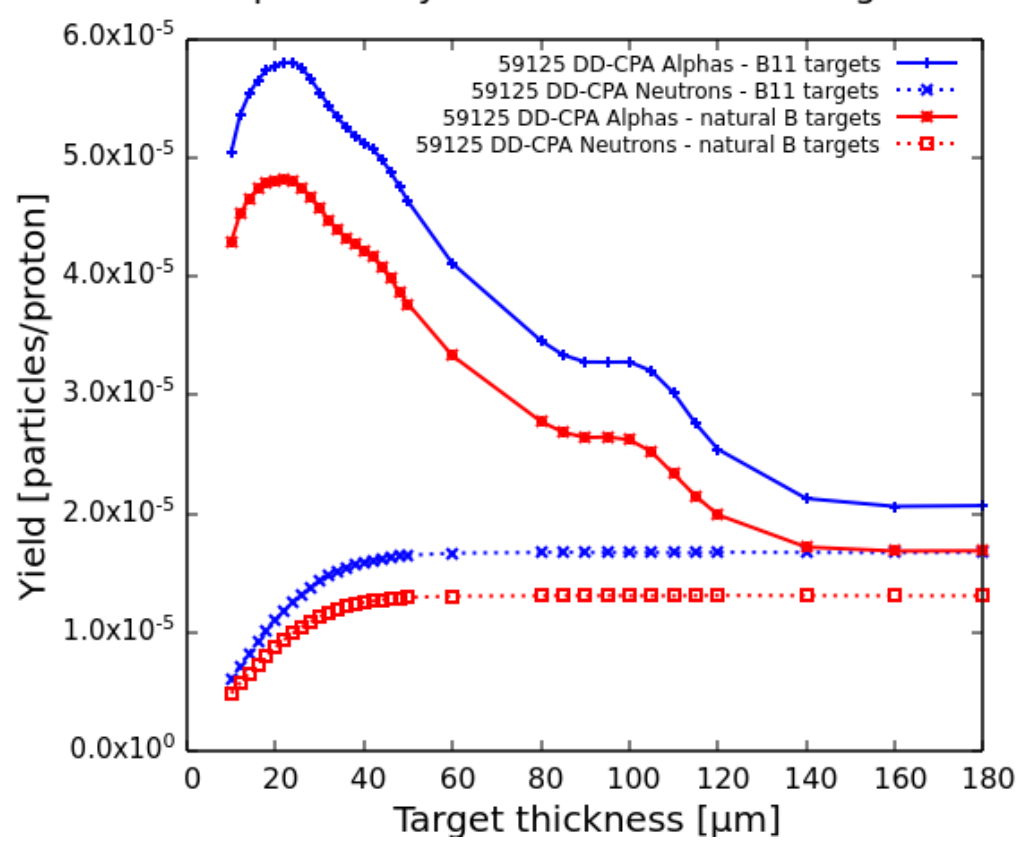


FIGURE 3.36: Total alpha particle (solid line) and neutron (dashed line) yield as a function of pure boron-11 (blue) and natural boron (red) catcher thickness for shot no. 59125.

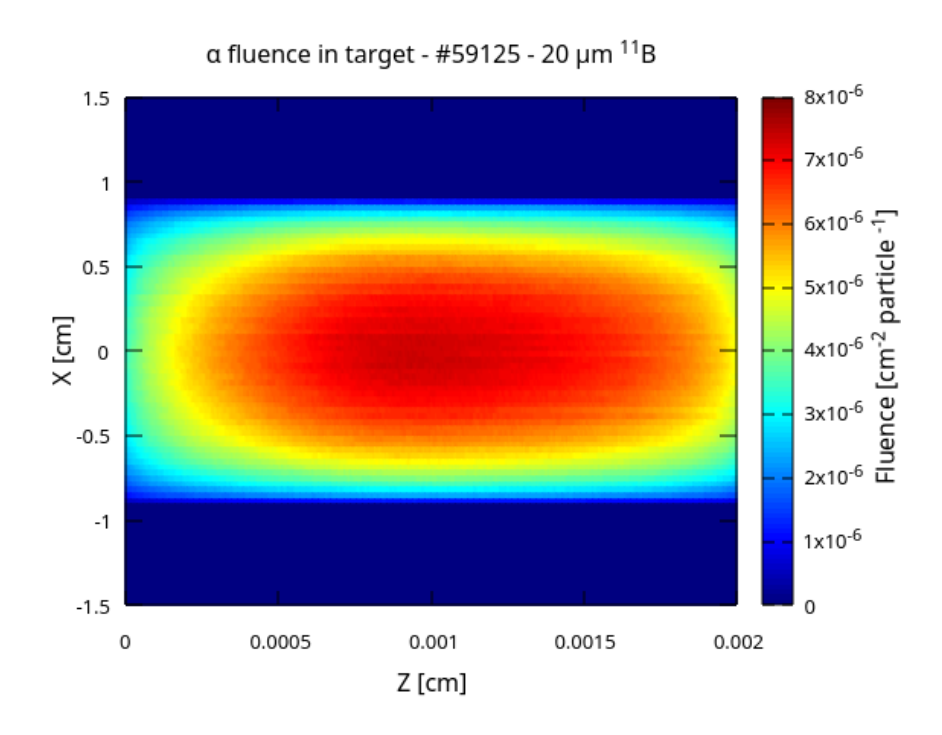


FIGURE 3.37: 2D map of residual alpha particles fluence in 20 *µm* pure boron-11 target volume (shot no. 59125).

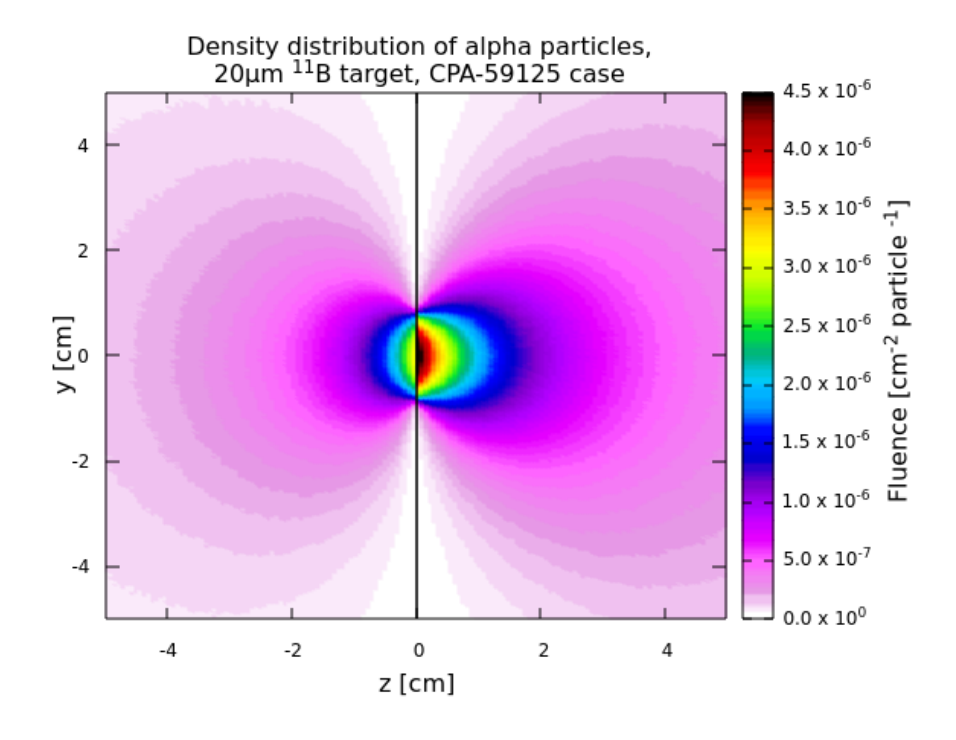


FIGURE 3.38: 2D alpha particle distribution for 20  $\mu m$  boron-11 catcher for shot no. 59125 proton spectrum.

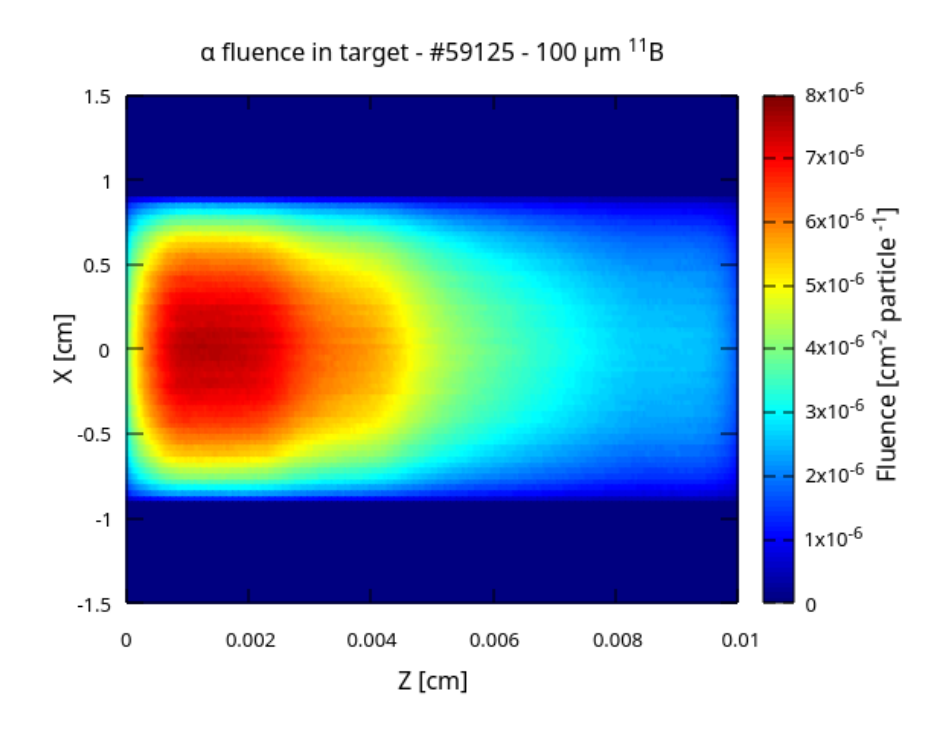


FIGURE 3.39: 2D map of residual alpha particles fluence in 100 μm pure boron-11 target volume (shot no. 59125).

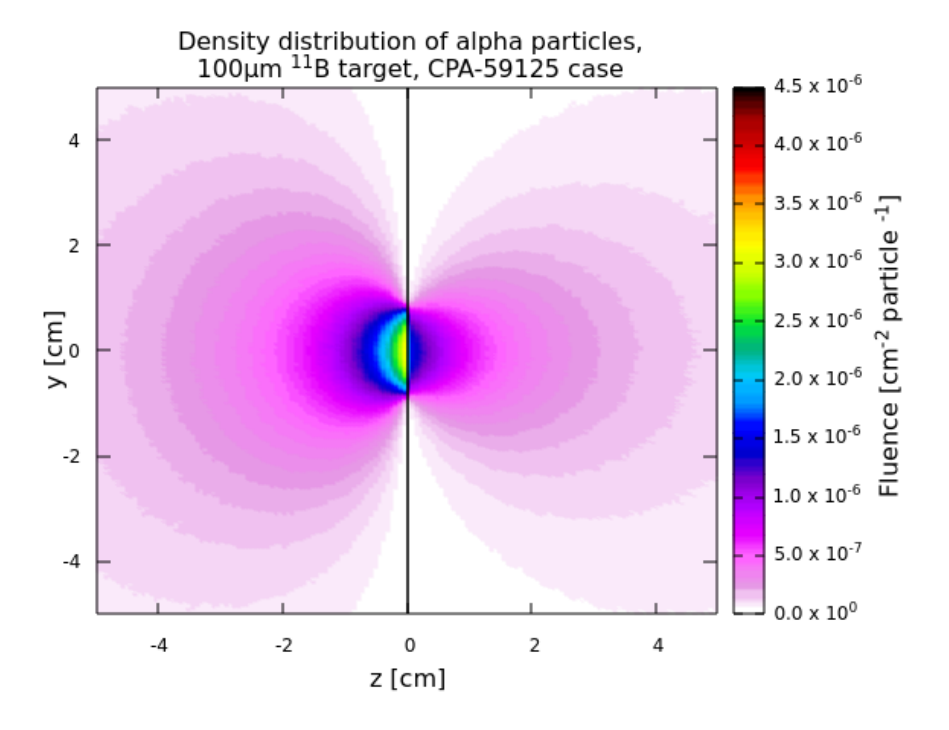


FIGURE 3.40: 2D alpha particle distribution for 100 μm boron-11 catcher for shot no. 59125 proton spectrum.

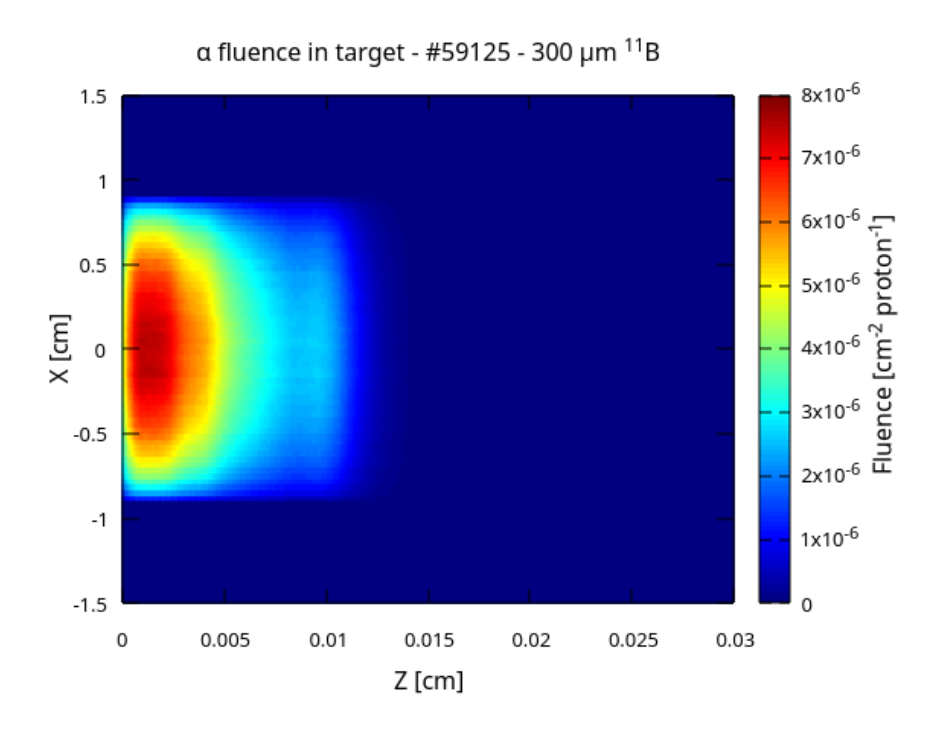


FIGURE 3.41: 2D map of residual alpha particles fluence in 300  $\mu m$  pure boron-11 target volume (shot no. 59125).

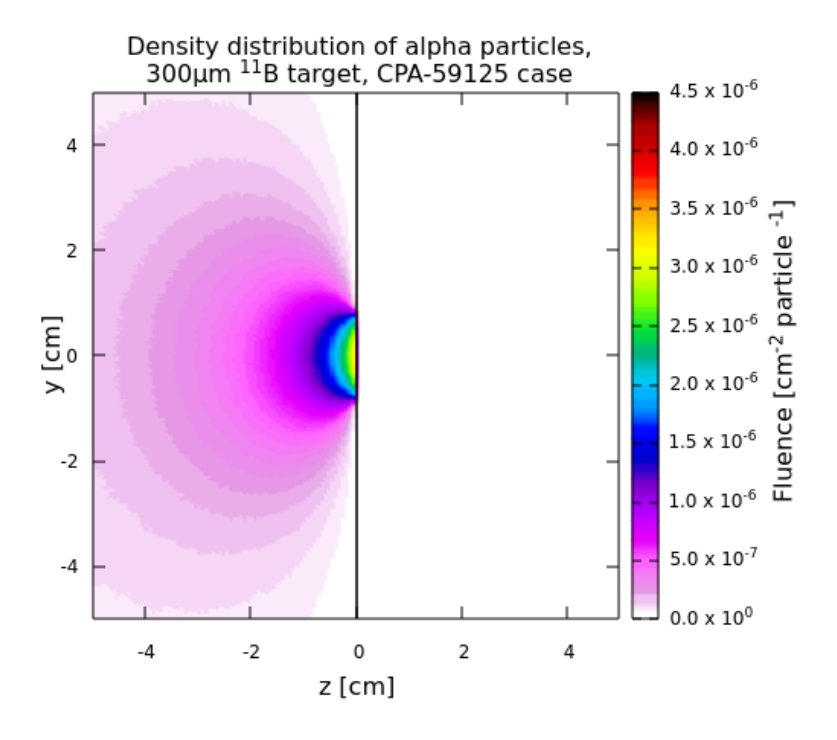


FIGURE 3.42: 2D alpha particle distribution for  $300~\mu m$  boron-11 catcher for shot no. 59125 proton spectrum.

Another worth mentioning feature is visible peak showing the increase of the number of alpha particles for thickness between  $80~\mu m$  -  $120~\mu m$ . Considering that proton beam spectrum used for this case exhibited quasi-monoenergetic feature, once again the profile of alpha particles fluence inside the target was extracted and presented on Figures 3.37 - 3.42.

As visible on Figure 3.41, there is an increase of number of the alpha particles located roughly  $100 \, \mu m$  deep in the  $300 \, \mu m$  thick target. This is due to fraction of protons with energy  $\sim 3.7 \, MeV$  slowed down to the energy corresponding to the main resonance in proton - boron cross section at  $675 \, keV$ , which results in increase of the alpha yield in this range of catcher thickness (Fig. 3.43).

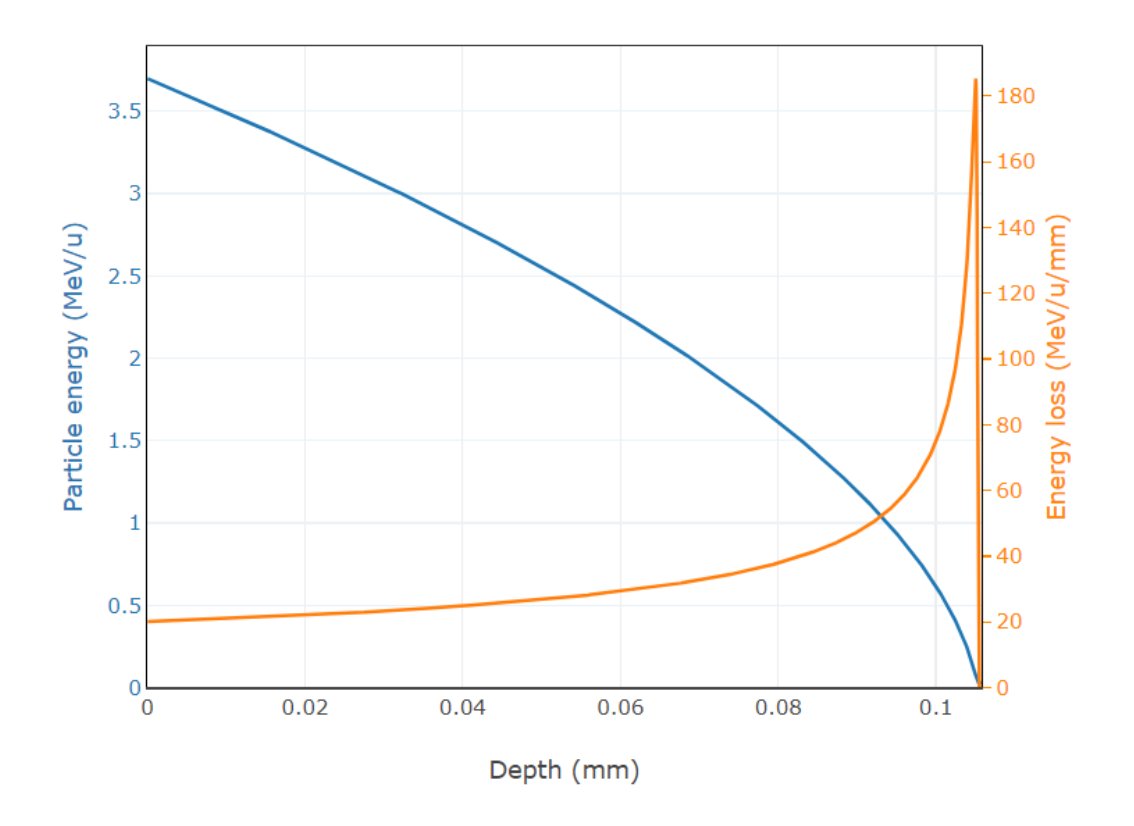


FIGURE 3.43: Result of Bethe-Bloch calculation of stopping 3.7 MeV proton in pure <sup>11</sup>B. Calculation was made using tool available at https://web-docs.gsi.de/ lestinsk/beamcalc/bb.php

Total yield obtained with USRBDX scoring estimator in FLUKA is by default given per incident primary – in this case per incident proton. It allows to compare theoretical response to specific shape of energy spectrum of the beam which initiates reactions.

Comparing the results for three described cases, the TNSA-produced proton beam available at HPLL shows nearly 50% lower alpha yield than any of

considered DD-CPA examples, among which the case of proton beam with quasi-monoenergetic peak located near  $3.7 \, MeV$  gives the best results in units of  $\frac{particles}{proton}$  (Fig. 3.44). For targets thicker than  $100 \, \mu m$  the number of alpha particles produced by this proton beam is visibly smaller than for 59104 case, however number of scored neutrons is two times lower per incident proton.

For DD-CPA shots one can normalize the results by multiplying the yield value by total number of protons used for retrieving energy spectra, allowing to quantitatively compare these cases. It is possible due to choice of detector used for TPS measurements, which in this case was Image Plate of BAS-IP TR type, for which calibration curves for various ion kinds are available in numerous articles. In our case, we rely on results collected by collaborative group lead by researchers from Queen's University Belfast [72].

#### Produced particles yield as a function of target thickness

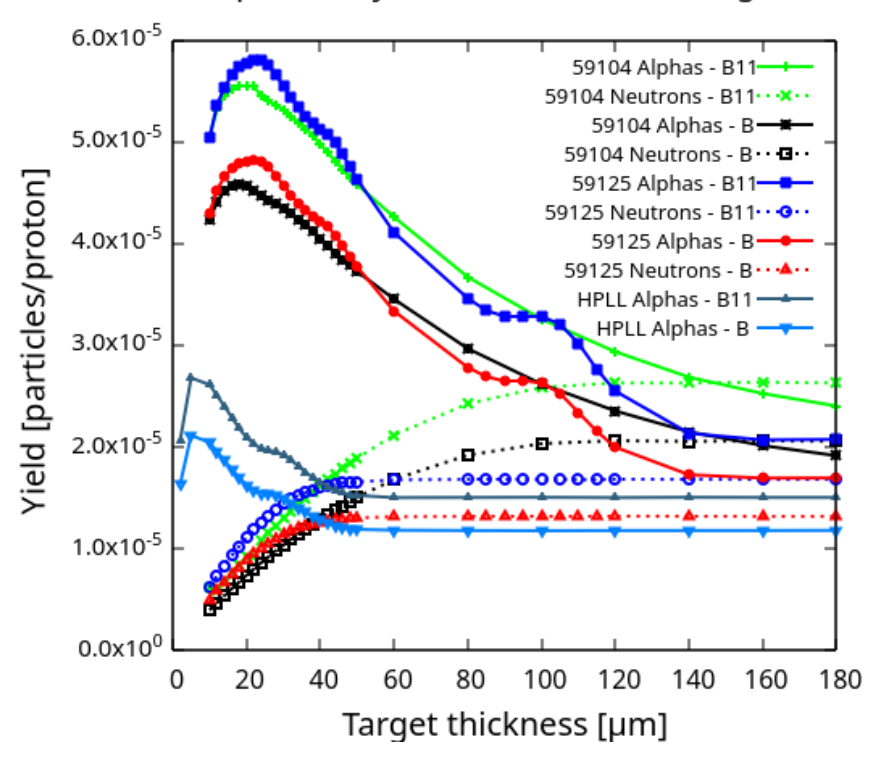


FIGURE 3.44: Total alpha particle (solid line) and neutron (dashed line) yield as a function of catcher thickness - comparison of three described cases.

In contrary, the data obtained for TNSA accelerated protons was collected with multi-channel plate (MCP) coupled with phosphor screen instead of Image Plate, which is yet to be calibrated using monoenergetic particles with either cyclotron or linear particle accelerator. Therefore obtaining quantitative results in this scheme using our TPS is not possible at the moment.

### Produced particles yield as a function of target thickness

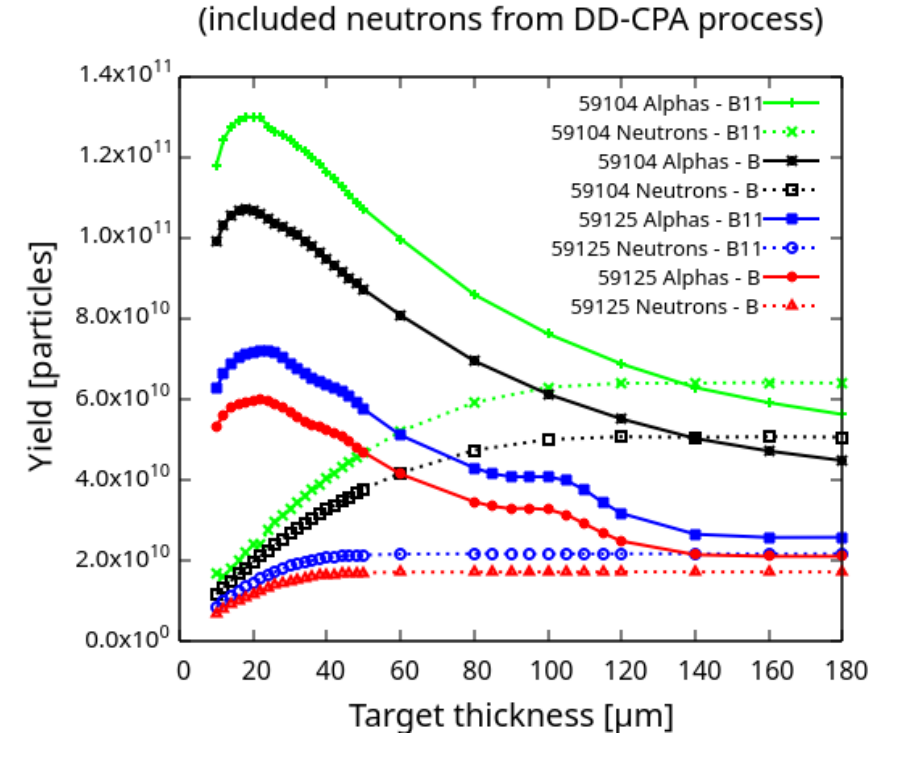


FIGURE 3.45: Total normalized alpha particle (solid line) and neutron (dashed line) yield as a function of catcher thickness

#### Ratio of produced alphas and neutrons for given target thickness

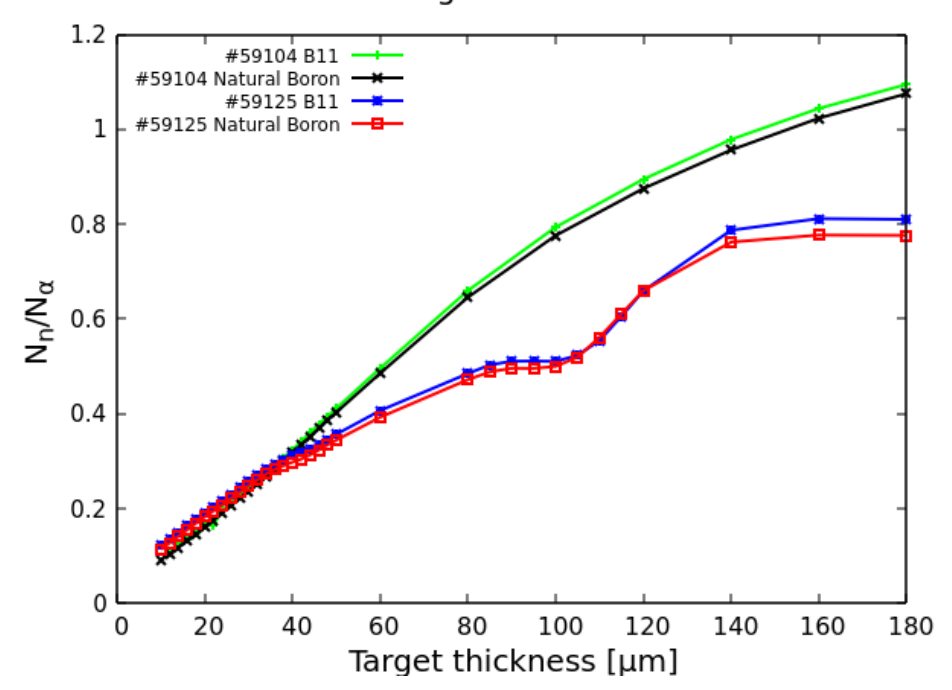


FIGURE 3.46: Ratio of total neutron and alpha particle yield calculated in FLUKA as a function of target thickness.

After taking into account total number of protons obtained from TPS energy spectrum reconstruction, which is equal to  $N_{59104} = 2.43 \times 10^{15}$  and  $N_{59125} = 1.24 \times 10^{15}$  respectively for shots 59104 and 59125, and including number of neutrons measured by means of BD-PND detectors for given cases, the final information of produced alpha particles and neutrons can be obtained (Fig. 3.45).

Important finding of this work is that for considered range of target thickness, the neutron yield can achieve levels comparable to, or even exceed, the yield of proton-boron fusion primary product - alpha particles. Alpha particle and neutron yield dependency on target thickness presented on Figure 3.45 can also be displayed as a ratio of produced neutrons and alphas  $\frac{N_n}{N_n}$  (Figure. 3.46). This approach reveals that the difference in using natural boron instead of pure boron-11 catchers does not lower the production of neutrons in secondary reactions. As presented on Figures 3.26 and 3.35, the energy of scored neutrons is greater than what is considered as "thermal", therefore the neutron capture reaction (which is possible due to the presence of  ${}^{10}B$ ) is not efficient. The positive impact of neutron capture starts to be visible for targets thicker than 140  $\mu m$  when proton beam obtained from shot no. 59125 was used in simulations. The explanation for this is increasing number of collisions between neutrons and nuclei of target atoms together with the target thickness. Nevertheless, this effect is very weak, and is not observed for shot no. 59104 proton beam, which exhibit higher energies of protons. Moreover, in pitcher-catcher scenario considered in this thesis, the shape of energy spectrum of proton beam injected into catcher shows much greater influence on the neutron to alpha ratio than the target's content of boron isotopes. The neutron results need to be adressed as well due to relatively high yield comparing to other works, e.g in article of Bonvalet et al. [43] where neutron yield was reported as 7.4% and 2.3% of total alpha particle number when using 200 µm thick targets for proton energies achieving up to 30 MeV and 10 MeV respectively. In this work, for the most optimal target thickness (which is  $12 \, \mu m$  in terms of alpha-to-neutron ratio), the lowest achieved number of neutrons was equal to 11% as presented on Figure 3.46. This value stands in agreement with result provided by Bonvalet, however (according to presented extensive simulations performed in FLUKA) as the target thickness increase, the neutron number increases rapidly, putting the aneutronic character of proton-boron fusion experiments in doubt. Unfortunately until now, the detailed studies of neutron production in  $p + {}^{11}B$  reaction basing

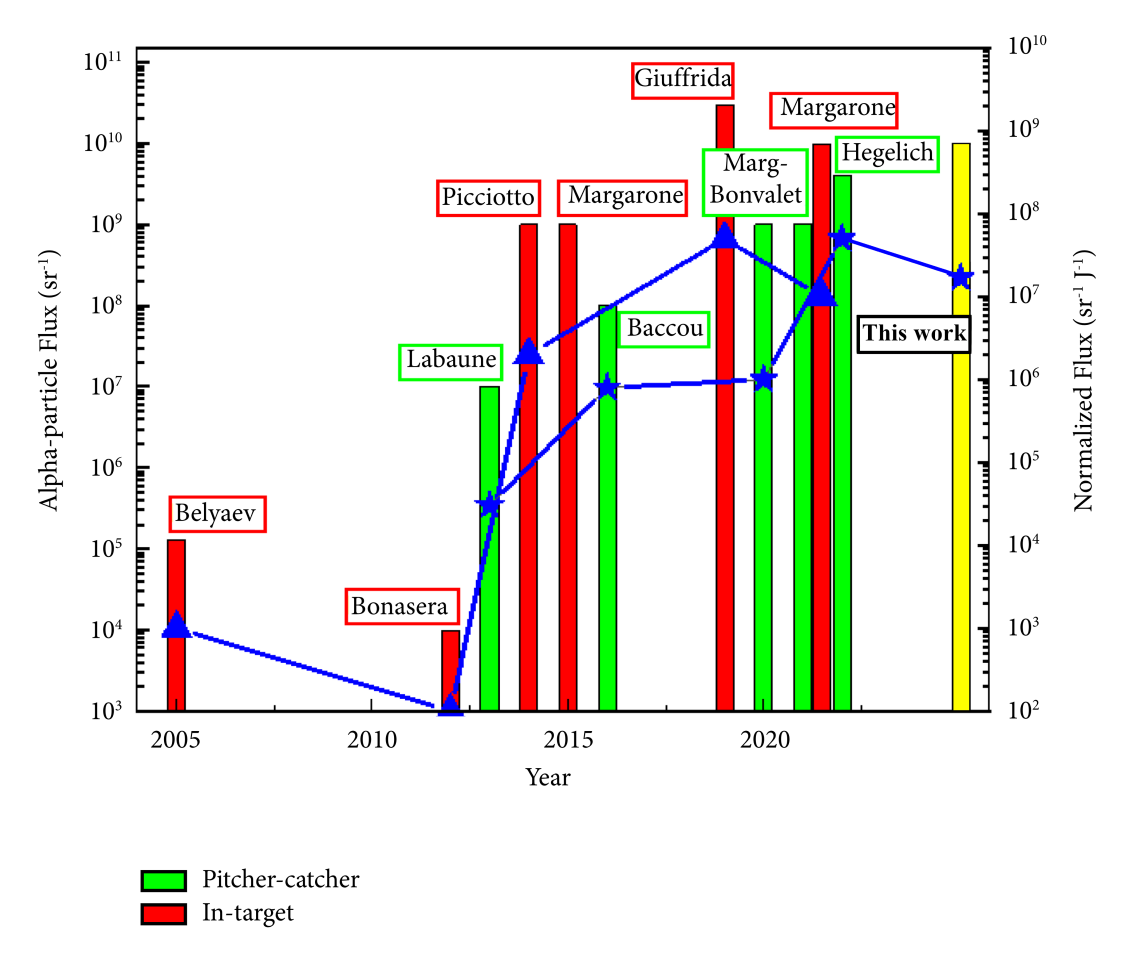


FIGURE 3.47: Numerical results presented in this work compared to experimental campaigns performed in last 20 years. Reused and edited from [35].

on experimental data were not published, which encourages to further investigation of this effect not only numerically by using different Monte Carlo codes, but also in experiments.

The presence of neutrons in principle should not be considered as a disadvantage in this fusion approach as they can be used as in-situ diagnostics in future power-plants [61] and idea of mixed proton-boron fuel (containing fraction of other relevant fusion fuels such as DT or DD) is currently considered in the field [73].

In order to compare numerically obtained values of alpha yield with experimental results presented on Figure 1.13, the dataset was reiterated and displayed on Figure 3.47.

### 4 Conclusions

The results presented in this work demonstrate the possible application of Cavity Pressure Acceleration in laser fusion-related research, at the same time show the potential of using this technique in generation of multi-MeV protons by exploiting the products of deuterium-deuterium reaction as reported in Section 3.2.1. The results obtained via Thomson Parabola Spectrometer were analysed and interpreted using numerical tool designed and created by the Author, described in Section 2.2.2.

The main difference between this approach and other, widely used laser ion acceleration methods is lack of laser intensity dependence on the efficiency of energetic particles acceleration (production) - the discussion made in section 2.1 (which is based on the numerical results obtained for nanosecond kilo-joule class laser) reveal that thermodynamical parameters crucial for driving fusion reactions are exceeding these that are attainable when higher intensity laser systems are used, as it concluded from section 3.2.2. The necessary condition to achieve this is proper choice of the cavity geometry according to pulse characteristics of the particular laser system.

The practical meaning of this fact is opening possibilities to use more accessible, low intensity laser systems to generate streams of energetic particles more efficiently - comparing the energy ranges and number of protons accelerated using Target Normal Sheath Acceleration using 10 TW laser system (presented in Section 3.1) and these achieved with 2 TW laser system (when CPA mechanism with deuterated materials was used) clearly shows potential of described method.

Results of Monte Carlo simulations presented in section 3.2.3 show the benefits of employing Cavity Pressure Acceleration mechanism in pitcher-catcher scenario of proton-boron fusion, which not only allow to obtain alpha yield superior to this guaranteed by traditional TNSA approach using TW-class lasers (discussed in 3.1.2), but also results comparable to these obtained on laser systems capable of delivering few order of magnitude more intense laser pulses (results presented in Fig.3.47).

All of the findings concluded above support the statement:" The intense proton beam generated through thermonuclear reaction of D+D via Cavity Pressure Acceleration method allows to more efficient generation of alpha particles by means of  $p+{}^{11}B\to 3\alpha$  fusion reaction comparing to standard approach to laser ion acceleration methods using TW-class laser system", which is the thesis statement of this work.

The disadvantage of CPA approach is quite complicated target design and significant amount of debris and projectiles that might be launched towards optics and devices placed in the experimental chamber due. The reason for this is extreme pressure, reaching up to 1 Gbar, arising in the cavity during plasma confinement that leads to deformation and in some cases, as our group experienced in past years, launching shrapnels of destroyed cavity housing towards equipment installed in chamber - this effect was minimised when  $CD_2$  powder-filled variant of cavity was used. Nevertheless, both of these issues have to be adressed when high repetition of shots will be expected in the experiment. Another difficulty during performing experiments when deuterium-enhanced CPA method is applied are multiple sources of particular particles of different energies, which are challenging from diagnostic point of view. As an example, using this method in driving proton-boron reaction requires user to introduce precise time-of-flight measurements to discriminate neutrons coming from deuterium-deuterium reaction from those originated from secondary proton-boron reactions.

At the moment of printing this work, majority of experimental results presented and discussed in section 3.2.1 were already published by the Author in peer-reviewed journal [74].

The results of simulations presented in Section 2.1, as well as the Monte Carlo simulations of CPA-produced proton beam interaction with thin boron foils discussed in 3.2.3, are the basis for upcoming experimental campaign, which at the moment of concluding this dissertation is confirmed and scheduled (Autumn 2025) for the L4n laser system, one of the beamlines located at Extreme Light Infrastructure facility (Dolní Břežany, Czech Republic):

"ELIUPM4-11: Hybrid laser-induced proton—boron fusion using nanosecond laser system: benchmark of an approach employing protons produced during thermonuclear D(d,p)T reaction".

- [1] J. Nuckolls et al. "Laser Compression of Matter to Super-High Densities: Thermonuclear (CTR) Applications". *Nature* 1972 239:5368 239 (5368 1972), pp. 139–142. ISSN: 1476-4687. DOI: 10.1038/239139a0.
- [2] C. Labaune. "Incoherent light on the road to ignition". *Nature Physics* 2007 3:10 3 (10 2007), pp. 680–682. ISSN: 1745-2481. DOI: 10 . 1038 / nphys742.
- [3] E. I. Moses et al. "The National Ignition Facility: Transition to a User Facility". *Journal of Physics: Conference Series* 688 (1 Mar. 2016), p. 012073. ISSN: 1742-6596. DOI: 10.1088/1742-6596/688/1/012073.
- [4] A. B. Zylstra et al. "Experimental achievement and signatures of ignition at the National Ignition Facility". *Physical Review E* 106 (2 Aug. 2022), p. 025202. ISSN: 24700053. DOI: 10.1103/PHYSREVE.106.025202.
- [5] A. B. Zylstra et al. "Burning plasma achieved in inertial fusion". *Nature* 2022 601:7894 601 (7894 Jan. 2022), pp. 542–548. ISSN: 1476-4687. DOI: 10.1038/s41586-021-04281-w.
- [6] H. Abu-Shawareb et al. "Achievement of Target Gain Larger than Unity in an Inertial Fusion Experiment". *Phys. Rev. Lett.* 132 (6 2024), p. 065102. DOI: 10.1103/PhysRevLett.132.065102.
- [7] E. L. Clark et al. "Energetic Heavy-Ion and Proton Generation from Ultraintense Laser-Plasma Interactions with Solids". *Physical Review Letters* 85 (8 Aug. 2000), p. 1654. ISSN: 00319007. DOI: 10.1103/PhysRevLett.85.1654.
- [8] A. Maksimchuk et al. "Forward Ion Acceleration in Thin Films Driven by a High-Intensity Laser". *Physical Review Letters* 84 (18 May 2000), p. 4108. ISSN: 10797114. DOI: 10.1103/PhysRevLett.84.4108.
- [9] R. A. Snavely et al. "Intense High-Energy Proton Beams from Petawatt-Laser Irradiation of Solids". *Physical Review Letters* 85 (14 Oct. 2000), p. 2945. ISSN: 00319007. DOI: 10.1103/PhysRevLett.85.2945.

[10] S. C. Wilks et al. "Energetic proton generation in ultra-intense laser–solid interactions". *Physics of Plasmas* 8 (2 Feb. 2001), pp. 542–549. ISSN: 1070-664X. DOI: 10.1063/1.1333697.

- [11] F. Dollar et al. "Finite spot effects on radiation pressure acceleration from intense high-contrast laser interactions with thin targets". *Physical Review Letters* 108 (17 Apr. 2012), p. 175005. ISSN: 00319007. DOI: 10. 1103/PHYSREVLETT.108.175005.
- [12] S. Kar et al. "Ion acceleration in multispecies targets driven by intense laser radiation pressure". *Physical Review Letters* 109 (18 Nov. 2012), p. 185006. ISSN: 00319007. DOI: 10.1103/PHYSREVLETT.109.185006.
- [13] F. Fiuza et al. "Laser-driven shock acceleration of monoenergetic ion beams". *Physical Review Letters* 109 (21 Nov. 2012), p. 215001. ISSN: 00319007. DOI: 10.1103/PHYSREVLETT.109.215001.
- [14] L. Yin et al. "Three-dimensional dynamics of breakout afterburner ion acceleration using high-contrast short-pulse laser and nanoscale targets". *Physical Review Letters* 107 (4 July 2011), p. 045003. ISSN: 00319007. DOI: 10.1103/PHYSREVLETT.107.045003.
- [15] J. Park et al. "Ion acceleration in laser generated megatesla magnetic vortex". *Physics of Plasmas* 26 (10 Oct. 2019). ISSN: 10897674. DOI: 10. 1063/1.5094045/15613697/103108\_1\_ACCEPTED\_MANUSCRIPT.PDF.
- [16] H. Schwoerer et al. "Laser-plasma acceleration of quasi-monoenergetic protons from microstructured targets". *Nature* 2006 439:7075 439 (7075 Jan. 2006), pp. 445–448. ISSN: 1476-4687. DOI: 10.1038/nature04492.
- [17] J. Fuchs et al. "Comparison of laser ion acceleration from the front and rear surfaces of thin foils". *Physical Review Letters* 94 (4 Feb. 2005), p. 045004. ISSN: 00319007. DOI: 10.1103/PHYSREVLETT.94.045004.
- [18] L. Romagnani et al. "Dynamics of electric fields driving the laser acceleration of multi-MeV protons". *Physical Review Letters* 95 (19 Nov. 2005), p. 195001. ISSN: 00319007. DOI: 10.1103/PHYSREVLETT.95.195001.
- [19] A. Măgureanu et al. "Target Characteristics Used in Laser-Plasma Acceleration of Protons Based on the TNSA Mechanism". Frontiers in Physics 10 (Mar. 2022), p. 727718. ISSN: 2296424X. DOI: 10.3389/FPHY. 2022.727718/BIBTEX.

[20] A. Permogorov et al. "Effects of pulse chirp on laser-driven proton acceleration". *Scientific Reports* 2022 12:1 12 (1 Feb. 2022), pp. 1–8. ISSN: 2045-2322. DOI: 10.1038/s41598-022-07019-4.

- [21] V. Kaymak et al. "Boosted acceleration of protons by tailored ultra-thin foil targets". *Scientific Reports* 2019 9:1 9 (1 Dec. 2019), pp. 1–10. ISSN: 2045-2322. DOI: 10.1038/s41598-019-55011-2.
- [22] P. L. Poole et al. "Laser-driven ion acceleration via target normal sheath acceleration in the relativistic transparency regime". *New Journal of Physics* 20 (1 Jan. 2018), p. 013019. ISSN: 1367-2630. DOI: 10.1088/1367-2630/AA9D47.
- [23] A. Higginson et al. "Near-100 MeV protons via a laser-driven transparency-enhanced hybrid acceleration scheme". *Nature Communications* 2018 9:1 9 (1 Feb. 2018), pp. 1–9. ISSN: 2041-1723. DOI: 10.1038/s41467-018-03063-9.
- [24] M. Murakami et al. "Towards realization of hyper-velocities for impact fast ignition". *Plasma Physics and Controlled Fusion* 47 (12B Nov. 2005), B815. ISSN: 0741-3335. DOI: 10.1088/0741-3335/47/12B/S63.
- [25] S. Borodziuk et al. "Reversed scheme of thin foil acceleration". *Applied Physics Letters* 93 (10 Sept. 2008), p. 101502. ISSN: 00036951. DOI: 10. 1063/1.2979700.
- [26] S. Borodziuk and J. Kostecki. "Ablative acceleration and energy transfer in a laser-foil—foil system". *Journal of Technical Physics* 32 (1 1991), pp. 79–85. ISSN: 0324-8313.
- [27] S. Borodziuk et al. "Cavity pressure acceleration: An efficient laser-based method of production of high-velocity macroparticles". *Applied Physics Letters* 95 (23 Dec. 2009), p. 231501. ISSN: 00036951. DOI: 10. 1063/1.3271693.
- [28] S. Borodziuk et al. "Forward and backward cavity pressure acceleration of macroparticles". *Applied Physics Letters* 99 (23 Dec. 2011), p. 231501. ISSN: 00036951. DOI: 10.1063/1.3662972.
- [29] M. Karasik et al. "Acceleration to high velocities and heating by impact using Nike KrF laser". *Physics of Plasmas* 17 (5 May 2010), p. 56317. ISSN: 1070664X. DOI: 10.1063/1.3399786.
- [30] A. P. L. Robinson et al. "Radiation pressure acceleration of thin foils with circularly polarized laser pulses". *New Journal of Physics* 10.1 (2008), p. 013021. DOI: 10.1088/1367-2630/10/1/013021.

[31] S. Jabłoński, J. Badziak, and P. Rączka. "Generation of high-energy ion bunches via laser-induced cavity pressure acceleration at ultra-high laser intensities". *Laser and Particle Beams* 32.1 (2014), 129–135. DOI: 10. 1017/S0263034614000019.

- [32] J. Badziak et al. "Generation of ultra-high-pressure shocks by collision of a fast plasma projectile driven in the laser-induced cavity pressure acceleration scheme with a solid target". *Physics of Plasmas* 22.3 (Mar. 2015), p. 032709. ISSN: 1070-664X. DOI: 10 . 1063 / 1 . 4916321. eprint: https://pubs.aip.org/aip/pop/article-pdf/doi/10.1063/1. 4916321/15903862/032709\\_1\\_online.pdf.
- [33] T. Chodukowski et al. "Neutron production in cavity pressure acceleration of plasma objects". *AIP Advances* 10 (8 Aug. 2020). ISSN: 21583226. DOI: 10.1063/5.0005977.
- [34] G. Miley et al. "Panel 1: Discussion of report of the Aneutronic Fusion Committee of the National Academy of Science's Air Force Studies Board". Nuclear Instruments and Methods in Physics Research Section A: Accelerators, Spectrometers, Detectors and Associated Equipment 271 (1 Aug. 1988), pp. 217–221. ISSN: 0168-9002. DOI: 10.1016/0168-9002(88) 91152-7.
- [35] T. A. Mehlhorn et al. "Path to Increasing p-B11 Reactivity via ps and ns Lasers". Laser and Particle Beams 2022 (2022). ISSN: 1469803X. DOI: 10.1155/2022/2355629.
- [36] V. S. Belyaev et al. "Observation of neutronless fusion reactions in picosecond laser plasmas". *Physical Review E Statistical, Nonlinear, and Soft Matter Physics* 72 (2 Aug. 2005), p. 026406. ISSN: 15393755. DOI: 10.1103/PHYSREVE.72.026406.
- [37] A. Bonasera et al. "Measuring the astrophysical S-factor in plasmas". *Fission and Properties of Neutron-Rich Nuclei*. World Scientific Pub Co Pte Lt, Aug. 2008, pp. 503–507. DOI: 10.1142/9789812833433\_0061.
- [38] C. Labaune et al. "Fusion reactions initiated by laser-accelerated particle beams in a laser-produced plasma". *Nature Communications* 2013 4:1 4 (1 Oct. 2013), pp. 1–6. ISSN: 2041-1723. DOI: 10.1038/ncomms3506.
- [39] A. Picciotto et al. "Boron-proton nuclear-fusion enhancement induced in boron-doped silicon targets by low-contrast Pulsed Laser". *Physical Review X* 4 (3 Aug. 2014), p. 031030. ISSN: 21603308. DOI: 10.1103/PHYSREVX.4.031030.

[40] D. Margarone et al. "Advanced scheme for high-yield laser driven nuclear reactions". *Plasma Physics and Controlled Fusion* 57 (1 Nov. 2014), p. 014030. ISSN: 0741-3335. DOI: 10.1088/0741-3335/57/1/014030.

- [41] C. Baccou et al. "New scheme to produce aneutronic fusion reactions by laser-accelerated ions". *Laser and Particle Beams* 33 (1 Oct. 2015), pp. 117–122. ISSN: 0263-0346. DOI: 10.1017/S0263034615000178.
- [42] L. Giuffrida et al. "High-current stream of energetic alpha particles from laser-driven proton-boron fusion". *Physical Review E* 101 (1 Jan. 2020), p. 013204. ISSN: 24700053. DOI: 10.1103/PHYSREVE.101.013204.
- [43] J. Bonvalet et al. "Energetic alpha -particle sources produced through proton-boron reactions by high-energy high-intensity laser beams". *Physical Review E* 103 (5 May 2021), p. 053202. ISSN: 24700053. DOI: 10.1103/PHYSREVE.103.053202.
- [44] D. Margarone et al. "In-Target Proton–Boron Nuclear Fusion Using a PW-Class Laser". *Applied Sciences (Switzerland)* 12 (3 Feb. 2022). ISSN: 20763417. DOI: 10.3390/APP12031444.
- [45] T. T. Böhlen et al. "The FLUKA Code: Developments and Challenges for High Energy and Medical Applications". *Nuclear Data Sheets* 120 (June 2014), pp. 211–214. ISSN: 0090-3752. DOI: 10.1016/J.NDS.2014. 07.049.
- [46] B. Fryxell et al. "FLASH: An Adaptive Mesh Hydrodynamics Code for Modeling Astrophysical Thermonuclear Flashes". *The Astrophysical Journal Supplement Series* 131.1 (2000), p. 273. DOI: 10.1086/317361.
- [47] P. Raczka et al. "Target Charging, Strong Electromagnetic Pulse Emission and Proton Acceleration from Thin Foils at 10 TW IPPLM Femtosecond Laser Facility". *Acta Physica Polonica A* 138 (4 Oct. 2020), pp. 593–600. ISSN: 1898794X. DOI: 10.12693/APHYSPOLA.138.593.
- [48] P. Rączka et al. "Measurement of the electric field strength generated in the experimental chamber by 10 TW femtosecond laser pulse interaction with a solid target". *Journal of Instrumentation* 14 (04 Apr. 2019). ISSN: 1748-0221. DOI: 10.1088/1748-0221/14/04/P04008.
- [49] L. Torrisi et al. "Target normal sheath acceleration by fs laser and advanced carbon foils with gold films and nanoparticles". *Physics of Plasmas* 27 (4 Apr. 2020), p. 43107. ISSN: 10897674. DOI: 10.1063/5.0004834/318842.

[50] L. Torrisi et al. "Ion acceleration from aluminium plasma generated by a femtosecond laser in different conditions". *Contributions to Plasma Physics* 60 (4 May 2020), e201900187. ISSN: 1521-3986. DOI: 10.1002/CTPP.201900187.

- [51] F. Wagner et al. "Maximum Proton Energy above 85 MeV from the Relativistic Interaction of Laser Pulses with Micrometer Thick CH<sub>2</sub> Targets". *Phys. Rev. Lett.* 116 (20 2016), p. 205002. DOI: 10 . 1103 / PhysRevLett.116.205002.
- [52] D. C. Carroll et al. "A modified Thomson parabola spectrometer for high resolution multi-MeV ion measurements-Application to laser-driven ion acceleration". Nuclear Instruments and Methods in Physics Research, Section A: Accelerators, Spectrometers, Detectors and Associated Equipment 620 (1 Aug. 2010), pp. 23–27. ISSN: 01689002. DOI: 10.1016/J.NIMA.2010.01.054.
- [53] P. Tchórz et al. "Capabilities of Thomson parabola spectrometer in various laser-plasma- and laser-fusion-related experiments". *Nukleonika* 68.1 (2023), pp. 29–36. DOI: 10.2478/nuka-2023-0005.
- [54] R. Brun et al. "root-project/root: v6.18/02" (Aug. 2019). DOI: 10.5281/ZENODO.3895860.
- [55] V. Kantarelou et al. "A Methodology for the Discrimination of Alpha Particles from Other Ions in Laser-Driven Proton-Boron Reactions Using CR-39 Detectors Coupled in a Thomson Parabola Spectrometer". *Laser and Particle Beams* 2023 (2023). ISSN: 1469803X. DOI: 10.1155/2023/3125787.
- [56] G. Milluzzo et al. "Extended characterization of alpha particles via laser-induced p-11B fusion reaction in silicon hydrogenated boron-doped thin targets". *Journal of Instrumentation* 18 (07 July 2023), p. C07022. ISSN: 1748-0221. DOI: 10.1088/1748-0221/18/07/C07022.
- [57] A. Ferrari et al. "Work supported by Department of Energy contract DE-AC02-76SF00515. FLUKA: A Multi-Particle Transport Code" (2005).
- [58] American Nuclear Society. Mathematics et al. "Flair: A powerful but user friendly graphical interface for FLUKA" (2009).
- [59] K. L. Laursen et al. "Complete kinematical study of the 3 alpha breakup of the 16.11 MeV state in 12 C". *The European Physical Journal A* 52 (2016). DOI: 10.1140/epja/i2016-16271-2.

[60] V. Istokskaia et al. "A multi-MeV alpha particle source via proton-boron fusion driven by a 10-GW tabletop laser". *Communications Physics* 2023 6:1 6 (1 Feb. 2023), pp. 1–8. ISSN: 2399-3650. DOI: 10.1038/s42005-023-01135-x.

- [61] B. M. Hegelich et al. "Photon and Neutron Production as in Situ Diagnostics of Proton-Boron Fusion". Laser and Particle Beams 2023 (2023). ISSN: 1469803X. DOI: 10.1155/2023/6924841.
- [62] M. Tosca et al. "Plasma polymers as targets for laser-driven proton-boron fusion". Frontiers in Physics 11 (July 2023), p. 1227140. ISSN: 2296424X. DOI: 10.3389/FPHY.2023.1227140.
- [63] D. Kong et al. "Alpha-Particle Generation from H-11B Fusion Initiated by Laser-Accelerated Boron Ions". Laser and Particle Beams 2022 (2022). ISSN: 1469803X. DOI: 10.1155/2022/5733475.
- [64] K. Jungwirth et al. "The Prague Asterix Laser System". *Physics of Plasmas* 8 (2001), p. 2495. DOI: 10.1063/1.1350569.
- [65] H. Daido et al. "Neutron production from a shell-confined carbon-deuterium plasma by 1.06 um laser irradiation". Applied Physics Letters 51 (26 Dec. 1987), pp. 2195–2196. ISSN: 0003-6951. DOI: 10.1063/1.98937.
- [66] J. Krása et al. "Observation of repetitive bursts in emission of fast ions and neutrons in sub-nanosecond laser-solid experiments". *Laser and Particle Beams* 31 (3 Sept. 2013), pp. 395–401. ISSN: 0263-0346. DOI: 10. 1017/S0263034613000360.
- [67] J. F. Ziegler, M. D. Ziegler, and J. P. Biersack. "SRIM The stopping and range of ions in matter (2010)". *Nuclear Instruments and Methods in Physics Research Section B: Beam Interactions with Materials and Atoms* 268 (11-12 June 2010), pp. 1818–1823. ISSN: 0168-583X. DOI: 10.1016/J. NIMB. 2010.02.091.
- [68] O. B. Tarasov and D. Bazin. "LISE++: design your own spectrometer". Nuclear Physics A 746 (1-4 SPEC.ISS. Dec. 2004), pp. 411–414. ISSN: 0375-9474. DOI: 10.1016/J.NUCLPHYSA.2004.09.063.
- [69] C. Baccou et al. "CR-39 track detector calibration for H, He, and C ions from 0.1-0.5 MeV up to 5 MeV for laser-induced nuclear fusion product identification". 86.8 (Aug. 2015), p. 083307. ISSN: 0034-6748. DOI: 10.1063/1.4927684.

[70] C. A. Schneider, W. S. Rasband, and K. W. Eliceiri. "NIH Image to ImageJ: 25 years of image analysis". *Nature Methods* 2012 9:7 9 (7 June 2012), pp. 671–675. ISSN: 1548-7105. DOI: 10.1038/nmeth.2089.

- [71] K. Nedunchezhian et al. "Boron Neutron Capture Therapy A Literature Review". *Journal of Clinical and Diagnostic Research : JCDR* 10 (12 Dec. 2016), ZE01. ISSN: 0973709X. DOI: 10.7860/JCDR/2016/19890. 9024.
- [72] P. Martin et al. "Absolute calibration of Fujifilm BAS-TR image plate response to laser driven protons up to 40 MeV" (2022). DOI: 10.1063/5.0089402.
- [73] H. Ruhl and G. Korn. "A laser-driven mixed fuel nuclear fusion microreactor concept" (2022). arXiv: 2202.03170 [physics.plasm-ph].
- [74] P. Tchórz et al. "Proton beams generated via thermonuclear deuterium–deuterium fusion by means of modified cavity pressure acceleration-type targets as a candidate for proton–boron fusion driver". *Physics of Plasmas* 31.8 (Sept. 2024), p. 084503. ISSN: 1070-664X. DOI: 10.1063/5.0207108.